Plasmonic Nano-Photocatalysts for Light-Induced Alcohol Oxidation

Meltiani Belekoukia

Submitted for the degree of Doctor of Philosophy

Heriot-Watt University

School of Engineering and Physical Sciences

September 2020

ABSTRACT

Photocatalytic oxidation of alcohols in the presence of plasmonic metals using oxygen as oxidizing agent is considered as a promising approach for efficient and green chemical transformations under mild conditions. In this direction, this Thesis demonstrates the synthesis of commercially valuable products such as benzaldehyde *via* the development of plasmonic-based nanomaterials as photocatalysts, along with design of continuous flow reactor, enabling high reaction rate and high selectivity of formed carbonyl compounds.

Initially, the current state of photocatalytic oxidation of alcohols is summarized, the importance and fundamentals of plasmonic metal nanoparticles is presented while challenges and research gaps of the field are highlighted. Three experimental strategies were adopted in the Thesis. The first experimental part of the thesis focused on understanding the plasmonic heating effect generated by Au nanoparticles and particularly the surface plasmon resonance of Au nanoparticles by performing a well-controlled experiment using a continuous flow system. The results revealed a significant temperature rise of Au-based nanofluids, with different Au loadings, compared to bare TiO_2 nanofluid or pure water, which arise from the localized surface plasmon resonance effect of Au nanoparticles.

The second experimental part of the thesis aimed to investigate the performance of plasmonic Au nanoparticles decorated on Cr_2O_3 microspheres towards the photocatalytic oxidation of benzyl alcohol. It has been shown that the amount of Au loading affected significantly the reaction efficiency, with 1.18 wt.% of Au loaded photocatalyst converting 81.4% of benzyl alcohol to benzaldehyde with a selectivity of 98.3% after 3 hours of laser irradiation. Additionally the plasmonic heating effect of Au nanoparticles contributed to a 26% oxidation rate enhancement using 1.18 wt.% Au.

In the third experimental part, the effect of incorporating a second noble metal like Ag as well as the fabrication of a continuous flow reactor for comparison with a typical batch reactor were demonstrated. Bimetallic $0.34Ag-1.21Au/Cr_2O_3$ photocatalyst converted 92.4% of benzyl alcohol to benzaldehyde with 98.8 % selectivity, which is 4.5 times that of pure Cr_2O_3 and 1.3 times of monometallic $1.18Au/Cr_2O_3$. The results showed that the reaction rate under continuous flow conditions was almost an order of magnitude superior to the values achieved using batch reactor. Therefore, the findings of this Thesis highlight the need for development and optimization of continuous flow synthesis of carbonyl compounds in the presence of plasmonic metals, which can favour the conversion of alcohols in terms of reaction rate and selectivity.

DEDICATION

To my parents

Eleni and Andreas

ACKNOWLEDGEMENTS

Research Thesis Submission

Name*:*	Meltiani Belekoukia		
School:	EPS		
Version: *(i.e. First, Resubmission, Final)*	Final	Degree Sought:	PhD

Declaration

In accordance with the appropriate regulations I hereby submit my thesis and I declare that:

1. The thesis embodies the results of my own work and has been composed by myself
2. Where appropriate, I have made acknowledgement of the work of others
3. The thesis is the correct version for submission and is the same version as any electronic versions submitted*.
4. My thesis for the award referred to, deposited in the Heriot-Watt University Library, should be made available for loan or photocopying and be available via the Institutional Repository, subject to such conditions as the Librarian may require
5. I understand that as a student of the University I am required to abide by the Regulations of the University and to conform to its discipline.
6. I confirm that the thesis has been verified against plagiarism via an approved plagiarism detection application e.g. Turnitin.
7. Where the thesis contains published outputs under Regulation 6 (9.1.2) or Regulation 43 (9) these are accompanied by a critical review which accurately describes my contribution to the research and, for multi-author outputs, a signed declaration indicating the contribution of each author (complete)
8. Inclusion of published outputs under Regulation 6 (9.1.2) or Regulation 43 (9) shall not constitute plagiarism.

* *Please note that it is the responsibility of the candidate to ensure that the correct version of the thesis is submitted.*

Signature of Candidate*:*	*Meltiani*	Date:	14/09/2020

Submission

Submitted By *(name in capitals):*	MELTIANI BELEKOUKIA
Signature of Individual Submitting:	*Meltiani*
Date Submitted:	14/09/2020

For Completion in the Student Service Centre (SSC)

Limited Access	Requested	Yes		No		Approved	Yes		No	
*E-thesis Submitted (**mandatory for final theses**)*										
Received in the SSC by *(name in capitals):*						Date:				

Inclusion of Published Works

Declaration

This thesis contains one or more multi-author published works. In accordance with Regulation 6 (9.1.2) I hereby declare that the contributions of each author to these publications is as follows:

Citation details	**M. Belekoukia**, E. Kalamaras, J. Z. Y. Tan, F. Vilela, S. Garcia, M. M. Maroto-Valer, J. Xuan. "Continuous flow-based laser-assisted plasmonic heating: A new approach for photothermal energy conversion and utilization", Applied Energy 247, 517-524, (2019).
Meltiani Belekoukia	Review of relevant research, Material synthesis, Design and fabrication of continuous flow container, design of experiments, perform the experiments, analysis of results, writing up of publication,
All other authors	Supervision on work, Feedback/comments on publication, Proofreading, paper submission
Signature:	
Date:	14/09/2020

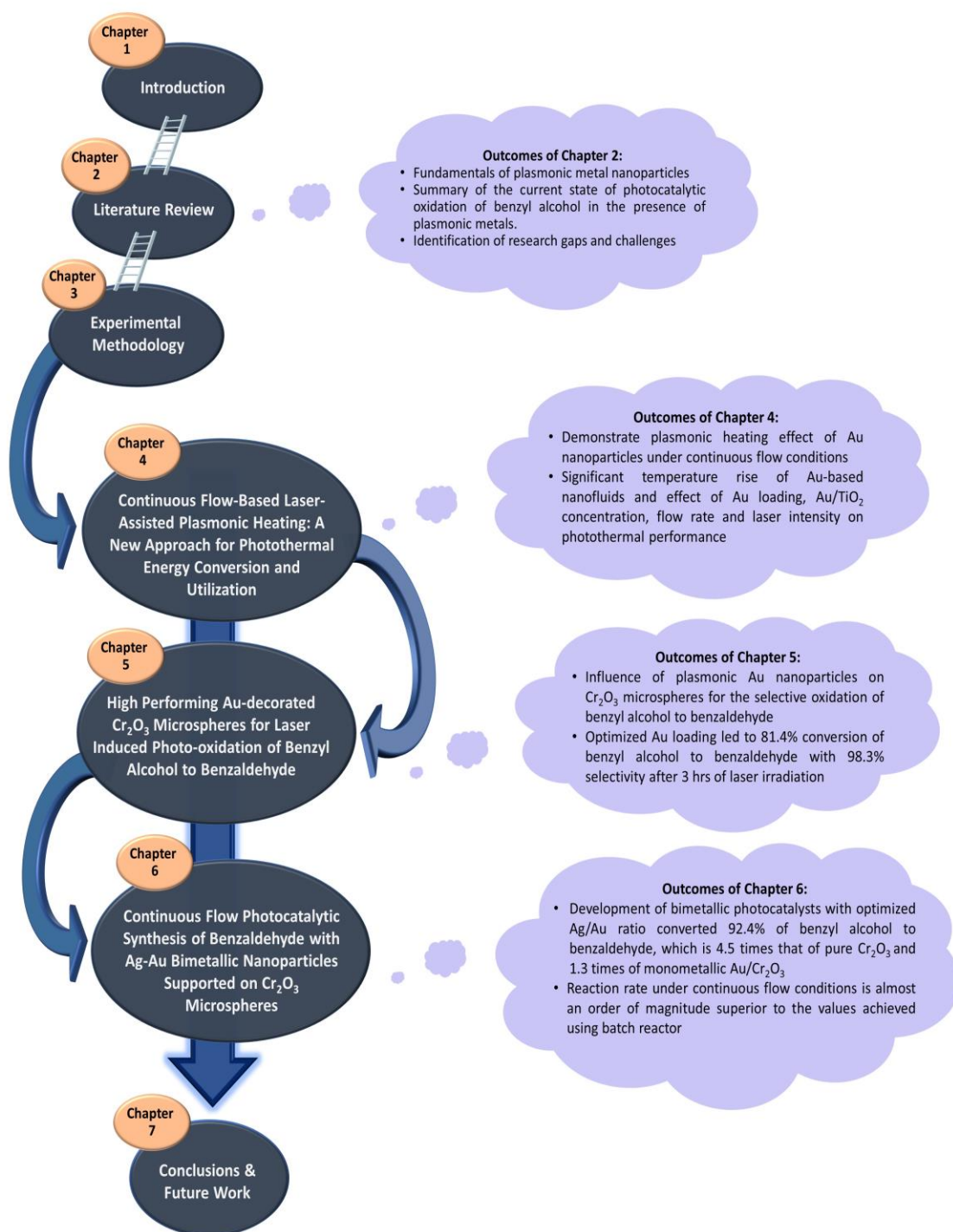| Citation details	**M. Belekoukia**, J. Z. Y. Tan, J.M. Andresen, H. Wang, M. Mercedes Maroto-Valer, J. Xuan. "Laser Induced Plasmonic Heating with Au Decorated TiO_2 Nanoparticles", Energy Procedia, 2019, 158, 5647-5652.
Author 1	Review of relevant research, material synthesis, Design and fabrication of batch container, design of experiments, perform the experiments, analysis of results, writing up of publication, paper submission
Author 2	Supervision on work, Feedback/comments on publication, Proofreading
Signature:	
Date:	14/09/2020

Overview of PhD Thesis

Chapter 1

Introduction

Chapter 2

Literature Review

Chapter 3

Experimental Methodology

Outcomes of Chapter 2:
- Fundamentals of plasmonic metal nanoparticles
- Summary of the current state of photocatalytic oxidation of benzyl alcohol in the presence of plasmonic metals.
- Identification of research gaps and challenges

Chapter 4

Continuous Flow-Based Laser-Assisted Plasmonic Heating: A New Approach for Photothermal Energy Conversion and Utilization

Outcomes of Chapter 4:
- Demonstrate plasmonic heating effect of Au nanoparticles under continuous flow conditions
- Significant temperature rise of Au-based nanofluids and effect of Au loading, Au/TiO_2 concentration, flow rate and laser intensity on photothermal performance

Chapter 5

High Performing Au-decorated Cr_2O_3 Microspheres for Laser Induced Photo-oxidation of Benzyl Alcohol to Benzaldehyde

Outcomes of Chapter 5:
- Influence of plasmonic Au nanoparticles on Cr_2O_3 microspheres for the selective oxidation of benzyl alcohol to benzaldehyde
- Optimized Au loading led to 81.4% conversion of benzyl alcohol to benzaldehyde with 98.3% selectivity after 3 hrs of laser irradiation

Chapter 6

Continuous Flow Photocatalytic Synthesis of Benzaldehyde with Ag-Au Bimetallic Nanoparticles Supported on Cr_2O_3 Microspheres

Outcomes of Chapter 6:
- Development of bimetallic photocatalysts with optimized Ag/Au ratio converted 92.4% of benzyl alcohol to benzaldehyde, which is 4.5 times that of pure Cr_2O_3 and 1.3 times of monometallic Au/Cr_2O_3
- Reaction rate under continuous flow conditions is almost an order of magnitude superior to the values achieved using batch reactor

Chapter 7

Conclusions & Future Work

TABLE OF CONTENTS

ACRONYMS

AO   Ammonium oxalate

C_6H_5CHO Benzaldehyde

BQ   1,4-benzoquinone

CO_2 Carbon dioxide

Cr_2O_3 Chromium oxide

CB   Conduction band

CW   Continuous wave

DP   Deposition-precipitation

DRS   Diffuse reflectance spectra

DMC   Dimethylcarbonate

e^- Electron

EDX   Energy-dispersive X-Ray spectroscopy

fs   femtosecond (10^{-12} s)

FDTD   Fine Difference Time Domain

FID   Flame ionization detector

FTO   Fluorine-doped tin oxide

GC   Gas Chromatography

Au   Gold

$AuCl_4 \cdot 3H_2O$ Gold(III) chloride trihydrate

HR-TEM   High resolution Transmission electron microscopy

h^+ Hole

$^{\cdot}OH$ Hydroxyl radicals

IR   Infrared

JCPDS   Joint Committee on Powder Diffraction Standards

Laser   Light amplification by stimulated emission of radiation

LEDs   Light-emitting diodes

LSPR   Localized Surface Plasmon Resonance

μmol   micromole

$mg\ mL^{-1}$ milligram per millilitre

$mL\ min^{-1}$ millilitre per minute

mM   millimolar

mW/cm^2 milliwatt per square centimeter

M   Molar, concentration mol/L

mol   moles

nm   nanometer (10^{-9} m)

NPs   Nanoparticles

PEC   Photoelectrochemical

ps   picosecond (10^{-12} s)

PRET   Plasmon Resonance Energy Transfer

Pt   Platinum

PMMA   Polymethyl methacrylate

pH   Potential of hydrogen

Redox   Reduction-oxidation

rpm   Revolution per minute

SEM   Scanning electron microscopy

Ag   Silver

$AgNO_3$ Silver nitrate

O_2^- Superoxide radicals

SPR   Surface Plasmon Resonance

TBA   Tert-butyl alcohol

TiO_2 Titania

TEM   Transmission electron microscopy

TOF   Turnover frequency

UV   Ultraviolet

VB   Valence band

Vis   Visible

cm^{-1} Wavenumber

wt.%   Weight percentage

XeHg   Xenon mercury

XRD   X-Ray diffraction

SYMBOLS

A   Absorbance

θ Angle between incident and normal to lattice plane

°C   Celcius

$C_{alcohol}$ Concentration of alcohol after reaction

$C_{aldehyde}$ Concentration of formed aldehyde

x   Concentration of formed product

R^2 Correlation coefficients

L   Crystallite size

k   Dimensionless shape factor

B   Full width of half maximum of the peak

C_0 Initial concentration of alcohol

Io   Intensity of incident light

I   Intensity of transmitted light

ε Molar absorptivity

n   Order of reflection

l   Path length

d   Planar spacing

k	Rate constant
t	Reaction time
R	Reflectance
T	Transmittance
λ	X-Ray wavelength

LIST OF PUBLICATIONS BY THE CANDIDATE

Published

- "Continuous flow-based laser-assisted plasmonic heating: A new approach for photothermal energy conversion and utilization", **M. Belekoukia**, E. Kalamaras, J. Z. Y. Tan, F. Vilela, S. Garcia, M. M. Maroto-Valer, J. Xuan. Applied Energy 247, 517-524, (2019).

- "A microfluidic photoelectrochemical cell for solar-driven CO_2 conversion into liquid fuels with CuO-based photocathodes", E. Kalamaras, **M. Belekoukia**, J. Z. Y. Tan, J. Xuan, M. Maroto-Valer, H. J. Andersen. Faraday Discussions, 215, 329-344 (2019).

- "Laser Induced Plasmonic Heating with Au Decorated TiO_2 Nanoparticles", **M. Belekoukia**, J. Z. Y. Tan, J.M. Andresen, H. Wang, M. Mercedes Maroto-Valer, J. Xuan, Energy Procedia, 2019, 158, 5647-5652.

- "Techno-economic assessment of a hybrid off-grid DC system for combined heat and power generation in remote islands" E. Kalamaras, **M. Belekoukia,** Z. Lin, B. Xu, H. Wang, J. Xuan. Energy Procedia, 142, 501-506 (2019).

Submitted or under preparation manuscripts

- "High Performing Au-decorated Cr_2O_3 Microspheres for Laser Induced Photo-oxidation of Benzyl Alcohol to Benzaldehyde" **M. Belekoukia,** J. Tan, E. Kalamaras, F. Vilela, S. Garcia, M. Mercedes Maroto-Valer, J. Xuan, Ready for submission.

- "A continuous flow cell for light-induced benzyl alcohol oxidation in the presence of bimetallic nanoparticles supported on Cr_2O_3 microspheres as heterogeneous photocatalysts " **M. Belekoukia**, J. Tan, E. Kalamaras, F. Vilela, S. Garcia, M. Mercedes Maroto-Valer, J. Xuan, Ready for submission.

Research work presented in Conferences/Workshops

- Annual poster event of School of Engineering and Physical Sciences (EPS), 12 October 2016, Heriot-Watt University. "Laser Induced and Enhanced Chemical Processes for Energy and Environmental Applications. **(Chapter 2)**

- 10th International Conference on Applied Energy (ICAE), 22-25 August 2018, Hong Kong. "Laser Induced Plasmonic Heating with Au Decorated TiO_2 Nanoparticles". **(Chapter 4)**

- Poster event organized by Research Centre for Carbon Solutions, 28 May 2018, Heriot-Watt University. "Laser induced photosynthesis of C_6H_5COH using Au-decorated Cr_2O_3 microspheres". **(Chapter 5)**

- 235th ECS Meeting, 26-30 May 2019, Dallas, US. "Bimetallic Nanoparticles Supported on Cr_2O_3 Microspheres as Heterogeneous Photocatalysts for Light-Induced Alcohol Oxidation". **(Chapters 5 & 6)**

Chapter 1 – Introduction

1.1   Photocatalysis in chemical industry

In the chemical industry, transformation of organic compounds is of great importance, as high-value pharmaceuticals, cosmetics, food and fragrance products can be formed. However, the chemical industry tends to rely on increasing temperature, pressure, concentration of reactants and residence time to improve the production [1, 2]. While these industrial processes increase reaction rate, they are unsustainable, energy inefficient and involve use and formation of unwanted toxic and hazardous compounds. Therefore, an increasing research interest has been devoted in the development of low-cost and environmentally friendly approaches using light harvesting energy technologies for a large variety of chemical transformations. Photocatalysis is considered an attractive process to drive effectively chemical transformations under mild conditions, free of hazardous compounds as well as improve their spatial and temporal control [3, 4]. Light harvesting energy conversion by means of photocatalytic processes has attracted significant interest since Fujishima and Honda reported for the first-time hydrogen production *via* photoelectrochemical water-splitting using TiO_2 as photoanode [5]. TiO_2 is a benchmark photocatalyst with a wide band gap semiconductor, which benefits from its low-cost, lack of toxicity, chemical resistance and excellent stability [6]. Subsequently, a large variety of semiconductor photocatalysts (ZnO, SiO_2, CeO_2, Cu_2O, WO_3, Fe_2O_3, etc.) have been used in several photocatalytic applications such as water splitting, CO_2 reduction, environmental pollution and formation of valuable chemicals in the pharmaceutical industry [7-10].

1.2   Green chemistry and alcohol oxidation

The development of high-value carbonyl compounds such as aldehydes and ketones, through selective oxidation of alcohols, holds great importance in the pharmaceutical industries [11, 12]. Among various carbonyl compounds, benzaldehyde (C_6H_5CHO) is one of the most important aromatic molecules used as valuable intermediate in pharmaceuticals, fragrances and food industry [2, 13, 14]. Particularly, benzaldehyde is an important fine chemical to produce antibiotics to treat bacterial infections (chloramphenicol, ampicillin), pharmaceuticals guarding against high blood pressure (ephedrine), anti-seizure medication (diphenylhydantoin), and amino acids (*e.g.*, phenylglycine used in antibiotics and pseudoephedrine, which is the active ingredient in most cough syrups). Industrially, benzaldehyde is synthesized by hydrolysis of benzyl

chloride derived from toluene chlorination, producing a large amount of toxic waste (Reaction 1.1) [15]. Particularly, this process is carried out at high temperatures (110-180 ℃), and involves the production of hazardous intermediates, while the formation of by-products reveals poor selectivity decreasing the profits [16].

$$C_6H_5CHCl_2 + H_2O \rightarrow C_6H_5CHO + 2HCl \tag{1.1}$$
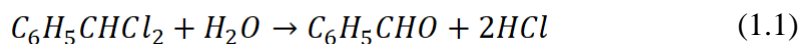
Therefore, it is of great interest to develop environmentally benign processes to produce the corresponding aldehydes with high selectivity. Heterogeneous photocatalytic oxidation of alcohols using semiconducting photocatalysts and oxygen as oxidant has been proposed as a more sustainable process under mild conditions for organic synthesis of carbonyl compounds in which the benzaldehyde is the desired product and the benzoic acid is the by-product (Reaction 1.2) [17-19]. Benzyl alcohol is a natural component of many fruits and teas and can be found in the essential oils of plants such as jasmine and hyacinth. Benzyl alcohol is manufactured industrially via the hydrolysis of benzyl chloride and sodium hydroxide and through toluene oxidation process, releasing chlorine and consuming solvents with the inclusion of toxic substances [20]. It can also be produced from benzyl acetate by hydrolysis or by transesterification with methanol, where useful acetic acid can be formed as the by-product without discharging waste water, thus being economical and of low environmental load. It should be noted here that there is an urgent need to develop a sustainable path of energy for industrial production of benzyl alcohol, which is the proposed source of benzaldehyde formation, and research efforts should be devoted towards this direction. In this work, we focus on the oxidation of benzyl alcohol to benzaldehyde via photocatalysis, which is an environmentally friendly route.
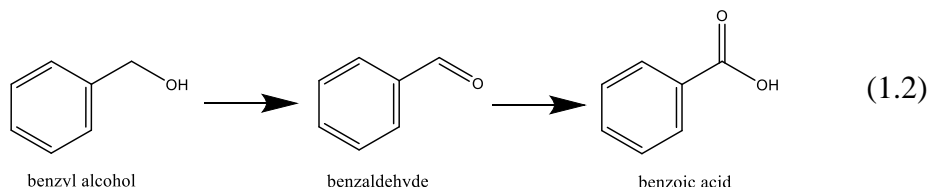
Photocatalytic oxidation of alcohols to the corresponding aldehydes has been extensively investigated using several photocatalysts over a decade with significant improvements. However, it is crucial to further investigate and optimize the photocatalytic oxidation of alcohols in terms of reaction rate and selectivity, before industry can proceed to large-scale production of carbonyl compounds. A deep

understanding of the parameters that affect the photocatalytic oxidation of alcohols including efficient photocatalysts, reactor configuration and light source is needed to further optimize yields. A review on the parameters affecting the photocatalytic performance and the current challenges in photocatalysis field is presented in Chapter 2.

1.3 Aims and objectives of the Thesis

While many studies have explored the photocatalytic oxidation of benzyl alcohol, the development of efficient photocatalytic processes under mild conditions in terms of reaction rate and selectivity remains a significant challenge. The aim of this Thesis is to investigate batch and continuous flow synthesis of commercially valuable products such as benzaldehyde using plasmonic nano-photocatalysts. Different approaches were adopted to increase the sustainability of the process by enhancing the photocatalytic performance with respect to reaction rate and selectivity.

To achieve this the following objectives will be accomplished:

1. Investigate the surface plasmon resonance and particularly the plasmonic heating effect of Au nanoparticles using visible laser light under continuous flow conditions. Chapter 4 explores thoroughly the influence of Au loading, Au/TiO_2 NPs concentration and laser intensity versus flow rate on the optical and photothermal properties of Au/TiO_2 nanofluids.

2. Explore the performance of plasmonic Au nanoparticles (NPs) decorated on Cr_2O_3 microspheres as efficient photocatalysts for the photocatalytic oxidation of benzyl alcohol under visible laser irradiation. Having confirmed the surface plasmon resonance effect of Au NPs decorated on metal oxides through the concept of continuous flow based plasmonic heating, Chapter 5 evaluates the production of benzaldehyde by investigating the effect of Au loading on Cr_2O_3 with respect to the amount of Au, highlighting the importance of optimised metal loading. A series of scavenging experiments were performed to explore the photocatalytic mechanism of Au/Cr_2O_3 microspheres.

3. Study the activity of bimetallic Au and Ag nanoparticles decorated on hydrothermally synthesized Cr_2O_3 microspheres over their monometallic counterparts for batch and continuous flow synthesis of benzaldehyde. Based on

the successful application of monometallic Au nanoparticles decorated on Cr_2O_3 microspheres for the photo-oxidation of benzyl alcohol to benzaldehyde, Chapter 6 presents the effect of incorporating a second metal like Ag and the significance of Ag/Au ratio in the photocatalytic oxidation of benzyl alcohol. Further to the batch testing in the presence of bimetallic NPs, Chapter 6 investigates the continuous flow synthesis of benzaldehyde in the presence of bimetallic nanoparticles. A continuous flow reactor with the merits of high heat and mass transfer and good control of residence time was developed to better evaluate the effect of substrate residence time with the catalyst. Using pure Cr_2O_3 and optimized mono- and bi- metallic photocatalysts obtained from batch type reactions, different parameters such as concentration of metal nanoparticles, flow rate and laser intensity that affected significantly the photocatalytic performance were studied.

The main metrics used to evaluate the photocatalytic activity in both batch and continuous flow cells were conversion of benzyl alcohol, selectivity of benzaldehyde and reaction rate. In addition, physicochemical characterizations such as Scanning electron microscopy (SEM), Transmission electron microscopy (TEM), Energy-dispersive X-Ray spectroscopy (EDX), X-Ray diffraction (XRD), Raman spectroscopy, UV-Vis spectroscopy and electrochemical characterization such as chronoamperometry of the photocatalysts were performed.

The ground-breaking aspects of this study lie in:

- Use of novel mono- and bi- metallic Ag/Au NPs supported on Cr_2O_3 microspheres as efficient plasmonic nano-photocatalysts for the selective oxidation of benzyl alcohol to benzaldehyde and evaluation of the photothermal effect on the photocatalytic activity.

- Optimization of photocatalytic oxidation of benzyl alcohol in terms of reaction rate *via* the development of a continuous flow reactor. The continuous flow system benefits from improved heat and mass transfer and allows control of operating conditions over fluids.

1.4 References

[1] L. Kesavan, R. Tiruvalam, M.H.A. Rahim, M.I. bin Saiman, D.I. Enache, R.L. Jenkins, N. Dimitratos, J.A. Lopez-Sanchez, S.H. Taylor, D.W. Knight, C.J. Kiely, G.J. Hutchings, Solvent-Free Oxidation of Primary Carbon-Hydrogen Bonds in Toluene Using Au-Pd Alloy Nanoparticles, Science, 331 (2011) 195-199.

[2] G.-J.t. Brink, I.W.C.E. Arends, R.A. Sheldon, Green, Catalytic Oxidation of Alcohols in Water, Science, 287 (2000) 1636-1639.

[3] X. Lang, X. Chen, J. Zhao, Heterogeneous visible light photocatalysis for selective organic transformations, Chemical Society Reviews, 43 (2014) 473-486.

[4] D. Friedmann, A. Hakki, H. Kim, W. Choi, D. Bahnemann, Heterogeneous photocatalytic organic synthesis: state-of-the-art and future perspectives, Green Chemistry, 18 (2016) 5391-5411.

[5] A. Fujishima, K. Honda, Electrochemical Photolysis of Water at a Semiconductor Electrode, Nature, 238 (1972) 37-38.

[6] Y. Lan, Y. Lu, Z. Ren, Mini review on photocatalysis of titanium dioxide nanoparticles and their solar applications, Nano Energy, 2 (2013) 1031-1045.

[7] H.-E. Cheng, C.-Y. Lin, C.-M. Hsu, Fabrication of SnO_2-TiO_2 core-shell nanopillar-array films for enhanced photocatalytic activity, Applied Surface Science, 396 (2017) 393-399.

[8] M. Qamar, Z.H. Yamani, M.A. Gondal, K. Alhooshani, Synthesis and comparative photocatalytic activity of Pt/WO_3 and Au/WO_3 nanocomposites under sunlight-type excitation, Solid State Sciences, 13 (2011) 1748-1754.

[9] Y. Pan, S. Deng, L. Polavarapu, N. Gao, P. Yuan, C.H. Sow, Q.-H. Xu, Plasmon-Enhanced Photocatalytic Properties of Cu_2O Nanowire–Au Nanoparticle Assemblies, Langmuir, 28 (2012) 12304-12310.

[10] X. Chen, Z. Zheng, X. Ke, E. Jaatinen, T. Xie, D. Wang, C. Guo, J. Zhao, H. Zhu, Supported silver nanoparticles as photocatalysts under ultraviolet and visible light irradiation, Green Chemistry, 12 (2010) 414-419.

[11] C. Bai, A. Li, X. Yao, H. Liu, Y. Li, Efficient and selective aerobic oxidation of alcohols catalysed by MOF-derived Co catalysts, Green Chemistry, 18 (2016) 1061-1069.

[12] A. Tanaka, K. Hashimoto, H. Kominami, Preparation of Au/CeO_2 Exhibiting Strong Surface Plasmon Resonance Effective for Selective or Chemoselective Oxidation of Alcohols to Aldehydes or Ketones in Aqueous Suspensions under Irradiation by Green Light, Journal of the American Chemical Society, 134 (2012) 14526-14533.

[13] A. Abad, P. Concepción, A. Corma, H. García, A Collaborative Effect between Gold and a Support Induces the Selective Oxidation of Alcohols, Angewandte Chemie International Edition, 44 (2005) 4066-4069.

[14] C.Y. Ma, B.J. Dou, J.J. Li, J. Cheng, Q. Hu, Z.P. Hao, S.Z. Qiao, Catalytic oxidation of benzyl alcohol on Au or Au–Pd nanoparticles confined in mesoporous silica, Applied Catalysis B: Environmental, 92 (2009) 202-208.

[15] Lipper K.-A., Löser E., Brücher O., (2017), Benzyl Chloride and Other Side-Chain-Chlorinated Aromatic Hydrocarbons in Ullmann's Encyclopedia of Industrial Chemistry, Wiley-VCH, Weinheim pp. 1-22.

[16] F.M. Menger, C. Lee, Synthetically useful oxidations at solid sodium permanganate surfaces, Tetrahedron Letters, 22 (1981) 1655-1656.

[17] S. Yurdakal, G. Palmisano, V. Loddo, V. Augugliaro, L. Palmisano, Nanostructured Rutile TiO_2 for Selective Photocatalytic Oxidation of Aromatic Alcohols to Aldehydes in Water, Journal of the American Chemical Society, 130 (2008) 1568-1569.

[18] S. Sarina, H. Zhu, E. Jaatinen, Q. Xiao, H. Liu, J. Jia, C. Chen, J. Zhao, Enhancing Catalytic Performance of Palladium in Gold and Palladium Alloy Nanoparticles for Organic Synthesis Reactions through Visible Light Irradiation at Ambient Temperatures, Journal of the American Chemical Society, 135 (2013) 5793-5801.

[19] Y. Liu, P. Zhang, B. Tian, J. Zhang, Core–Shell Structural $CdS@SnO_2$ Nanorods with Excellent Visible-Light Photocatalytic Activity for the Selective Oxidation of Benzyl Alcohol to Benzaldehyde, ACS Applied Materials & Interfaces, 7 (2015) 13849-13858.

[20] Brühne F., Wright E., (2000) Ullmann's Encyclopedia of Industrial Chemistry, Wiley-VCH, Weinheim, pp. 357-365.

Chapter 2 - Literature Review

The aim of this Chapter is to provide the necessary background for understanding the research work presented in this Thesis. Initially, principles of photocatalysis and current challenges are summarized. The fundamentals of plasmonic metal nanoparticles and the possible mechanisms of plasmonic photocatalysis are discussed. Then, the influence of reactor configuration in the photocatalytic performance and the importance of light irradiation and particularly the benefits of using laser as source of photons are identified. Finally, the progress that has been made so far in photocatalytic oxidation of benzyl alcohol in the presence of plasmonic metal nanoparticles is reviewed while the effect of metal particle size, preparation method and catalyst support is evaluated.

2.1 Semiconductor Photocatalysis: principles and challenges

Photocatalysis is known as the process where light is utilized to accelerate a chemical reaction *via* activation of a photocatalyst, which remains unchanged [1, 2]. A photocatalytic reaction can be either homogeneous or heterogeneous depending on whether the photocatalyst and the reactants are in the same phase or not. Homogeneous photocatalysis is a process where reactants and photocatalyst are in the same phase, while in heterogeneous photocatalysis reactants exist in different phase of that of the photocatalyst. Homogeneous photocatalysts are known for their ability to work at mild conditions (room temperature, ambient pressure). However, they contain expensive elements and the difficulty in the separation process of the photocatalyst from reactants and products is deterrent for their reusability. On the other hand, heterogeneous photocatalysts are usually made of abundant elements and benefit from facile separation from the reaction mixture. For these reasons, heterogeneous photocatalysis is considered as a safe and sustainable technology in industrial applications. Heterogeneous photocatalysis is of significant importance for the world's economy and it has been widely used in several chemical transformations, including pharmaceuticals, fragrances, fuels and food industry.

In principle, when a semiconductor photocatalyst absorbs photons of energy equal or greater than the band gap of the photocatalyst, electrons are excited from the valence band (VB) to the conduction band (CB) of the semiconductor [3]. This results in leaving a positive hole in the valence band and a negative electron in the conduction band, creating electron-hole pairs [4]. VB is the highest occupied energy band filled with

electrons while CB is the lowest empty band with no electrons at the ground state. The photo-excited electron-hole pairs can undergo two different routes: i) recombine in the surface or bulk of the semiconductor just in a few nanoseconds causing a negative effect on the efficiency of the photocatalytic reaction; or ii) travel to the surface of the semiconductor photocatalyst given the long-enough charge carrier lifetime. In the latter case, the photo-generated electrons and holes can initiate reduction or oxidation (redox) reactions, respectively, on the surface of the photocatalyst [5]. Fig. 2.1 illustrates the mechanism of electron-hole pair formation in a semiconductor during a photocatalytic process. The photo-excited electrons participate in reduction reactions to form superoxide radicals (O_2^-), while positive holes participate in oxidation reactions to produce hydroxyl radicals (˙OH).
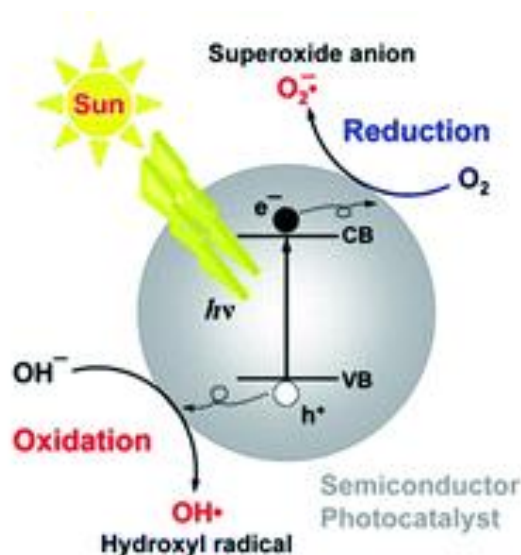
Figure 2.1. Schematic representation of photoactivated semiconductor mechanism [6].

Nevertheless, from a thermodynamic point of view, the conduction and valence band-edge position of the semiconductor photocatalyst should be compatible with the redox potentials of the targeted chemical compounds. Particularly, the conduction band-edge should lie at a higher (more negative) position, while the valence band-edge should be at a lower (more positive) position than the electrode potential of electron acceptor or donor to initiate reduction or oxidation reaction respectively [7]. Fig. 2.2 depicts the conduction band and valence band positions of typical semiconducting photocatalysts with respect to the reduction-oxidation potentials for water-splitting reaction.

Figure 2.2. Band-edge positions of some semiconductors relative to the energy levels of several redox couples in water [5].

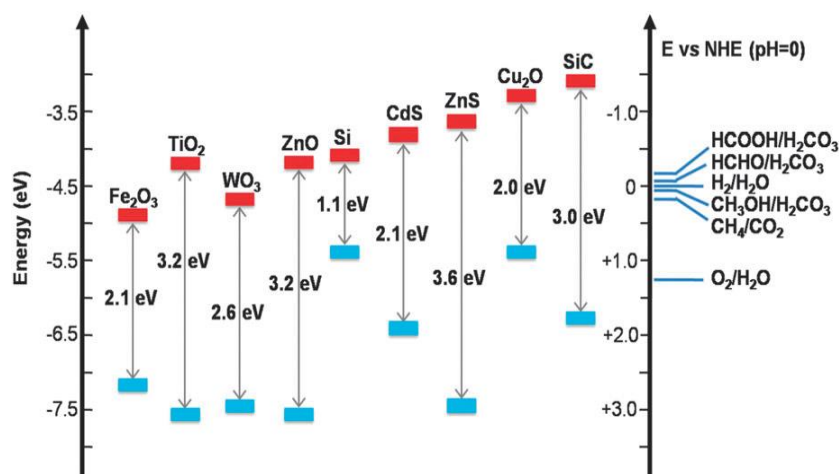As it can be seen from Fig. 2.2, semiconductors with wide band gap such as TiO_2 and ZnO can form both ·OH and O_2^- radicals, while narrow band gap semiconductors can produce only one type of radical. However, wide band gap semiconductors such as TiO_2, which has been widely employed as photocatalyst, face problems such as limited absorption in the visible region and high recombination of photogenerated charge carriers, resulting in low product selectivity and low reaction rate [8]. In this direction, many efforts including semiconductors heterostructure and doping semiconductors with metal and non-metal elements have been made to enhance light utilization, and thus, promote the efficiency of photocatalytic processes [9]. The deposition of plasmonic metals on semiconductor surface is another promising approach to increase the activity of metal oxide semiconductors and subsequently the efficiency of photocatalytic processes [10, 11]. Plasmonic metal NPs that benefit from enhanced light absorption and interfacial electron transfer will be discussed in detail in section 2.2. In addition to the importance of the photocatalysts, the efficiency of a photocatalytic process is greatly influenced by parameters such as mass transfer and light utilization. In this case, attention should be focused on photoreactor design to maximize mass transfer and light utilization. Photoreactor design is a significant factor affecting these parameters and so far, it has been shown that the conventional batch type reactors that have been mainly utilized in several photocatalytic reactions suffer from poor mass transfer and non-uniform light distribution [12]. Furthermore, the type of light source has a great impact on the efficiency of photocatalytic applications. So far, problems such as long reaction time, long-term power instability and increased energy consumption were identified when conventional lamps employed as irradiation source to drive photocatalytic

reactions [13, 14]. The development of cost-efficient photocatalytic process under mild conditions with high reaction rate and high selectivity remains a significant challenge. Therefore, intensive research efforts have been devoted to overcoming these challenges in order to enhance the photocatalytic efficiency.

2.2   Plasmonic metal nanoparticles

Plasmonic metal nanoparticles (NPs) have been used and demonstrated to be a promising material in selective organic transformations under mild conditions [15]. The deposition of nanostructured plasmonic metals (*i.e.,* Au, Ag, Pd and Cu) on semiconductors could enhance the photocatalytic activities by facilitating the transfer of photo-induced carriers through localized surface plasmon resonance (LSPR), and therefore, inhibiting the recombination of the photogenerated electron hole pairs [16, 17]. LSPR is the coherent resonant oscillation of free conduction electrons confined on the surface of plasmonic metal NPs, which is induced by the interaction with the electromagnetic field of the incident light (Fig. 2.3) [18]. At resonance, when the frequency of metal surface electrons oscillating against the restoring force matches the frequency of incident light, the near-field region of plasmonic NPs is amplified. LSPR is an optical phenomenon, which occurs when the size of metal NPs is smaller than the wavelength of the incident light.
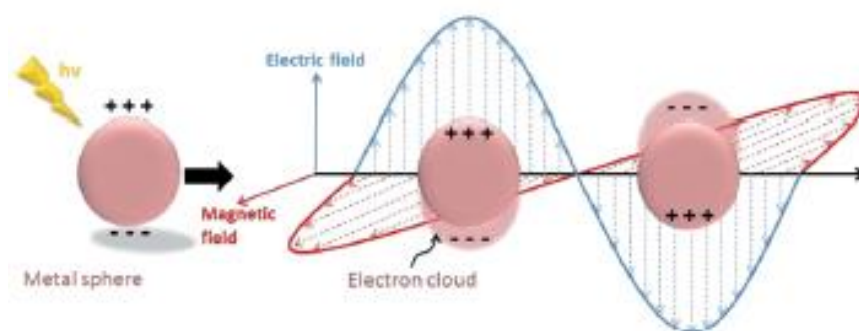
Figure 2.3. Schematic illustration of LSPR excitation on metal NPs [19].

In terms of intense visible light absorption, Au, Ag and Cu are suitable candidates [17, 20, 21]. For instance, the LSPR absorption peaks of Ag, Au and Cu spheres with diameters of 38, 25 and 133 nm are located at approximately 420, 520 and 610 nm respectively [16]. Among the noble metals, Au nanoparticles are the most attractive metal used in photocatalytic processes due to their chemical stability, in addition to their high absorption and scattering properties [22].

Relevant studies have shown that apart from the nature of metals, their size, shape, interparticle distance and surrounding media have significant effect on the LSPR properties (wavelength and intensity), resulting in different photocatalytic activity [16, 23-26]. Particularly, as the size of nanoparticles increases, the intensity of the produced electromagnetic field alters causing a red-shift (longer wavelength) in the LSPR frequency (Fig. 2.4c). In addition, by changing the shape of NPs from spheres to cubes or wires, not only the LSPR wavelength shifts, but also the number of LSPR peaks increase (Fig. 2.4b) [16]. Furthermore, different surrounding media cause blue or red shift of the LSPR absorbance of Ag depending on the refractive index of the solvent (Fig. 2.4d) [24]. Therefore, LSPR wavelength can be designed and controlled for specific applications.
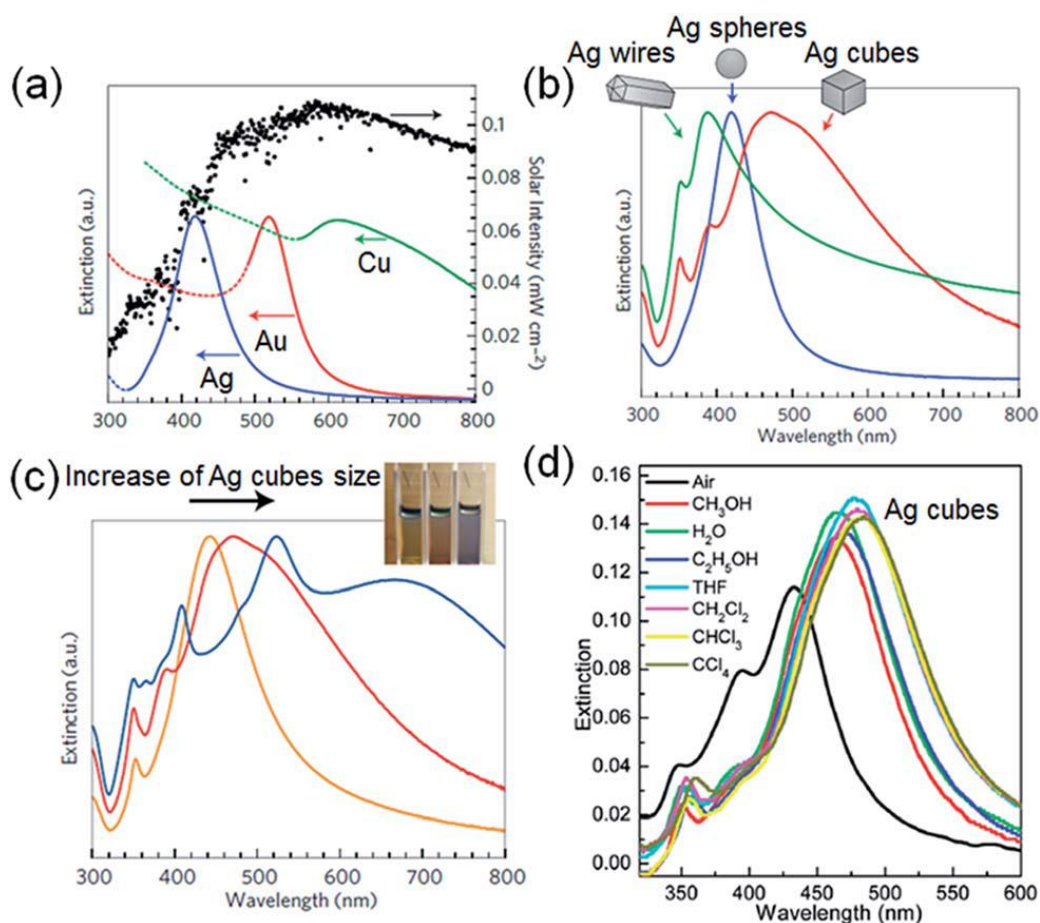

Figure 2.4. The plasmonic wavelength dependence of metal nano-structures on their (a) metal species (b) shapes and (c) sizes. (d) The effect of the surrounding media on the plasmonic wavelength of Ag nanocubes [16] [24].

Generally, energetic electrons are generated at the surface of metal NPs in 5-100 fs *via* LSPR excitation and remain in hot state for 0.5-1 ps before travelling back to lower energy levels [27]. If electrons manage to be transferred to the reactant molecule adsorbed on the surface of metal NPs during this time, then chemical transformations can be induced under visible light irradiation [28, 29].

The photocatalytic route *via* SPR can be explained through four possible mechanisms: 1) injection of hot electrons, 2) electric field amplification, known as Plasmon Resonance Energy Transfer, 3) scattering of resonant photons and 4) plasmonic heating process [30]. Hot electron mechanism and electric field amplification are near field effects, which can be controlled by engineering the interface between the metal and semiconductors while light scattering is a far field effect that increases the effective optical path length of incident light and therefore enhances the photon absorption of semiconductors. Additionally, the plasmonic metal nanoparticles can generate plasmonic heating, known as photothermal effect, to drive photocatalytic reactions due to their strong localized surface plasmon resonance effect.

2.2.1   Photo-induced charge transfer

Generally, plasmonic metal NPs can improve the photocatalytic activity of semiconductors under both UV and visible light irradiation through photo-induced charged mechanism *via* electron transfer either from semiconductor to metal or from metal to semiconductor, reducing electron-hole pair recombination. When the metal and semiconductor come in contact, a potential energy barrier that prevents electrons passing through them is formed at the metal-semiconductor junction known as Schottky junction [30]. Fig. 2.5 illustrates the energy band diagram of a typical n-type semiconductor-metal Schottky junction. The height (Φ_B) of the potential Schottky barrier is given from the following equation:

$$\Phi_B = \Phi_M - X_{SM}$$

where Φ_M is the working function of the metal, described as the required energy to transfer an electron from the metallic Fermi energy (E_F) to the vaccum Energy (Evac) and X_{SM} is the electron affinity, defined as the energy difference between the minimum conduction band (CB) and the Evac.
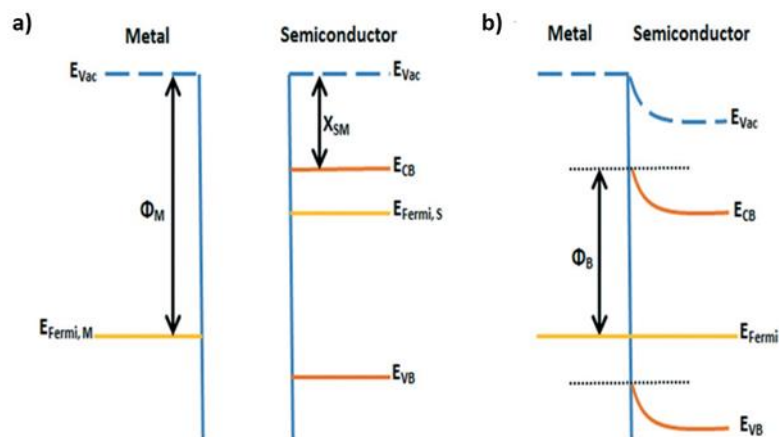
Figure 2.5. Formation of the Schottky barrier between n-type semiconductors and metals (a) before contact and (b) after contact [30].

Upon light illumination, photogenerated electrons are transferred from the semiconductor to the contacting metal through the Schottky junction, leading to a shift of the Fermi level of the metal towards that of the semiconductor, until the Fermi level of the semiconductor reaches equilibrium with that of the metal.

The Schottky barrier acts as an effective electron trap where the electron is not able to travel back to the semiconductor. In this manner, metal serves as an electron sink preventing electron-hole pair recombination and prolonging electron lifespan for the photocatalytic reaction. The Fermi level of the metal should be sufficiently lower than the semiconductor CB to obtain efficient electron transfer across the Schottky barrier. For this reason, metals with large work function values such as Pt (5.93 eV), Au (5.31 eV) and Ag (4.74 eV) are mainly utilised to form heterojunctions with semiconductors.

For example, Hirakawa *et al.* explored the electron transfer in the presence of Ag/TiO$_2$ nanostructure using UV irradiation [31]. The authors reported a shift in the plasmon peak position due to accumulation of electron density of metal through charge transfer from TiO$_2$ to Ag under UV irradiation. It has been concluded that the improvement of the photo-activity of TiO$_2$ by coupling with plasmonic metal under UV irradiation stems from the electron transfer from the semiconductor to the metal, leading to efficient separation of charge carriers between TiO$_2$ and Ag NPs.

In the case of visible light excitation, the enhancement in the photocatalytic activity can be attributed to the injection of hot electrons from the metal to the semiconductor (Fig. 2.6). Particularly, upon visible light irradiation, high-energy electrons are produced in plasmonic NPs by LSPR excitation. Subsequently, the generated hot

electrons are injected into the conduction band of the semiconductor photocatalyst leaving the plasmonic metal positively charged resulting in generation of holes in the plasmonic metal [32, 33]. The electrons in the semiconductor's conduction band and the holes left in the metal participate in reduction and oxidation reactions respectively. Tian and Tatsuma demonstrated for the first time the hot electron injection mechanism to explain the photoactivity of Au/TiO_2 in an electrochemical cell [33]. Since then, many research groups such as Zheng *et al.* and Wang *et al.* interpreted the photocatalytic activity of metal-based semiconductors through this mechanism [34, 35].
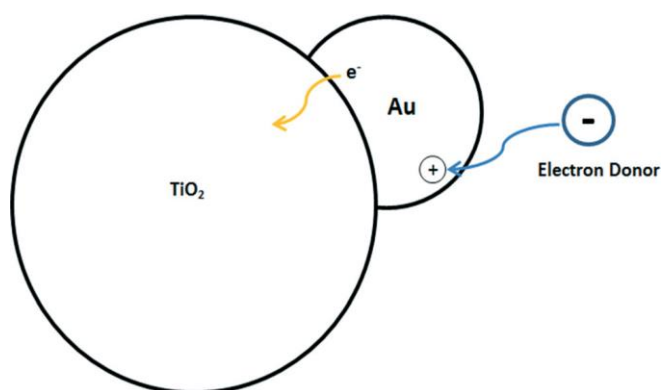

Figure 2.6. Mechanism of hot electron transfer [33].

2.2.2 Near-field enhancement mechanism

Another mechanism to explain the enhanced photocatalytic performance over plasmonic metals supported on metal oxides can be ascribed to the plasmon induced electromagnetic field enhancement near the surface of metal NPs in the semiconductor, which increased the generation rate of the photoexcited electron holes at the semiconductor. Plasmon Energy Resonance Transfer (PRET) mechanism is utilised to interpret the enhanced photocatalytic reaction *via* the presence of an intense electric field near the metal [30]. Particularly, plasmon energy is transferred to the semiconductor through the intense electric field created near the metal by incident irradiation, promoting the generation of electron hole pairs near the surface of the semiconductor *via* the dipole-dipole interaction between the metal and the semiconductor. PRET can amplify the electric field in small well-defined locations, named as hot spots. Based on Fine Difference Time Domain (FDTD) simulation study of Hou *et al.* (Fig. 2.7), the electric field in the hot spots shows up to 1000-fold enhancement compared to the incident electric field on the semiconductor surface, resulting to 1000 times more electron-hole generation rate and photoabsorption compared to that under normal incident light [36].
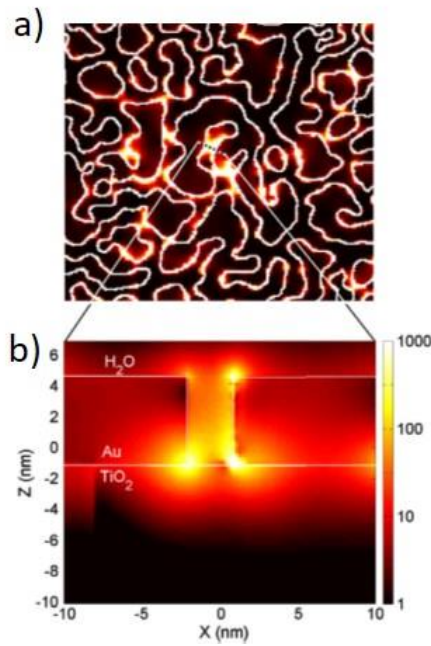
14

Figure 2.7. a), b) Electric field intensities at the Au–TiO$_2$ interface calculated using the FDTD simulation method [36].

According to the literature, the overlap of LSPR band of the metal with the band gap of the semiconductor and the light source spectrum is required to initiate the PRET mechanism and this overlap is related to the photoactivity of a reaction. Fig. 2.8 illustrates the proposed overlapping model defined using FDTD optical simulations by Ingram et al [37]. The authors reported that the overlap for Ag/N-TiO$_2$ absorbance is larger in comparison to that of Au/N-TiO$_2$, leading to a higher degradation of methylene blue than that of Au/N-TiO$_2$.
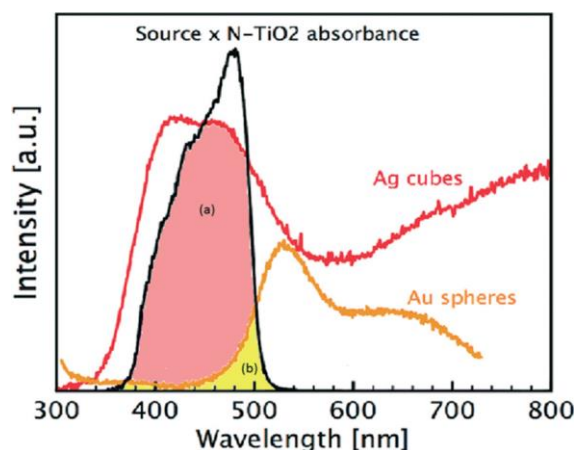

Figure 2.8. The optical overlap of the building block for the prediction of photocatalytic activity. (a) Source × N-TiO$_2$/Ag cube absorbance overlap. (b) Source × N-TiO$_2$/Au sphere absorbance overlap [38].

2.2.3   Photon scattering

Plasmonic NPs show excellent scattering properties due to the SPR excitation. Upon light illumination on the plasmonic metal, incident resonant photons can be spread out, leading to an increase in their optical path length. In this way, the plasmonic metal serves as a nano mirror. A number of photons which are not absorbed by the semiconductor, could be scattered by the plasmonic metal providing them the ability to travel through the semiconductor [39, 40]. As a result, the light absorption is improved causing a subsequent enhancement in the photocatalytic efficiency. Generally, light scattering depends on particle size and increases with larger particles. This means that plasmonic NPs should have a size large enough to cause intense light scattering [41]. For example, Christopher *et al.* investigated the enhancement of methylene blue degradation due to photon scattering from Ag to TiO_2 [42]. The authors reported that Ag cubic-shaped particles presented higher methylene blue degradation than that of Ag spheres because cubic particles could scatter light in a more efficient way. Fig 2.9 illustrates the effect of size and shape of the metal on the scattering efficiency calculated using FDTD method. As it can be seen, by increasing the size of Ag from 30 to 100 nm, scattering of photons is more efficient. Additionally, Warren and co-workers claimed that a metal size of at least 100 nm is required to maximize the possibility of scattering over the other effects [43].
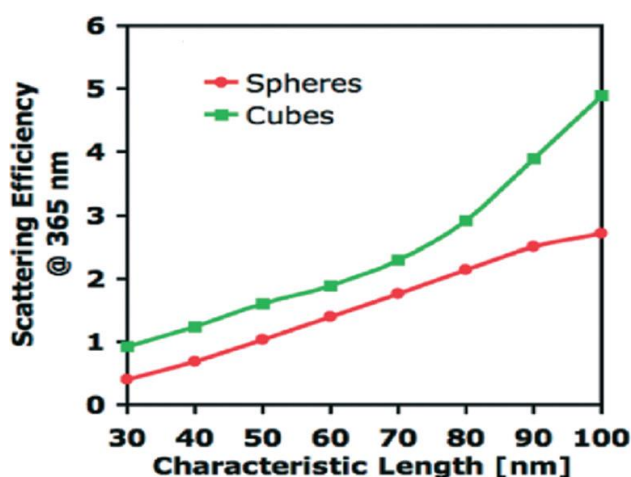

Figure 2.9. The relationship between the characteristic length of the sphere and cube shaped particles and their scattering efficiency calculated using a Finite-Difference Time-Domain (FDTD) method at 365 nm [42].

16

2.2.4 Plasmonic heating effect

The generation of SPR in plasmonic metal nanoparticles under light irradiation can result in alteration of the temperature of the surrounding medium of plasmon metals. When the hot electrons do not have sufficient energy to jump into the semiconductors and participate in the photocatalytic process they remain inside the metal [44]. In this case, the hot electrons undergo relaxation processes by a series of electron-electron (10-100 fs) and electron-phonon (100 fs – 1ps) interactions converting the absorbed light into heat [45]. The produced heat, known as plasmonic heating effect, is localized in the near vicinity of the NPs surface, resulting in photothermal conversion. Research has shown that metal NPs, such as Au, Ag and Cu with very low NPs concentration exhibit considerable photothermal performance due to their unique characteristics such as absorption of photons [46]. Metal nanoparticles convert the absorbed photons to heat energy, which is then transferred to surrounded medium, increasing the temperature. It should be noted that inter-particle distance, which depends on distribution of NPs, plays a significant role in the photothermal behavior of plasmonic NPs due to the presence of two different effects: thermal superposition effect and plasmonic coupling effect. The improved thermal accumulation caused by the heat which is transferred from nearby hot NPs can be described as the thermal superposition effect while the effect of plasmonic coupling can be considered as the thermal accumulation related to the plasmonic coupling of nearby NPs, which can enhance the local electromagnetic field and production of heat. In case of low NPs concentration, where the average inter-particle distance is larger, the two effects can be considered as negligible [47-49]. The effect of plasmonic heating on photocatalytic activity of metal NPs can be identified by measuring the local temperature near the surface of the metal. Many studies reported that plasmonic heating of plasmonic metals can promote the photocatalytic performance because the temperature rise can contribute to the reaction rate enhancement. For instance, Kim *et al.* demonstrated the use of Au NPs as efficient photothermal heating materials to catalyze the 4-nitrophenol under solar light irradiation [50]. The authors reported that the Au loaded filter papers exhibited an improved catalytic activity in 4-nitrophenol reduction caused by the photothermal effect of loaded Au NPs. In another study, Yen and co-workers determined that the rate of the catalytic reaction between hexacyanoferrate (III) and thiosulfate increased in the presence of Au NPs which act as photothermal heaters [51].

2.3 The role of light irradiation in photocatalysis

The type of light irradiation is one of the most important parameters affecting the overall efficiency of the photocatalytic process [52]. Photocatalysis can be carried out using either solar or artificial light such as mercury lamps, halogen lamps, light-emitting diodes (LEDs) and light amplification by stimulated emission of radiation (laser).

To date, most of the research work reported on photocatalysis mainly focuses on light sources that emit over a broad spectral range. Solar light is a clean, abundant and green energy source. Although solar photocatalysis has been demonstrated to be an effective technology for many applications, including CO_2 photoreduction, hydrogen production and water purification, there are still challenges to overcome in order to enhance the overall efficiency. For instance, the most common based photocatalysts including TiO_2 and ZnO absorb light only in the UV region, which means that most of the solar light lies outside of their band gap [18, 22].

Over the past twenty years, artificial light sources have attracted much attention in the field of photocatalysis due to their high intensity, around the clock availability and appropriate range of wavelength. However, conventional lamps with broad spectrum, such as mercury and halogen lamps, have high-energy consumption, include high toxic substances and they are not effective in terms of photon utilization for chemical processes [53]. More recently, LEDs producing light in a narrow spectrum and having low operating temperature, have been used as a safer competitive source of light to conventional lamps [54]. Nevertheless, the utilization of LEDs still hinder many limitations in terms of high cost of experimental set up as well as light harvesting efficiency. Particularly, the light output of an LED comes from spontaneous emission, which means the produced photons travel in different directions and disperse their power over a large area resulting in an energy loss.

Several studies have revealed the need to utilize more energy efficient light sources as an alternative to the existing conventional lamps in order to develop commercially feasible chemical processes for a large number of applications. Recent research has shown that the use of monochromatic laser source in chemical reactions can address several challenging issues including low reaction rate and low photonic efficiency [14]. Lasers gained interest quickly, resulting in a fast progress of laser technology due to their special properties, such as monochromaticity, coherence, directionality and high intensity that traditional artificial light sources do not possess. In particular, these properties make laser light suitable for a great variety of applications offering high

selectivity of the desired product, localized heating with low operating temperature avoiding huge energy consumption and high reaction rate.

2.3.1 Natural and artificial light sources

In this section, a detailed description and comparison of the different light sources is presented. The optimal use of solar or artificial light depends on the specific application and the different requirements needed.

- Natural light sources

Sunlight is a renewable and free energy source, with a broad spectrum that gives the opportunity to use a large variety of photocatalysts with different band gaps for several photocatalytic applications. Many studies reported the utilization of solar light as primary energy source to catalyse CO_2 reduction and split water into hydrogen and oxygen under ambient conditions, without the need of using high cost artificial light [55]. Both photocatalytic CO_2 reduction and water splitting are uphill energy reactions that need a significant input of energy. Thus, solar light can be employed as an effective source to produce clean hydrogen and low-cost hydrocarbon fuels known as solar fuels through photocatalytic water splitting and CO_2 photoreduction, respectively [56, 57]. In this way, solar energy is harvested and stored directly in chemical bonds.

- Artificial light sources

Several studies have reported the efficient use of artificial light sources, such as mercury and halogen lamps, LEDs and lasers compared to direct sunlight processes in photocatalytic reactions. Particularly, applications such as photocatalytic degradation of organic pollutants, oxidation processes, drug formation and medical therapy require a continuous light source with relatively high intensity, characteristics that can be easily provided by artificial light [58-60]. In contrast, solar light provides low energy density and its availability depends on weather and seasonal conditions which may not be in accordance with the required energy demands [55].

Another crucial parameter affecting significantly the chemical process is the light wavelength. Photocatalysts require light emitted within a particular wavelength of radiation in order to generate active species and drive the chemical reaction. Artificial light sources are capable of supplying a quite narrow wavelength (LEDs ~50 nm), a very narrow wavelength (Lasers ~5 nm) or a suitable range of either UV (~200-400 nm) or visible (~400-800 nm) irradiation using conventional lamps (mercury/halogen). The

light wavelength emitted by artificial lamps can match the absorption spectra of the photocatalyst contrary to the wide spectrum of light emitted by sun, which is mostly located outside the band gap of semiconducting photocatalysts. A comparison of the main characteristics between laser, LED and conventional lamps employed as light source in photocatalytic applications is illustrated in Table 2.1

Table 2.1. Comparison of the main characteristics between Laser, LED and conventional lamps employed as light source in photocatalytic applications.

	Conventional lamps (mercury/halogen)	LED	Laser
Wavelength	Broad band ~200-400 nm (UV) ~400-800nm (Visible)	Narrow ~50nm	Monochromatic ~5nm
Coherence	No	No	Yes
Directionality	No	No	Yes
Intensity	Up to 250 mW/cm^2 (Xe arc lamp: several hundred mW/cm^2)	Up to 150 mW/cm^2	Up to 10 W/cm^2
Lifetime	~500-2000 h	~50000-100000 h	>70000h

i) Conventional lamps

Contrary to solar irradiation, conventional lamps emit light in a narrower spectrum, which, however, is very broad compared to LEDs and lasers. Mercury and Halogen lamps with continuous output range from UV to near Infrared (IR) wavelengths are the most common artificial light sources to study the photocatalytic degradation of organic pollutants. Bhaktende *et al.* reported a much faster degradation of nitrobenzene using artificial UV lamp instead of solar light because of the higher percentage of UV [61]. However, long reaction time, long-term power instability and increased energy consumption have been observed using conventional lamps, resulting in low overall efficiency [62, 63]. For example, a 4-fold decrease of methanol production reported by Gondal and co-workers under Xenon mercury (XeHg) lamp compared to UV laser irradiation [64].

ii) Light Emitting Diodes (LEDs)

Recently, there has been growing interest in the development of LEDs, which is a solid-state light source based on p-n junction semiconductor with a forward bias applied [54]. LED, being a reliable and environmentally friendly light source represents an alternative to traditional lamps in terms of energy efficiency for photocatalytic applications. Additionally, LEDs have a rising power output, produce a relatively narrow range of wavelength within the UV, visible or infrared region and benefit from low operating temperature, low energy consumption and quite longer lifetime compared to conventional lamps [65]. UV LEDs have been utilized successfully for the photocatalytic degradation of organic compounds in water and air. For instance, Johnson carried out the first purification of organic compounds in air under UV LED irradiation achieving 80% of acetaldehyde and 95% decomposition after 20min [66].

iii) Light Amplification by Stimulated Emission of Irradiation (laser)

Laser light operates either in continuous or pulsed mode and consists of an optical spectrum with a very narrow width. The spectrum emitted by laser can range from UV to mid IR wavelengths. Energy, environmental and medical processes have been conducted in the presence of monochromatic laser light, achieving high selectivity, faster reaction rate and enhanced overall efficiency attributed to its unique properties.

Lasers emit light in a very narrow band centered around a single wavelength, which means that radiation emitted by laser is monochromatic [67]. In contrast, LEDs tend to produce a narrow range of wavelength and conventional lamps have a wide spectral output. Lasers produce light in a coherent manner, which asserts that the emitted photons are all of the same frequency and in phase with each other while LEDs and conventional lamps produce photons that travel in different time and phase [68]. Additionally, laser light is traveling only in one direction, thus it can transfer energy that remains efficiently concentrated, on a small region with minimum loss by dispersion [67]. On the other hand, LEDs and conventional lamps emit photons in many directions, and distribute their power over a large area causing waste of energy [69]. It should be noted that coherent light is much more concentrated and powerful even though the same quantity of energy is derived from both coherent and incoherent light.

Finally, since the beam emitted from a laser has small divergence angle, the light energy is centered on a very small region which means that the light beam is highly collimated [67]. This concentration of the beam results to a much higher intensity for

the laser light (up to 10 W/cm^2) compared to the ordinary light sources (LEDs ~ up to 150 mW/cm^2, conventional lamps ~ up to 250 mW/cm^2).

Considering the unique properties of laser light, it is important to point out that the use of an effective irradiation source such as laser can lead to a better control of the experimental conditions while at the same time offers the possibility to make the photocatalytic process more efficient in a wide range of applications.

2.3.2 Benefits of using laser as irradiation source in photocatalysis

The unique properties described above enable laser a promising irradiation source for several applications in terms of achieving localized heating, high selectivity of the desired product and high reaction rate, as will be described below.

2.3.2.1 Localized heating

The effect of localized heat generation under laser light in combination with plasmonic nanoparticles such as metals has been investigated over the last ten years [70]. The novel aspect of this process is that the directionality and high intensity of laser light allow localized heating in space and time, which could result in high-energy chemical process. Plasmonic localized heating can be achieved either by pulsed or continuous wave lasers (CW). Although it has been reported that CW lasers can supply better controllability of the heating process, it has been showed that high intensity CW laser might damage both nanoparticles and supporting material [68].

Laser interaction of plasmonic nanoparticles occurs in the following stages [71]: Plasmonic nanoparticles absorb incident laser light resulting in heating them up instantaneously. This heating can be rapidly transferred to the surrounding medium. The heating of nanoparticles can be explained by electron dynamics and lattice vibrations generated from incident light. Upon laser irradiation, the nanostructures perform as nanolenses (metal nanoparticle chains of different sized particles), causing electromagnetic field improvement in their surroundings which are several orders of magnitude stronger in comparison to that of the incident field. Nanolenses are self-similar arrangements of at least three nanoparticles, where there would be plasmon modes with a very strong field localization in the gap between the two smallest particles (Fig. 2.10) [72].
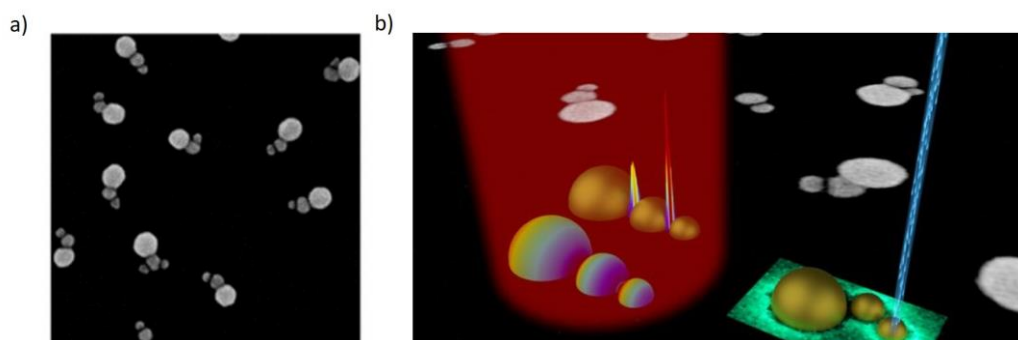
Figure 2.10. a) SEM image of Au nanolenses and b) Electrical field enhancement plot of gold nanolenses (gold nanoparticles with different particle radii) [72].

The quantity of produced heat can be controlled by altering several parameters, such as particle shape and size and at the same time laser intensity, wavelength and pulse duration [71]. In this way, the interaction of laser light with plasmonic metals, besides the enhancement in the electromagnetic field, permits the temporal and spatial control of localized heating. The important effect of this interplay on light manipulation, heat control and nanofabrication was reviewed thoroughly by Hashimoto and co-workers [71].

Femtosecond and nanosecond lasers can operate as tools to explore the dynamics and processes induced by the excitation of plasmon nanoparticles. In this regard, many studies investigated the reshape of Au nanorods to spherical particles in aqueous solution under nanosecond pulsed laser irradiation, which was attributed to a photo annealing process [73]. Additionally, the mechanism of nanosecond laser-induced size reduction and fragmentation of plasmonic nanoparticles was presented by Caupin and co-workers [74]. The effect of the interaction of laser with plasmon nanoparticles on the surface modification [75] or the deposition of Au nanoparticles [76] on glass substrate employing pulsed laser irradiation was reported. Finally, Zhou *et al.* showed that laser on a timescale of femtoseconds can be used to characterize spatial heating associated with plasmonic excitation [77].

2.3.2.2 Selectivity

In chemical processes, selectivity is one of the most important factors, as it is directly related to the yield and generally to the conversion efficiency of the reaction. The term selectivity can be defined as follows:

$$Selectivity = \frac{moles\ of\ the\ desired\ product\ formed}{moles\ of\ other\ compounds\ formed} \qquad (2.1)$$

23

One of the most significant advantages using laser light in photocatalytic processes such as CO_2 conversion into fuels or drug production is the enhancement of the selectivity of the product formed which is mainly ascribed to the monochromatic characteristic of laser light. It is interesting to note that adjusting the light wavelength, affects the selectivity of the chemical process by possibly erasing the formation of side products at a specific wavelength with higher energy that can be provided to activate the photocatalyst. In this direction, Gondal *et al.* showed that methanol was the only obtained product during CO_2 reduction process in the presence of laser light [64, 78]. The authors proposed that the monochromatic light could contribute to the production of photogenerated electrons with centred reduction energy, which strongly supports the formation of one specific compound while under broad band irradiation source with many wavelengths, electrons with different energies might be photogenerated, resulting in the generation of different hydrocarbon products. The same research group carried out additional studies using laser in the presence of different photocatalysts and concluded that monochromatic irradiation photogenerates electrons with a centered reduction energy that favors the production of a specific chemical product, enabling high selectivity of the desired product.

Additionally, many research groups have shown that the use of plasmonic nanostructures, known for their unique surface catalytic properties and strong light-matter interactions can further assist reaction selectivity for laser irradiation photocatalytic processes. In this regard, Luque and co-workers reported the amidation of benzaldehyde and morpholine for the production of 4-benzoylmorpholine using Au/SiO_2 as catalyst under laser irradiation [59]. By selectively activating Au nanoparticles, the desired product named 4-benzoylmorpholine was formed after 4h of laser irradiation with an impressive 99% selectivity. It was suggested that the increased selectivity was due to the localized heating effect achieved under laser irradiation, which might provoked the fast desorption and spreading of the intermediates in the surrounding medium deterring them to react further [59, 79].

2.3.2.3 Reaction rate

Many groups have reported that the utilization of a high photon flux source like laser could be a promising alternative light source to accelerate the rate of a chemical reaction. Gondal *et al.* suggested that by employing a high photon flux irradiation source like laser, more photons of particular wavelength of the incoming light are absorbed by the photocatalyst in a shorter time causing the excitation of more active

catalyst particles [80]. In contrast, broadband light can deliver low average power to the reaction compared to that of laser light possibly related to its high divergence [81].

In order to have a better understanding of the influence of laser energy, the impact of laser light in the production of methanol in comparison with XeHg lamp irradiation is illustrated in Fig. 2.11a-b [64]. Maximum methanol concentration (1.252 mM) was reached after 90 min laser irradiation, which was 4 times higher compared to the 0.375 mM methanol produced under XeHg lamp even after 120 min. According to the authors, the high conversion is attributed to the monochromaticity and high intensity of laser beam as the increased number of photons (5.364×10^{19} photons/min under 40 mJ/pulse of 355nm laser and 1.39×10^{19} photons/min under 500W XeHg lamp) could lead to a rise in the production of methanol molecules.
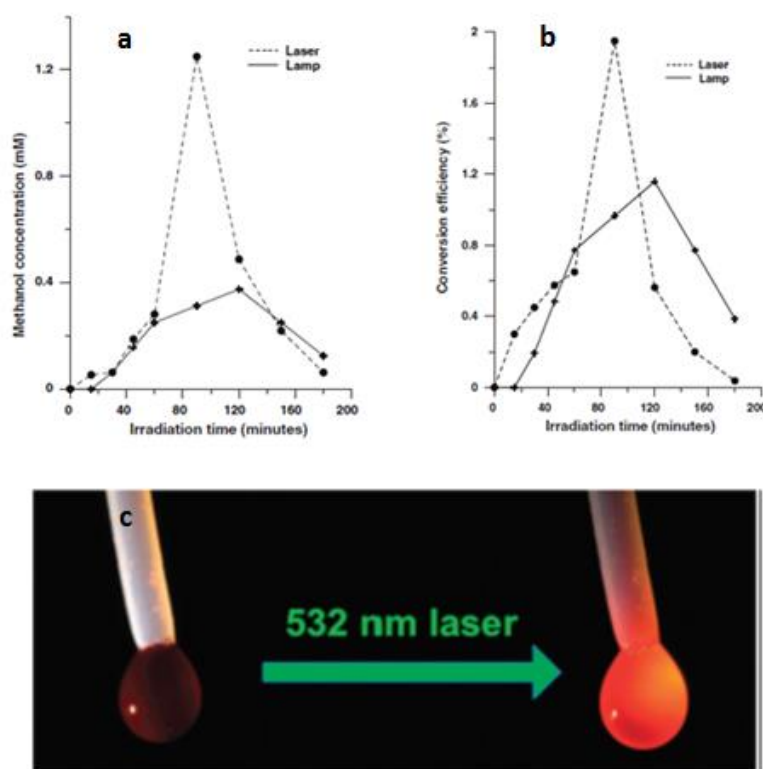
Figure 2.11. a) Methanol concentration and b) conversion efficiency versus time using laser and XeHg lamp irradiation [64], c) photo of drop before (resazurin) and during laser excitation (resorufin) [82].

Additionally, many efforts have been conducted to accelerate gas [83] and liquid [82] catalytic processes at room temperature through cooperative effect of intense laser excitation on plasmonic nanoparticles, which is mainly attributed to the localized heating process achieved. In this way, Trammer *et al.* reported a 2-fold increase in the catalytic rate of hydrolysis of methyl parathion by excitation of the plasmon absorption band of Au nanoparticles under green laser irradiation [84]. Additionally, Scaiano and co-workers observed the dramatic acceleration of the reduction reaction from resazurin

to resorufin under laser excitation employing Au NPs (Fig 2.11c) [82]. Particularly, an impressive 80% conversion was achieved under laser pulsed irradiation (10 J mL^{-1} , 50 mJ per pulse, ~ 10 μL drop) within a few nanoseconds, while under LED irradiation (500 J mL^{-1}) only 50% conversion was observed. It should be noted that in plasmon assisted chemical reactions under laser irradiation the highly dependence of reaction rate on laser power and wavelength was ascribed to the electromagnetic enhancement and the higher amount of hot electrons generated on the surface of plasmonic nanoparticles respectively.

To summarize, lasers produce monochromatic, coherent, high-intensity light with low beam divergence, properties which are of critical importance for an efficient light source in photocatalytic applications. However, it should be noted that the use of laser light in heterogeneous photocatalysis has been limited so far due to high cost of lasers, small illuminated area that requires a specific reactor design and safety concerns associated with the use of lasers, issues that should be taken under consideration [65].

2.4   Reactor design

In photocatalytic processes another significant engineering challenge is the photoreactor design which can influence the overall photocatalytic efficiency. One key parameter which determines the types of photoreactors that can be used in photocatalytic processes is the mode of operation (batch, semi-batch or continuous flow).

So far, the most common approaches for chemical transformations in pharmaceutical industry and particularly for the selective oxidation of aromatic alcohols are based on the utilization of batch reactors [85, 86]. For example, Tao *et al.* investigated the photocatalytic oxidation of benzyl alcohol in the presence of Pd/BiVO$_4$ under 300 W Xenon lamp (λ= 360-780 nm) [87]. The authors reported benzyl alcohol conversion (71.8%) with 99% benzaldehyde selectivity after 8 h irradiation. While batch reactors are used in synthetic chemistry due to their versatility, they are mainly favored when a process is conducted in small scales. Batch processes have high cost of labor per unit of production due to non-productive operations and low mass and heat transfer rates, resulting in long reaction time and decreased product yield, which are limiting factors for scalability. Additionally, the presence of hazardous compounds in large volumes arises safety issues and environmental concerns.

In this direction, many research efforts are devoted to design and fabricate continuous flow reactors with significant processing advantages that satisfy the demands for a

photocatalytic reaction with high conversion [12, 88]. For instance, Singh *et al.* studied the photocatalytic degradation of Rhodamine B in the presence of Ag_3PO_4 nanoparticles using a continuous flow microreactor [89]. The authors reported an efficient dye degradation of 97% within just 15 min of visible light irradiation.

For reactor development, many factors should be taken under consideration including reactor geometry, material of construction and flow rate. Flow reactors, being an alternative approach to batch type reactors, benefit from high heat and mass transfer and good control of residence time, enabling high throughput with excellent selectivity and precise reaction control [90, 91]. Continuous flow conditions allow unprecedentedly high degree of control over reaction for the production of high-value chemicals. These merits create unique opportunities to enhance the existing chemical routes in terms of safety, waste minimization and efficiency and enable a large variety of green chemical syntheses using efficient synthetic protocols.

2.5   Photocatalytic oxidation of alcohols using plasmonic metals

Selective oxidation of alcohols represents one of the most significant transformations in the chemical industry with aldehydes and ketones being the most valuable targets. As discussed in section 1.2, Chapter 1, benzaldehyde (C_6H_5CHO) is one of the most important aromatic molecules used as valuable intermediate in pharmaceuticals, fragrances and food industry. Photocatalytic oxidation of benzyl alcohol to benzaldehyde has been extensively investigated using several photocatalysts with significant improvements. Plasmonic metal NPs have been found to be effective and selective photocatalysts to catalyze the oxidation of alcohols to aldehydes under light irradiation. The anchoring of noble metals (Au, Ag, Pt, Pd, Cu) on semiconductors extends the light absorption to the visible region, promoting the formation of photoexcited electrons or plasmonic hot electrons and facilitates the separation of photoinduced charge carriers at the interface between metal and semiconductor [92].

In 2011, Kominami developed a green route for benzyl alcohol oxidation in the presence of $Au@CeO_2$ achieving 99% conversion and 99% selectivity after 20 h reaction [93]. This study ignited the interest of many researchers to explore the activity of supported noble metals. For instance, Chen and co-workers investigated the photocatalytic oxidation of benzyl alcohol over $Au/TiO_2/SBA$-15 under Xe lamp, $\lambda >$ 420 nm [94]. After 4 h of reaction, 91.1% yield of benzaldehyde was obtained using $Au/TiO_2/SBA$-15, which is 3.3 times greater than that of TiO_2/SBA-15 (27.1% yield),

revealing the presence of Au could improve the photocatalytic activity remarkably. The authors concluded that Au loading is a crucial parameter that determines the efficiency of the photo-oxidation process. In another study, Tao and co-workers demonstrated that the utilization of Pd decorated on the $BiVO_4$ nanoflakes resulted in an enhanced activity for the photo-oxidation of benzyl alcohol under 300 W Xe lamp illumination for 8 h (53% conversion with 99% selectivity) compared to pure $BiVO_4$ nanoflakes (12% conversion) [87].

Interestingly, bimetallic NPs show enhanced photocatalytic performance over their monometallic counterparts due to the synergistic effects between the metals [95, 96]. The synergistic effects could arise from the efficient charge transfer and interfacial collaboration by the two metals [97]. The optical properties of bimetallic NPs depend on their morphological structure. Particularly, core-shell structure shows two different SPR peaks which stem from the two different monometallic NPs, while a single SPR peak placed between the two monometallic SPR peaks is defined for the bimetallic structure of alloy NPs.

In this direction, Li *et al.* evaluated the photocatalytic activity of Au decorated BiOCl-OV (oxygen vacancies) *via* benzyl alcohol oxidation after 8 h visible light irradiation, achieving 75.6% benzyl alcohol conversion and >99% benzaldehyde selectivity [98]. In another study, Shao *et al.* investigated the photocatalytic oxidation of benzyl alcohol in the presence of $Au/Pd/BiVO_4$ under 300 W Xenon lamp (λ= 360-780 nm) [87]. The authors reported that the incorporation of the second metal like Au resulted in a 71.8 % benzyl alcohol conversion with 99% benzaldehyde selectivity after 8 h irradiation, which is almost 1.35 times higher compared to that of monometallic $Pd/BiVO_4$ and 4.5 times higher compared to that of pure $BiVO_4$. The enhancement can be attributed to the synergistic effect between the two metals. In a collaborative study, Xu and co-workers and Liu and co-workers suggested a mechanism for the photocatalytic oxidation of benzyl alcohol in the presence of bimetallic $AuPd/TiO_2$ nanobelts [85]. The suggested mechanism, which involves three steps is similar to that of aerobic dehydrogenation (Fig. 2.12). Generally, several attempts have been made to explore the mechanism of alcohol oxidation in the presence of supported noble metals using oxygen as oxidant. Finally, different parameters such as effect of support, particle size and catalyst preparation method that affect the photocatalytic activity of plasmonic metals should be taken under consideration.

It should be noted here that different studies have used photocatalysts decorated with plasmonic NPs to drive reactions thermally. For instance, Wang et al. reported the

efficient use of photocatalysts such SiO_2, Al_2O_3, TiO_2, ZrO_2 and CeO_2 decorated with Au NPs for the dehydrogenation of benzyl alcohol to benzaldehyde, achieving conversion from 2.1 to 89 % depending on the support after 6 h reaction at 120 ºC [99]. However, compared to thermal catalysis, both photocatalysis and photothermal catalysis can offer opportunities for reducing the energy input, altering the catalytic selectivity, and increasing the reaction efficiency.
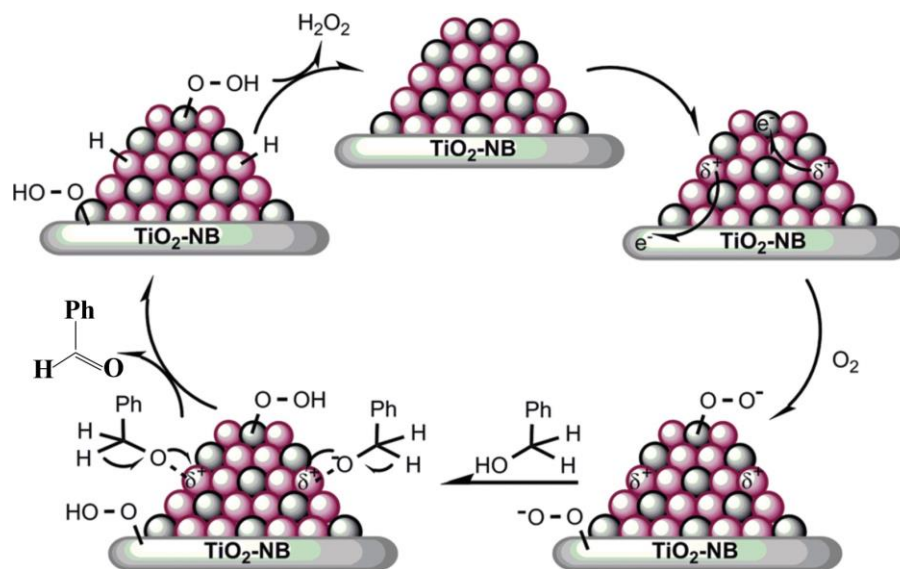

Figure 2.12. The mechanism for the aerobic oxidation of benzyl alcohol over the Au$-$Pd/TiO_2 NB nanostructures by using visible light irradiation [85].

2.5.1 Effect of support

Although free-standing plasmonic metal NPs present considerable photocatalytic activity in oxidation of alcohols under visible light irradiation, they are not considered suitable catalysts for practical applications due to the fact that they are vulnerable to aggregation and suffer from low stability [100]. Therefore, several materials including metal oxides, carbon and zeolites have been utilized as supports to stabilize metal NPs. The role of the support involves easy separation and recycling of the catalyst, control of particle growth and reduction of particles agglomeration [101-102].

Metal oxides are highly porous supports with high surface area and offer high chemical and thermal stability, properties that meet the requirements in most photocatalytic applications. They also benefit from their facile synthesis and easy separation capabilities. The most common metal oxides employed as supports are TiO_2, CeO_2, SiO_2, Al_2O_3 and Fe_2O_3. Based on their chemical reactivity, metal oxides can participate in the photocatalytic reaction rather than acting only as support for the deposition of active metals. TiO_2 decorated with plasmonic metal NPs has been widely

29

studied due to its efficient visible light activity in the photocatalytic oxidation of alcohols. For instance, Tsukamoto *et al.* assessed the photocatalytic activity of Au NPs decorated on commercial TiO_2 (P25) with visible illumination (>450 nm), achieving 79% of benzaldehyde after 4 h of reaction [103]. In another study, Tapley *et al.* used Al_2O_3 as support for Au NPs towards the selective oxidation of benzyl alcohol to benzaldehyde upon 530 nm LED irradiation [104].

Carbon materials are abundant elements that exhibit a large surface area and present high electronic conductivity [105, 106]. Carbon nanotubes and two dimensional graphene, which possess excellent electrical, optical and mechanical properties have been mainly used as supports for noble metals in heterogeneous catalysis [107-109]. Metal NPs supported on carbon materials have demonstrated efficient activity *via* the photocatalytic oxidation of alcohols. Sahoo *et al.* reported the photocatalytic superiority of AuAg nanoalloys deposited on layered double hydroxide (LDH)/ graphene oxide (GO) *via* oxidation of benzyl alcohol. Particularly, AuAg/LDH/GO presented 2.5 times higher performance (82.7% benzaldehyde yield and 90% selectivity) than LDH/GO after 3 h visible irradiation without any indication of activity loss after 5 cycles [95].

Zeolites have been utilized as supports mainly due to their crystalline nature, high thermal stability and high ability of absorption. Zeolites benefit from their large internal surface area and high porosity, characteristics that enable them as suitable supports for metal NPs [101]. Zhu *et al.* synthesized Au NPs supported on zeolites (Au@zeolites) using impregnation method and tested their catalytic activity for the oxidation of benzyl alcohol, reporting 23% benzyl alcohol conversion and 100% selectivity. The authors concluded that the use of NaOH increased remarkably the photocatalytic activity [110]. In a similar study, Ke *et al.* demonstrated the photocatalytic oxidation of benzyl alcohol to benzaldehyde driven by sunlight at ambient temperature in the presence Au/zeolites, reporting a high benzaldehyde selectivity of 99% [111].

2.5.2   Effect of particle size

The size of NPs affects remarkably the overall efficiency of the photocatalytic process. Particularly, a decrease in the size of NPs results in an increase in the surface area to volume ratio. The available surface area of NPs is of significant importance as the contact between the catalytic sites and reactant molecules increases [101]. Shape, size and morphology are characteristics that can be high controllable enabling a successful catalyst for selective oxidation of alcohols. Many studies reported that Au

NPs with small size with low loading act as more effective and selective catalysts for photocatalytic oxidation reactions compared to Au NPs with larger size [112]. For instance, Jiang *et al.* reported that the size of Au NPs affected the photocatalytic performance of benzyl alcohol oxidation in terms of benzaldehyde production (Fig. 2.13) [85]. The amount of benzaldehyde formed increased by increasing Au loading up to 3.5 wt.% Au loading on TiO_2, while decreased at higher loading due to an increased particle size, implying that large Au NPs with size > 5 nm are less active in the reaction. Size of Au NPs for Au_1/T-2, $Au_{3.5}$/T-2 and $Au_{4.5}$/T-2 were 2.8, 4.0 and 5.5 nm, respectively. In another study, Xheng *et al.* studied the influence of Au NPs size on CeO_2 nanorods for photocatalytic oxidation of propylene. They found that outgrown Au NPs (>10 nm) led to a decrease of the photocatalytic activity. The authors reported that the increase of Au NPs size resulted in saturation of exposed active sites for reactive species adsorption [113].
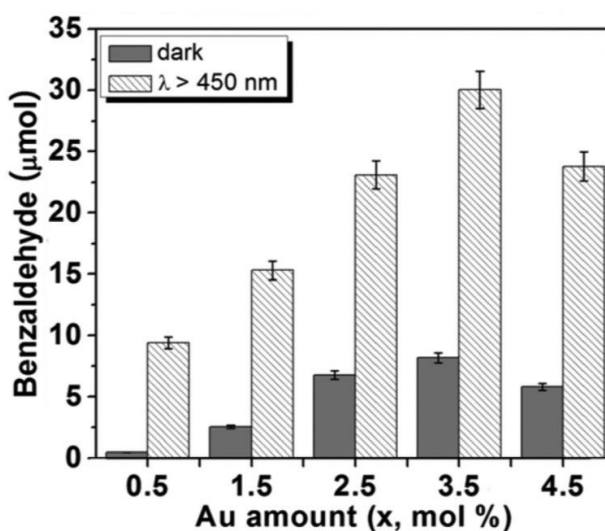
Figure 2.13. Amount of benzaldehyde formed during the benzyl alcohol oxidation in the dark (grey) and under visible light irradiation (shadow) over Au/TiO_2-NB photocatalysts with different Au loadings [113].

Similar results have been reported by many studies and it can be concluded that the activity of noble metals is directly correlated to their size, which controls the number of Au atoms and the coverage of the support surface.

2.5.3 Effect of catalyst preparation

The synthesis method of noble metals is of a strategic importance for controlling the catalyst activity and selectivity in photocatalytic oxidation of alcohols. The most common methods include chemical reduction, photodeposition, wet-impregnation and

deposition-precipitation. TEM and STEM images of Au NPs synthesized using the above methods are presented in Fig. 2.14.

Chemical reduction is one of the simplest methods to load noble metals onto the surface of metal oxides (Fig. 2.14d). Typically, this synthesis method includes the immersion of the as-synthesized support, which serves as template for the growth of metal NPs into a noble metal precursor solution. Subsequently, the metal precursor is adsorbed on the surface of the support followed by a chemical reduction using a reducing agent. The choice of the reducing agent affects remarkably the effectiveness of this synthesis method. Many reducing agents including sodium citrate and ascorbic acid have been used [114].

Another common preparation method is the photo-deposition, where light irradiation is used for the anchoring of noble metals on supports (Fig. 2.14b) [115]. In photo-deposition, electrons are excited upon light illumination from the conduction to the valence band of the semiconductor. The photoinduced electrons participate in the reduction of the adsorbed noble metal precursors into metal NPs decorated on the surface of the support. This method benefits from the fact that no addition of reducing or stabilizing agent is required, which enables the possibility to synthesize pure nanostructures free of any impurities [116]. The size of metal NPs can be controlled by altering the time and intensity of light irradiation as well as the concentration metal precursors. The desirable metal loading on the support can be achieved *via* multi-step photoreduction, repeating the addition of metal precursor and photoreduction many times.
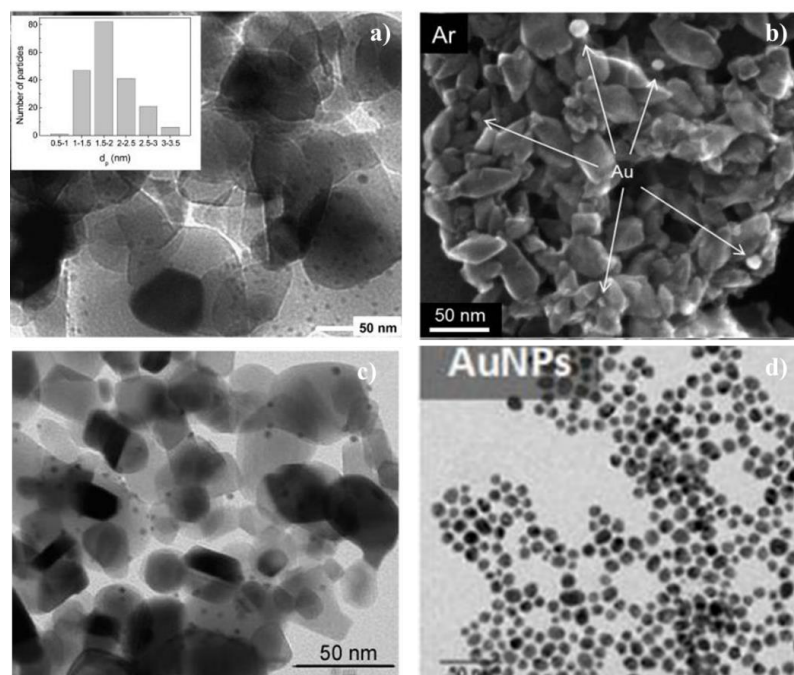
Figure 2.14. a) TEM micrographs and particle size distribution (insets) of Au/ TiO$_2$ prepared using deposition-precipitation [117], b) STEM micrographs of Au supported octahedral anatase particles prepared using photo-deposition [118], c) TEM micrographs of Au/TiO$_2$ prepared using wet impregnation [119] and d) TEM image of AuNPs prepared *via* citrate-based reduction process [120].

Wet-impregnation is a simple method for synthesizing metal NPs (Fig. 2.14c) [121]. Typically, the salt of a metal is dispersed in an aqueous solution and added onto a powdered solid support and subsequently stirred until a homogeneous solution is formed. After impregnation, the water is slowly evaporated from the powder at a desired temperature and the slurry is then dried, typically followed by calcination [122]. The rate of drying procedure influences the deposition of metal on the support. At high temperatures, the water evaporates from the solution fast without giving sufficient time to the metal to deposit on the support.

Deposition-precipitation (DP) is the most widely utilized method for the deposition of noble metals and particularly Au NPs on semiconductors (Fig. 2.14a) [123]. Typically, the as-synthesized support is dispersed into an aqueous HAuCl$_4$ precursor solution to form a slurry. The pH of the solution is adjusted to the desired value by the addition of precipitation agent [124, 125]. As precipitation agents, NaOH and urea are mainly used, with NaOH being the most common approach. The pH value of the preparation solution determines the particle size and yield deposition of metal NPs and therefore the catalytic activity. Then, the obtained slurry is washed repeatedly to remove any chloride ions left, dried and calcined in air to obtain metallic gold. This method benefits from the synthesis of small metal NPs increasing the active sites for reactants

adsorption and produces a well-defined coupling between the metal NPs and the semiconductor improving the separation of the photogenerated electrons.

Summary

   Despite the significant advances made in the photo-oxidation of benzyl alcohol by decorating metal oxides with noble metals, there are still limitations in terms of reaction rate and photonic efficiency. In this Chapter, the challenges in the photocatalytic oxidation of alcohols and the research strategies that have been employed to achieve higher benzaldehyde yield were highlighted while the research gaps of the field were identified. The existing studies have been devoted to enhancing the photocatalytic performance without efficient use of light energy resulting in long reaction time with limited yield. Additionally, since the photoreactor affects significantly the photocatalytic performance, a continuous flow reactor that makes efficient use of light irradiation will be designed and tested in the Thesis. The preparation method and the support of plasmonic metals are also crucial factors to achieve high performance and remain a subject of significant interest. The deposition-precipitation method will be used as synthesis technique in this Thesis because it favours the formation of small metal nanoparticles, which is essential in combination with laser irradiation for the effective oxidation of benzyl alcohol. At the same time, a catalyst support with absorption in UV-Vis region can act as catalytic active site, boosting the photocatalytic oxidation process. Finally, the photothermal effect of plasmonic metal nanoparticles has a key auxiliary role in the enhancement of photocatalytic performance and should be investigated during the reaction process. The literature review in this Chapter allowed to evaluate the criteria need to be considered with regards to the enhancement of photocatalytic performance. Therefore, this chapter will serve as a foundation for the following experimental and results chapters.

2.6   References

[1] S. Banerjee, D.D. Dionysiou, S.C. Pillai, Self-cleaning applications of TiO_2 by photo-induced hydrophilicity and photocatalysis, Applied Catalysis B: Environmental, 176-177 (2015) 396-428.

[2] J.W. MacFarlane, H.F. Jenkinson, T.B. Scott, Sterilization of microorganisms on jet spray formed titanium dioxide surfaces, Applied Catalysis B: Environmental, 106 (2011) 181-185.

[3] O. Ola, M.M. Maroto-Valer, Review of material design and reactor engineering on TiO_2 photocatalysis for CO2 reduction, Journal of Photochemistry and Photobiology C: Photochemistry Reviews, 24 (2015) 16-42.

[4] A. Fujishima, T.N. Rao, D.A. Tryk, Titanium dioxide photocatalysis, Journal of Photochemistry and Photobiology C: Photochemistry Reviews, 1 (2000) 1-21.

[5] W. Fan, Q. Zhang, Y. Wang, Semiconductor-based nanocomposites for photocatalytic H2 production and CO_2 conversion, Physical Chemistry Chemical Physics, 15 (2013) 2632-2649.

[6] A.B. Djurišić, Y.H. Leung, A.M. Ching Ng, Strategies for improving the efficiency of semiconductor metal oxide photocatalysis, Materials Horizons, 1 (2014) 400-410.

[7] Ohtani B., (2013), Design and Development of Active Titania and Related Photocatalysts in Photocatalysis and water purification: from fundamentals to recent applications, Wiley-VCH, Weinheim, pp. 73-102.

[8] A.L. Linsebigler, G. Lu, J.T. Yates, Photocatalysis on TiO_2 Surfaces: Principles, Mechanisms, and Selected Results, Chemical Reviews, 95 (1995) 735-758.

[9] R. Asahi, T. Morikawa, H. Irie, T. Ohwaki, Nitrogen-Doped Titanium Dioxide as Visible-Light-Sensitive Photocatalyst: Designs, Developments, and Prospects, Chemical Reviews, 114 (2014) 9824-9852.

[10] Y. Tian, T. Tatsuma, Plasmon-induced photoelectrochemistry at metal nanoparticles supported on nanoporous TiO_2, Chemical Communications, (2004) 1810-1811.

[11] A. Tanaka, S. Sakaguchi, K. Hashimoto, H. Kominami, Preparation of Au/TiO_2 with Metal Cocatalysts Exhibiting Strong Surface Plasmon Resonance Effective for Photoinduced Hydrogen Formation under Irradiation of Visible Light, ACS Catalysis, 3 (2013) 79-85.

[12] Y. Bai, N. Cherkasov, S. Huband, D. Walker, R.I. Walton, E. Rebrov, Highly Selective Continuous Flow Hydrogenation of Cinnamaldehyde to Cinnamyl Alcohol in a Pt/SiO$_2$ Coated Tube Reactor, Catalysts, 8 (2018) 58-75.

[13] X. Liu, Y. Yang, X. Shi, K. Li, Fast photocatalytic degradation of methylene blue dye using a low-power diode laser, Journal of Hazardous Materials, 283 (2015) 267-275.

[14] K. Hayat, M.A. Gondal, M.M. Khaled, S. Ahmed, Kinetic study of laser-induced photocatalytic degradation of dye (alizarin yellow) from wastewater using nanostructured ZnO, Journal of Environmental Science and Health, Part A, 45 (2010) 1413-1420.

[15] P. Christopher, H. Xin, S. Linic, Visible-light-enhanced catalytic oxidation reactions on plasmonic silver nanostructures, Nature Chemistry, 3 (2011) 467-472.

[16] S. Linic, P. Christopher, D.B. Ingram, Plasmonic-metal nanostructures for efficient conversion of solar to chemical energy, Nature Materials, 10 (2011) 911-921.

[17] M. Rycenga, C.M. Cobley, J. Zeng, W. Li, C.H. Moran, Q. Zhang, D. Qin, Y. Xia, Controlling the Synthesis and Assembly of Silver Nanostructures for Plasmonic Applications, Chemical Reviews, 111 (2011) 3669-3712.

[18] H. Cheng, K. Fuku, Y. Kuwahara, K. Mori, H. Yamashita, Harnessing single-active plasmonic nanostructures for enhanced photocatalysis under visible light, Journal of Materials Chemistry A, 3 (2015) 5244-5258.

[19] S. Peiris, J. McMurtrie, H.-Y. Zhu, Metal nanoparticle photocatalysts: emerging processes for green organic synthesis, Catalysis Science & Technology, 6 (2016) 320-338.

[20] H. Chen, L. Shao, Q. Li, J. Wang, Gold nanorods and their plasmonic properties, Chemical Society Reviews, 42 (2013) 2679-2724.

[21] H. Wang, F. Tam, N.K. Grady, N.J. Halas, Cu Nanoshells: Effects of Interband Transitions on the Nanoparticle Plasmon Resonance, The Journal of Physical Chemistry B, 109 (2005) 18218-18222.

[22] N. Zhou, V. Lopez-Puente, Q. Wang, L. Polavarapu, I. Pastoriza-Santos, Q.-H. Xu, Plasmon-enhanced light harvesting: applications in enhanced photocatalysis, photodynamic therapy and photovoltaics, RSC Advances, 5 (2015) 29076-29097.

[23] K.L. Kelly, E. Coronado, L.L. Zhao, G.C. Schatz, The Optical Properties of Metal Nanoparticles: The Influence of Size, Shape, and Dielectric Environment, The Journal of Physical Chemistry B, 107 (2003) 668-677.

[24] M.A. Mahmoud, M. Chamanzar, A. Adibi, M.A. El-Sayed, Effect of the Dielectric Constant of the Surrounding Medium and the Substrate on the Surface Plasmon Resonance Spectrum and Sensitivity Factors of Highly Symmetric Systems: Silver Nanocubes, Journal of the American Chemical Society, 134 (2012) 6434-6442.

[25] L.M. Liz-Marzán, Tailoring Surface Plasmons through the Morphology and Assembly of Metal Nanoparticles, Langmuir, 22 (2006) 32-41.

[26] C. Noguez, Surface Plasmons on Metal Nanoparticles: The Influence of Shape and Physical Environment, The Journal of Physical Chemistry C, 111 (2007) 3806-3819.

[27] M. Haruta, M. Daté, Advances in the catalysis of Au nanoparticles, Applied Catalysis A: General, 222 (2001) 427-437.

[28] X. Chen, H.-Y. Zhu, J.-C. Zhao, Z.-F. Zheng, X.-P. Gao, Visible-Light-Driven Oxidation of Organic Contaminants in Air with Gold Nanoparticle Catalysts on Oxide Supports, Angewandte Chemie International Edition, 47 (2008) 5353-5356.

[29] X. Chen, Z. Zheng, X. Ke, E. Jaatinen, T. Xie, D. Wang, C. Guo, J. Zhao, H. Zhu, Supported silver nanoparticles as photocatalysts under ultraviolet and visible light irradiation, Green Chemistry, 12 (2010) 414-419.

[30] M.R. Khan, T.W. Chuan, A. Yousuf, M.N.K. Chowdhury, C.K. Cheng, Schottky barrier and surface plasmonic resonance phenomena towards the photocatalytic reaction: study of their mechanisms to enhance photocatalytic activity, Catalysis Science & Technology, 5 (2015) 2522-2531.

[31] T. Hirakawa, P.V. Kamat, Photoinduced Electron Storage and Surface Plasmon Modulation in Ag@TiO_2 Clusters, Langmuir, 20 (2004) 5645-5647.

[32] A. Furube, L. Du, K. Hara, R. Katoh, M. Tachiya, Ultrafast Plasmon-Induced Electron Transfer from Gold Nanodots into TiO_2 Nanoparticles, Journal of the American Chemical Society, 129 (2007) 14852-14853.

[33] Y. Tian, T. Tatsuma, Mechanisms and Applications of Plasmon-Induced Charge Separation at TiO_2 Films Loaded with Gold Nanoparticles, Journal of the American Chemical Society, 127 (2005) 7632-7637.

[34] H. Wang, T. You, W. Shi, J. Li, L. Guo, Au/TiO_2/Au as a Plasmonic Coupling Photocatalyst, The Journal of Physical Chemistry C, 116 (2012) 6490-6494.

[35] Z. Zheng, B. Huang, X. Qin, X. Zhang, Y. Dai, M.-H. Whangbo, Facile in situ synthesis of visible-light plasmonic photocatalysts M@TiO_2 (M = Au, Pt, Ag) and evaluation of their photocatalytic oxidation of benzene to phenol, Journal of Materials Chemistry, 21 (2011) 9079-9087.

[36] W. Hou, Z. Liu, P. Pavaskar, W.H. Hung, S.B. Cronin, Plasmonic enhancement of photocatalytic decomposition of methyl orange under visible light, Journal of Catalysis, 277 (2011) 149-153.

[37] D.B. Ingram, P. Christopher, J.L. Bauer, S. Linic, Predictive Model for the Design of Plasmonic Metal/Semiconductor Composite Photocatalysts, ACS Catalysis, 1 (2011) 1441-1447.

[38] J.A. Dionne, H.A. Atwater, Plasmonics: Metal-worthy methods and materials in nanophotonics, MRS Bulletin, 37 (2012) 717-724.

[39] X. Zhang, Y. Zhu, X. Yang, S. Wang, J. Shen, B. Lin, C. Li, Enhanced visible light photocatalytic activity of interlayer-isolated triplex $Ag@SiO_2@TiO_2$ core–shell nanoparticles, Nanoscale, 5 (2013) 3359-3366.

[40] M.K. Kumar, S. Krishnamoorthy, L.K. Tan, S.Y. Chiam, S. Tripathy, H. Gao, Field Effects in Plasmonic Photocatalyst by Precise SiO_2 Thickness Control Using Atomic Layer Deposition, ACS Catalysis, 1 (2011) 300-308.

[41] C. Burda, X. Chen, R. Narayanan, M.A. El-Sayed, Chemistry and Properties of Nanocrystals of Different Shapes, Chemical Reviews, 105 (2005) 1025-1102.

[42] P. Christopher, D.B. Ingram, S. Linic, Enhancing Photochemical Activity of Semiconductor Nanoparticles with Optically Active Ag Nanostructures: Photochemistry Mediated by Ag Surface Plasmons, The Journal of Physical Chemistry C, 114 (2010) 9173-9177.

[43] S. Warren, E. Thimsen, Plasmonic Solar Water Splitting, Energy & Environmental Science, 5 (2012) 5133-5146.

[44] X. Wang, M. Zhu, Y. Sun, W. Fu, Q. Gu, C. Zhang, Y. Zhang, Y. Dai, Y. Sun, A New Insight of the Photothermal Effect on the Highly Efficient Visible-Light-Driven Photocatalytic Performance of Novel-Designed TiO_2 Rambutan-Like Microspheres Decorated by Au Nanorods, Particle & Particle Systems Characterization, 33 (2016) 140-149.

[45] J.B. Lee, S. Choi, J. Kim, Y.S. Nam, Plasmonically-assisted nanoarchitectures for solar water splitting: Obstacles and breakthroughs, Nano Today, 16 (2017) 61-81.

[46] P.K. Jain, X. Huang, I.H. El-Sayed, M.A. El-Sayed, Noble Metals on the Nanoscale: Optical and Photothermal Properties and Some Applications in Imaging, Sensing, Biology, and Medicine, Accounts of Chemical Research, 41 (2008) 1578-1586.

[47] L. Khosravi Khorashad, L.V. Besteiro, Z. Wang, J. Valentine, A.O. Govorov, Localization of Excess Temperature Using Plasmonic Hot Spots in Metal

Nanostructures: Combining Nano-Optical Antennas with the Fano Effect, The Journal of Physical Chemistry C, 120 (2016) 13215-13226.

[48] Y. Ren, Q. Chen, H. Qi, L. Ruan, Hot Spot Effect of Optical Nanoantenna to Enhance Localized Photothermal Conversion, ES Energy & Environment, 3 (2019) 74-79.

[49] V. Siahpoush, S. Ahmadi-kandjani, A. Nikniazi, Effect of plasmonic coupling on photothermal behavior of random nanoparticles, Optics Communications, 420 (2018) 52-58.

[50] J.-H. Kim, K.M. Twaddle, J. Hu, H. Byun, Sunlight-Induced Synthesis of Various Gold Nanoparticles and Their Heterogeneous Catalytic Properties on a Paper-Based Substrate, ACS Applied Materials & Interfaces, 6 (2014) 11514-11522.

[51] C.-W. Yen, M.A. El-Sayed, Plasmonic Field Effect on the Hexacyanoferrate (III)-Thiosulfate Electron Transfer Catalytic Reaction on Gold Nanoparticles: Electromagnetic or Thermal?, The Journal of Physical Chemistry C, 113 (2009) 19585-19590.

[52] Y. Suyama, M. Otsuki, S. Ogisu, R. Kishikawa, J. Tagami, M. Ikeda, H. Kurata, T. Cho, Effects of light sources and visible light-activated titanium dioxide photocatalyst on bleaching, Dental Materials Journal, 28 (2009) 693-699.

[53] M. Qamar, M.A. Gondal, K. Hayat, Z.H. Yamani, K. Al-Hooshani, Laser-induced removal of a dye C.I. Acid Red 87 using n-type WO_3 semiconductor catalyst, Journal of Hazardous Materials, 170 (2009) 584-589.

[54] W.-K. Jo, R.J. Tayade, New Generation Energy-Efficient Light Source for Photocatalysis: LEDs for Environmental Applications, Industrial & Engineering Chemistry Research, 53 (2014) 2073-2084.

[55] T. Jafari, E. Moharreri, A. Amin, R. Miao, W. Song, S. Suib, Photocatalytic Water Splitting-The Untamed Dream: A Review of Recent Advances, Molecules, 21 (2016) 900-928.

[56] L. Yuan, C. Han, M.-Q. Yang, Y.-J. Xu, Photocatalytic water splitting for solar hydrogen generation: fundamentals and recent advancements, International Reviews in Physical Chemistry, 35 (2016) 1-36.

[57] K. Li, X. An, K.H. Park, M. Khraisheh, J. Tang, A critical review of CO_2 photoconversion: Catalysts and reactors, Catalysis Today, 224 (2014) 3-12.

[58] M.M. Mahlambi, C.J. Ngila, B.B. Mamba, Recent Developments in Environmental Photocatalytic Degradation of Organic Pollutants: The Case of Titanium Dioxide Nanoparticles - A Review, Journal of Nanomaterials, 2 (2015) 29-57.

[59] J. Huang, M. Zhang, J. Wang, X. Hu, R. Luque, F.L.Y. Lam, A comprehensive study on the effect of preparation methods for Au-core@shell silica materials in room temperature oxidative amide formation, Journal of Materials Chemistry A, 3 (2015) 789-796.

[60] E.Y. Lukianova-Hleb, A. Belyanin, S. Kashinath, X. Wu, D.O. Lapotko, Plasmonic nanobubble-enhanced endosomal escape processes for selective and guided intracellular delivery of chemotherapy to drug-resistant cancer cells, Biomaterials, 33 (2012) 1821-1826.

[61] D.S. Bhatkhande, S.P. Kamble, S.B. Sawant, V.G. Pangarkar, Photocatalytic and photochemical degradation of nitrobenzene using artificial ultraviolet light, Chemical Engineering Journal, 102 (2004) 283-290.

[62] M.A. Gondal, M.N. Sayeed, A. Alarfaj, Activity comparison of Fe2O3, NiO, WO3, TiO2 semiconductor catalysts in phenol degradation by laser enhanced photo-catalytic process, Chemical Physics Letters, 445 (2007) 325-330.

[63] M.A. Gondal, M.A. Ali, X.F. Chang, K. Shen, Q.Y. Xu, Z.H. Yamani, Pulsed laser-induced photocatalytic reduction of greenhouse gas CO_2 into methanol: A value-added hydrocarbon product over SiC, Journal of Environmental Science and Health, Part A, 47 (2012) 1571-1576.

[64] M.A. Gondal, M.A. Ali, M.A. Dastageer, X. Chang, CO_2 Conversion into Methanol Using Granular Silicon Carbide (α6H-SiC): A Comparative Evaluation of 355 nm Laser and Xenon Mercury Broad Band Radiation Sources, Catalysis Letters, 143 (2013) 108-117.

[65] Tokode O., Lawton L., Robertson P., (2014), UV LED Sources for Heterogeneous Photocatalysis, in Environmental Photochemistry Part III, Springer Verlag, pp. 159-179

[66] Johnson B., (2003), High-power, short-wave LED purifies air, in Photonics spectra, Laurin Publishing Co., Inc. Pittsfield, p. 111.

[67] Svelto O, (1998), Principles of Lasers, Springer, New York Dordrecht Heidelberg London, pp. 1-607.

[68] Csele M. (2004), Fundamentals of light sources and lasers, A John Wiley & Sons, Inc., pp. 1-336.

[69] L.H. Levine, J.T. Richards, J.L. Coutts, R. Soler, F. Maxik, R.M. Wheeler, Feasibility of Ultraviolet-Light-Emitting Diodes as an Alternative Light Source for Photocatalysis, Journal of the Air & Waste Management Association, 61 (2011) 932-940.

[70] N. Zhou, V. López-Puente, Q. Wang, L. Polavarapu, I. Pastoriza-Santos, Q.-H. Xu, Plasmon-enhanced light harvesting: applications in enhanced photocatalysis, photodynamic therapy and photovoltaics, RSC Advances, 5 (2015) 29076-29097.

[71] S. Hashimoto, D. Werner, T. Uwada, Studies on the interaction of pulsed lasers with plasmonic gold nanoparticles toward light manipulation, heat management, and nanofabrication, Journal of Photochemistry and Photobiology C: Photochemistry Reviews, 13 (2012) 28-54.

[72] J. A. Lloyd, S. H. Ng, A. C. Y. Liu, Y. Zhu, W. Chao, T. Coenen, J. Etheridge, D. E. Gómez, U. Bach Plasmonic Nanolenses: Electrostatic Self-Assembly of Hierarchical Nanoparticle Trimers and Their Response to Optical and Electron Beam Stimuli, ACS Nano (2017), 11, 2, 1604–1612

[73] S.-S. Chang, C.-W. Shih, C.-D. Chen, W.-C. Lai, C.R.C. Wang, The Shape Transition of Gold Nanorods, Langmuir, 15 (1999) 701-709.

[74] F. Caupin, E. Herbert, Cavitation in water: a review, Comptes Rendus Physique, 7 (2006) 1000-1017.

[75] A. Takami, H. Kurita, S. Koda, Laser-Induced Size Reduction of Noble Metal Particles, The Journal of Physical Chemistry B, 103 (1999) 1226-1232.

[76] X. Li, A. Pyatenko, Y. Shimizu, H. Wang, K. Koga, N. Koshizaki, Fabrication of Crystalline Silicon Spheres by Selective Laser Heating in Liquid Medium, Langmuir, 27 (2011) 5076-5080.

[77] C.-H. Lin, L. Jiang, J. Zhou, H. Xiao, S.-J. Chen, H.-L. Tsai, Laser-treated substrate with nanoparticles for surface-enhanced Raman scattering, Optics Letters, 35 (2010) 941-943.

[78] X. Chang, J. Zheng, M.A. Gondal, G. Ji, Photocatalytic conversion of CO_2 into value-added hydrocarbon (methanol) with high selectivity over ZnS nanoparticles driven by 355-nm pulsed laser, Research on Chemical Intermediates, 41 (2015) 739-747.

[79] A. Pineda, L. Gomez, A.M. Balu, V. Sebastian, M. Ojeda, M. Arruebo, A.A. Romero, J. Santamaria, R. Luque, Laser-driven heterogeneous catalysis: efficient amide formation catalysed by Au/SiO2 systems, Green Chemistry, 15 (2013) 2043-2049.

[80] M.A. Gondal, M.N. Sayeed, Laser-enhanced photocatalytic degradation of organic pollutants from water using ZnO semiconductor catalyst, Journal of Environmental Science and Health, Part A, 43 (2007) 70-77.

[81] M.A. Gondal, M.N. Sayeed, Z. Seddigi, Laser enhanced photo-catalytic removal of phenol from water using p-type NiO semiconductor catalyst, Journal of Hazardous Materials, 155 (2008) 83-89.

[82] C.J.B. Alejo, C. Fasciani, M. Grenier, J.C. Netto-Ferreira, J.C. Scaiano, Reduction of resazurin to resorufin catalyzed by gold nanoparticles: dramatic reaction acceleration by laser or LED plasmon excitation, Catalysis Science & Technology, 1 (2011) 1506-1511.

[83] W.H. Hung, M. Aykol, D. Valley, W. Hou, S.B. Cronin, Plasmon Resonant Enhancement of Carbon Monoxide Catalysis, Nano Letters, 10 (2010) 1314-1318.

[84] S.A. Trammell, R. Nita, M. Moore, D. Zabetakis, E. Chang, D.A. Knight, Accelerating the initial rate of hydrolysis of methyl parathion with laser excitation using monolayer protected 10 nm Au nanoparticles capped with a Cu(bpy) catalyst, Chemical Communications, 48 (2012) 4121-4123.

[85] T. Jiang, C. Jia, L. Zhang, S. He, Y. Sang, H. Li, Y. Li, X. Xu, H. Liu, Gold and gold–palladium alloy nanoparticles on heterostructured TiO_2 nanobelts as plasmonic photocatalysts for benzyl alcohol oxidation, Nanoscale, 7 (2015) 209-217.

[86] N. Gogoi, G. Borah, P.K. Gogoi, T.R. Chetia, TiO_2 supported gold nanoparticles: An efficient photocatalyst for oxidation of alcohol to aldehyde and ketone in presence of visible light irradiation, Chemical Physics Letters, 692 (2018) 224-231.

[87] X. Tao, L. Shao, R. Wang, H. Xiang, B. Li, Synthesis of BiVO4 nanoflakes decorated with AuPd nanoparticles as selective oxidation photocatalysts, Journal of Colloid and Interface Science, 541 (2019) 300-311.

[88] D. Motta, F.J.S. Trujillo, N. Dimitratos, A. Villa, L. Prati, An investigation on AuPt and AuPt-Bi on granular carbon as catalysts for the oxidation of glycerol under continuous flow conditions, Catalysis Today, 308 (2018) 50-57.

[89] A. Singh, A. Baruah, V. Katoch, K. Vaghasiya, B. Prakash, A.K. Ganguli, Continuous flow synthesis of Ag_3PO_4 nanoparticles with greater photostability and photocatalytic dye degradation efficiency, Journal of Photochemistry and Photobiology A: Chemistry, 364 (2018) 382-389.

[90] Rossetti I., (2016) Flow Chemistry: New Concepts from Batch to Continuous Organic Chemistry, Industrial Chemistry, pp.1-2.

[91] V. Hessel, D. Kralisch, N. Kockmann, T. Noël, Q. Wang, Novel Process Windows for Enabling, Accelerating, and Uplifting Flow Chemistry, ChemSusChem, 6 (2013) 746-789.

[92] X. Zhang, X. Ke, J. Yao, Recent development of plasmon-mediated photocatalysts and their potential in selectivity regulation, Journal of Materials Chemistry A, 6 (2018) 1941-1966.

[93] A. Tanaka, K. Hashimoto, H. Kominami, Preparation of Au/CeO2 Exhibiting Strong Surface Plasmon Resonance Effective for Selective or Chemoselective Oxidation of Alcohols to Aldehydes or Ketones in Aqueous Suspensions under Irradiation by Green Light, Journal of the American Chemical Society, 134 (2012) 14526-14533.

[94] Y. Chen, W. Li, J. Wang, Q. Yang, Q. Hou, M. Ju, Gold nanoparticle-modified TiO$_2$/SBA-15 nanocomposites as active plasmonic photocatalysts for the selective oxidation of aromatic alcohols, RSC Advances, 6 (2016) 70352-70363.

[95] M. Sahoo, S. Mansingh, K.M. Parida, A bimetallic Au–Ag nanoalloy mounted LDH/RGO nanocomposite: a promising catalyst effective towards a coupled system for the photoredox reactions converting benzyl alcohol to benzaldehyde and nitrobenzene to aniline under visible light, Journal of Materials Chemistry A, 7 (2019) 7614-7627.

[96] Y.-J. Song, Y.M. López-De Jesús, P.T. Fanson, C.T. Williams, Preparation and Characterization of Dendrimer-Derived Bimetallic Ir–Au/Al$_2$O$_3$ Catalysts for CO Oxidation, The Journal of Physical Chemistry C, 117 (2013) 10999-11007.

[97] R. Nazir, P. Fageria, M. Basu, S. Pande, Decoration of Carbon Nitride Surface with Bimetallic Nanoparticles (Ag/Pt, Ag/Pd, and Ag/Au) *via* Galvanic Exchange for Hydrogen Evolution Reaction, The Journal of Physical Chemistry C, 121 (2017) 19548-19558.

[98] H. Li, F. Qin, Z. Yang, X. Cui, J. Wang, L. Zhang, New Reaction Pathway Induced by Plasmon for Selective Benzyl Alcohol Oxidation on BiOCl Possessing Oxygen Vacancies, Journal of the American Chemical Society, 139 (2017) 3513-3521.

[99] W. Fang, J. Chen, Q. Zhang, W. Deng, Y. Wang, Hydrotalcite-Supported Gold Catalyst for the Oxidant-Free Dehydrogenation of Benzyl Alcohol: Studies on Support and Gold Size Effects, Chemistry – A European Journal, 17 (2011) 1247-1256

[100] G.L. Hallett-Tapley, M.J. Silvero, M. González-Béjar, M. Grenier, J.C. Netto-Ferreira, J.C. Scaiano, Plasmon-Mediated Catalytic Oxidation of sec-Phenethyl and Benzyl Alcohols, The Journal of Physical Chemistry C, 115 (2011) 10784-10790.

[101] A.S. Sharma, H. Kaur, D. Shah, Selective oxidation of alcohols by supported gold nanoparticles: recent advances, RSC Advances, 6 (2016) 28688-28727.

[102] X. Pan, X. Bao, Reactions over catalysts confined in carbon nanotubes, Chemical Communications, (2008) 6271-6281.

[103] D. Tsukamoto, Y. Shiraishi, Y. Sugano, S. Ichikawa, S. Tanaka, T. Hirai, Gold Nanoparticles Located at the Interface of Anatase/Rutile TiO_2 Particles as Active Plasmonic Photocatalysts for Aerobic Oxidation, Journal of the American Chemical Society, 134 (2012) 6309-6315.

[104] G.L. Hallett-Tapley, M.J. Silvero, C.J. Bueno-Alejo, M. González-Béjar, C.D. McTiernan, M. Grenier, J.C. Netto-Ferreira, J.C. Scaiano, Supported Gold Nanoparticles as Efficient Catalysts in the Solventless Plasmon Mediated Oxidation of sec-Phenethyl and Benzyl Alcohol, The Journal of Physical Chemistry C, 117 (2013) 12279-12288.

[105] T. Wu, S. Liu, Y. Luo, W. Lu, L. Wang, X. Sun, Surface plasmon resonance-induced visible light photocatalytic reduction of graphene oxide: Using Ag nanoparticles as a plasmonic photocatalyst, Nanoscale, 3 (2011) 2142-2144.

[106] J. Li, C.-y. Liu, Z. Xie, Synthesis and surface plasmon resonance properties of carbon-coated Cu and Co nanoparticles, Materials Research Bulletin, 46 (2011) 743-747.

[107] G.G. Wildgoose, C.E. Banks, R.G. Compton, Metal Nanoparticles and Related Materials Supported on Carbon Nanotubes: Methods and Applications, Small, 2 (2006) 182-193.

[108] C. Wang, S. Guo, X. Pan, W. Chen, X. Bao, Tailored cutting of carbon nanotubes and controlled dispersion of metal nanoparticles inside their channels, Journal of Materials Chemistry, 18 (2008) 5782-5786.

[109] M.-M. Titirici, R.J. White, N. Brun, V.L. Budarin, D.S. Su, F. del Monte, J.H. Clark, M.J. MacLachlan, Sustainable carbon materials, Chemical Society Reviews, 44 (2015) 250-290.

[110] H. Zhu, X. Chen, Z. Zheng, X. Ke, E. Jaatinen, J. Zhao, C. Guo, T. Xie, D. Wang, Mechanism of supported gold nanoparticles as photocatalysts under ultraviolet and visible light irradiation, Chemical Communications, (2009) 7524-7526.

[111] X. Zhang, X. Ke, H. Zhu, Zeolite-Supported Gold Nanoparticles for Selective Photo-oxidation of Aromatic Alcohols under Visible-Light Irradiation, Chemistry – A European Journal, 18 (2012) 8048-8056.

[112] T. Ishida, M. Haruta, Gold Catalysts: Towards Sustainable Chemistry, Angewandte Chemie International Edition, 46 (2007) 7154-7156.

[113] D. Jiang, W. Wang, S. Sun, L. Zhang and Y. Zheng, Equilibrating the Plasmonic and Catalytic Roles of Metallic Nanostructures in Photocatalytic Oxidation over Au-Modified CeO_2, ACS Catal., (2015), 5, 613–621.

[114] J. Kimling, M. Maier, B. Okenve, V. Kotaidis, H. Ballot, A. Plech, Turkevich Method for Gold Nanoparticle Synthesis Revisited, The Journal of Physical Chemistry B, 110 (2006) 15700-15707.

[115] C. Tossi, L. Hällström, J. Selin, M. Vaelma, E. See, J. Lahtinen, I. Tittonen, Size- and density-controlled photodeposition of metallic platinum nanoparticles on titanium dioxide for photocatalytic applications, Journal of Materials Chemistry A, 7 (2019) 14519-14525.

[116] B. Kraeutler, A.J. Bard, Heterogeneous photocatalytic preparation of supported catalysts. Photodeposition of platinum on titanium dioxide powder and other substrates, Journal of the American Chemical Society, 100 (1978) 4317-4318.

[117] C. Gomes Silva, R. Juárez, T. Marino, R. Molinari, H. García, Influence of Excitation Wavelength (UV or Visible Light) on the Photocatalytic Activity of Titania Containing Gold Nanoparticles for the Generation of Hydrogen or Oxygen from Water, Journal of the American Chemical Society, 133 (2011) 595-602.

[118] Z. Wei, L. Rosa, K. Wang, M. Endo, S. Juodkazis, B. Ohtani, E. Kowalska, Size- controlled gold nanoparticles on octahedral anatase particles as efficient plasmonic photocatalyst, Applied Catalysis B: Environmental, 206 (2017) 393-405.

[119] L. Delannoy, N. El Hassan, A. Musi, N.N. Le To, J.-M. Krafft, C. Louis, Preparation of Supported Gold Nanoparticles by a Modified Incipient Wetness Impregnation Method, The Journal of Physical Chemistry B, 110 (2006) 22471-22478.

[120] H. Tyagi, A. Kushwaha, A. Kumar, M. Aslam, A Facile pH Controlled Citrate- Based Reduction Method for Gold Nanoparticle Synthesis at Room Temperature, Nanoscale Research Letters, 11 (2016) 362-472.

[121] P. Munnik, P.E. de Jongh, K.P. de Jong, Recent Developments in the Synthesis of Supported Catalysts, Chemical Reviews, 115 (2015) 6687-6718.

[122] Y. Xu, Q. Lin, B. Liu, F. Jiang, Y. Xu, X. Liu, A Facile Fabrication of Supported Ni/SiO2 Catalysts for Dry Reforming of Methane with Remarkably Enhanced Catalytic Performance, Catalysts, 9 (2019) 183-191.

[123] M. Haruta, Gold as a novel catalyst in the 21st century: Preparation, working mechanism and applications, Gold Bulletin, 37 (2004) 27-36.

[124] F. Moreau, G.C. Bond, Gold on titania catalysts, influence of some physicochemical parameters on the activity and stability for the oxidation of carbon monoxide, Applied Catalysis A: General, 302 (2006) 110-117.

[125] F. Moreau, G.C. Bond, A.O. Taylor, Gold on titania catalysts for the oxidation of carbon monoxide: control of pH during preparation with various gold contents, Journal of Catalysis, 231 (2005) 105-114.

Chapter 3 – Experimental Methodology

In Chapter 2, a review of the fundamentals and properties of plasmonic metal NPs as well as their photocatalytic activity allowed to evaluate the methodology that will be used in photocatalytic oxidation advancements. For nanomaterials, characteristics such as particle size, morphology and surface composition are of key importance. Evaluation of physicochemical properties such as content, absorption and crystallinity is vital to understand the parameters which affect the catalytic performance and explore possible routes for optimization. The experimental design of this Chapter includes materials synthesis techniques, physicochemical and photo-electrochemical characterization, design and setup of continuous flow system, conditions of plasmonic heating experiment and benzyl alcohol photo-oxidation and finally product identification and analysis. The fundamental theories of physicochemical and electrochemical characterization techniques are presented.

3.1 Materials synthesis

3.1.1 Materials

Potassium dichromate ($K_2Cr_2O_7$, 99.99%), acrylamide solution ($CH_2CHCONH_2$, 40% in H_2O), gold (III) chloride trihydrate ($HAuCl_4 \cdot 3H_2O \geq 99.9$ % trace metals basis) and P25 Titanium (IV) oxide (particle size 21 nm, $\geq 99.5\%$ trace metals basis) nanopowders were supplied from Sigma Aldrich. Ethanol (≥ 99.8 %) and sodium hydroxide (Pellets, $\geq 98.5\%$) were obtained from Fischer Scientific and Acros Organics, respectively. All chemicals were utilized as received. All aqueous solutions were prepared utilizing Milli–Q water type I with resistivity 18.2 MΩ·cm.

3.1.2 Synthesis of Cr_2O_3 microspheres

Cr_2O_3 microspheres, as shown in Fig. 3.1a, were synthesized using a hydrothermal approach [1]. Firstly, $K_2Cr_2O_7$ (0.05 mmol) was dissolved into milli-Q water (456 mL). Then, 1.0 mmol acrylamide were added and stirred for 30 min until a homogeneous solution, orange in colour, was formed. The prepared solution was transferred into the Teflon–lined autoclave (100 mL) for hydrothermal treatment at 180 °C for 12 h. Upon cooling down to room temperature, the green coloured powder was collected and sequentially washed with water and then ethanol three times each. The powder was then

dried in an oven at 75 °C overnight. To improve the crystallization of the obtained powder, the dried Cr_2O_3 was calcined under air at 900 °C for 1 h.

3.1.3   Synthesis of Au/TiO₂ nanoparticles and Au/Cr₂O₃ microspheres

Monometallic Au nanoparticles (1, 3 & 5 wt.%) were decorated on TiO_2 nanoparticles and Cr_2O_3 microspheres using deposition-precipitation (DP) method with NaOH (Fig. 3.1b) [2]. Commercial Degussa P25-TiO_2 and Cr_2O_3 powder were dried in an oven for 24 h before use. Different concentrations of $AuCl_4 \cdot 3H_2O$ (1, 3 & 5 wt.% Au) were dissolved in 25 mL milli-Q water and the pH of the solution was controlled at 9 by adding a certain amount of NaOH. Then, 150mg of commercial P25-TiO_2 or synthesized Cr_2O_3 powder were added to the solution and the pH was re-adjusted at 9. DP was performed at 80 °C under 2 hrs vigorous stirring keeping the pH constant at 9 and then the solution was stirred overnight. After the DP procedure, the obtained powders were collected by centrifuge, rinsed thoroughly with ethanol and milli-Q water and air-dried at 80 °C overnight. Finally, Au/TiO_2 and Au/Cr_2O_3 powders were calcined under air atmosphere at 300 °C for 4 h with a ramp rate of 5 °C/min. For photocatalytic experiments, 2 & 4 wt.% Au loadings on Cr_2O_3 microspheres were prepared and tested as well (Fig. A1-2, APPENDIX A) while 1, 3 & 5 wt.% Au loadings were discussed in detail in Chapter 5 showing a specific trend.

3.1.4   Synthesis of Ag-Au/TiO₂ nanoparticles and Ag-Au/Cr₂O₃ microspheres

Monometallic Ag nanoparticles were decorated on Cr_2O_3 microspheres using wet impregnation method [3]. Different concentrations of $AgNO_3$ (with loadings 0.5 – 2 wt.%) were dispersed in an aqueous solution (10 mL) in a round bottom flask. Then, the obtained solution was added onto 150 mg of Cr_2O_3 powder and stirred until a homogeneous solution was formed. After impregnation, the water was slowly evaporated from the powder at 60 °C (60 rpm) using a rotary evaporator. The produced Ag/Cr_2O_3 powders were collected by centrifugation and washed thoroughly with ethanol and water. The as-synthesized samples were dried in an oven at 75 °C overnight and calcined at 400 °C for 4 h with a ramping rate of 5 °C/min. Monometallic 1 wt.% Ag/P25-TiO_2 nanoparticles were synthesized as a reference for comparison with Cr_2O_3 supported Ag NPs.

For synthesis of bimetallic NPs, Au loading was kept constant at 3 wt.% based on the highest obtained photocatalytic activity as demonstrated in Chapter 5, while Ag loading

was varied between 0.5-3 wt.% to investigate the effect of Ag-Au ratio. Bimetallic Ag-Au/Cr_2O_3 photocatalysts were synthesized as follows: Initially, 3 wt.% Au/Cr_2O_3 photocatalysts were prepared by deposition precipitation method and then Ag-Au/Cr_2O_3 samples were loaded *via* wet impregnation deposition of Ag NPs on 3 wt.% Au/Cr_2O_3 support (Fig. 3.1c). The obtained bimetallic photocatalysts Ag (0.5 wt.%) – Au (3 wt.%)/Cr_2O_3, Ag (1 wt.%) - Au (3 wt.%)/Cr_2O_3, Ag (2 wt.%) – Au (3 wt.%)/Cr_2O_3 and Ag (3 wt.%) – Au (3 wt.%)/Cr_2O_3 (where wt.% represents the weight percentage of metal) were designated as 0.5Ag-3Au/Cr_2O_3, 1Ag-3Au/Cr_2O_3, 2Ag-3Au/Cr_2O_3 and 3Ag-3Au/Cr_2O_3, respectively. Bimetallic Ag (0.5 wt.%)-Au (3 wt.%)/TiO_2 were synthesized as a reference for comparison with Cr_2O_3 supported Ag-Au NPs.
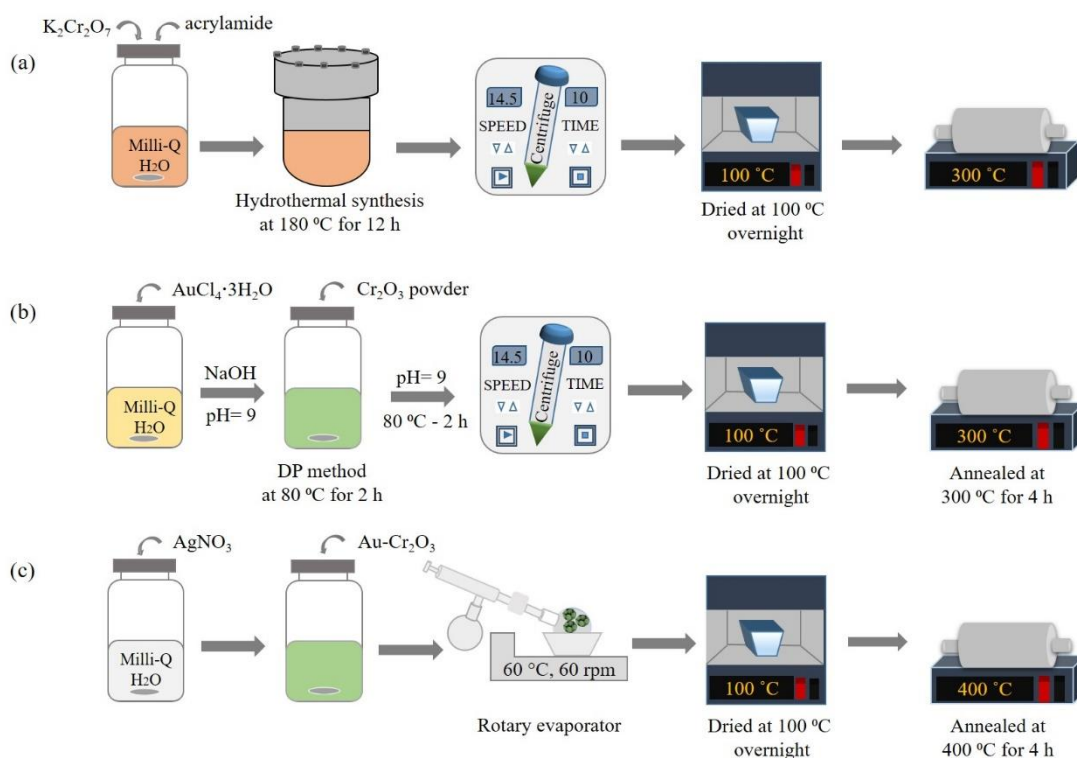
Figure 3.1. Schematic illustration of a) hydrothermal synthesis of Cr_2O_3 microspheres, b) DP method of Au nanoparticles loaded on Cr_2O_3 microspheres and c) wet impregnation method of Ag nanoparticles loaded on Au/Cr_2O_3 microspheres.

3.2 Physicochemical characterization techniques

3.2.1 Scanning electron microscopy (SEM)

3.2.1.1 Background

Scanning electron microscopy (SEM) is an imaging technique which investigates the morphology of the samples. In this microscopic technique, the surface of the sample is scanned with a high-energy electron beam to produce an image. Particularly, electrons are produced by an electron source at the top of the column, accelerated down and travelled through a set of lenses and apertures in the vacuum chamber to generate a focused beam of electrons which eventually strikes the surface of the sample. When the electron beam interacts with the sample, many signals like secondary and backscattered electrons are produced [4]. Subsequently, these signals are collected from a detector to form images that can be displayed on a computer monitor.

3.2.1.2 Experimental

The morphology of the samples was examined using a Focused Ion Beam (FIB) Emission Scanning Electron Microscope (SEM, FEI Quanta 3D FEG) operated at an accelerated voltage of 10 kV. Samples were prepared by dispersing 1 mg of nanopowder in 400 μL ethanol and the solution was sonicated for 5 minutes. Subsequently, a drop of the suspension was deposited on a silicon wafer and allowed to dry before placed on the SEM specimen.

3.2.2 Transmission electron microscopy (TEM)

3.2.2.1 Background

Transmission electron microscopy (TEM) is an imaging technique which operates in a similar way to that of light microscope using electrons instead of light. Similar to SEM, high-energy electrons travel through a sequence of lenses under vacuum to produce the desired focused beam of electrons which hit the surface of the sample [5]. The interaction of the electrons with the sample generates X-Rays that is recorded on high-resolution fluorescent screen acquiring information about morphology, crystallization and composition of the tested material. A TEM sample should be thin enough to allow sufficient electrons to pass through in order to obtain an image with minimum loss energy. Therefore, sample preparation is of significant importance for TEM analysis.

3.2.2.2   Experimental

TEM was performed using a high-resolution transmission electron microscope (HR-TEM FEI Titan Themis 200) equipped with an energy dispersive X-Ray (EDX) detector operated at 200 kV for identification of chemical composition. Crystallographic nature of the samples was identified using Selected Area Electron Diffraction (SAED) technique in the transmission electron microscope.   Samples were prepared by dispersing 1 mg of nanopowder in 400 μL ethanol and depositing a drop of the suspension on a carbon coated Cu grid.

3.2.3   Energy Dispersive X-Ray Analysis (EDX)

Energy dispersive X-Ray spectroscopy (EDX) is an analytical technique coupled with SEM or TEM for identification of elemental composition of the nanomaterials. Electrons beam hits the surface of the sample causing excitation of the atoms in discrete orbitals. When the electrons vacancies are filled by higher-state electrons, X-Rays are emitted which have characteristic energy for each element. The identification and quantification of the elemental composition of the sample can be done by measuring the peak energy of the emitted X-Rays.

3.2.4   X-Ray diffraction spectroscopy (XRD)

3.2.4.1   Background

X-Ray diffraction (XRD) is a technique which is used to identify the crystal structure, crystallite size and lattice parameters of nanomaterials [6]. XRD is based on diffraction of X-Ray beams as a function of the angle of the incident beam. These X-Rays are produced from targeted metal, which is bombarded by high energy electrons (usually Cu or Mo), and then are filtered and concentrated into monochromatic radiation which is directed towards the sample. The interaction of X-Ray beam with the surface of the sample generates reflected rays from constructive interference when conditions of Bragg's law are satisfied:

$$2d \sin \theta = n\lambda \qquad\qquad (3.1)$$

where d represents the planar spacing, θ is the angle between incident and normal to the lattice plane, n is the order of reflection and λ corresponds to X-Ray wavelength.

Additionally, from the diffraction data, the crystallite size of the material can be estimated using Scherrer's equation:

$$L = \frac{k\lambda}{B\cos\theta} \qquad (3.2)$$

where k is a dimensionless shape factor, λ is X-Ray wavelength, B is full width of half maximum of the peak and θ is the angle.

3.2.4.2   Experimental

XRD measurements were carried out using a D8 Advance (Bruker AXS) X-Ray diffractometer with Cu Ka radiation (λ=1.5418 Å) and a nickel beta filter ($2\theta = 10\text{-}80°$). Powder samples were mounted onto sample holder and placed into the equipment.

3.2.5   Raman spectroscopy

3.2.5.1   Background

Raman spectroscopy is a technique utilized to provide information about vibrational, rotational and other low-frequency modes of molecules [7]. Raman spectroscopy is based on inelastic scattering of photons from a laser light source. In this scattering process, incident photons interact with the sample resulting in a change of the frequency of the photons towards red or blue. The shift in energy gives information about vibrational modes of molecules. Typically, scattered light is collected with lens and passes through a monochromator to acquire Raman spectrum. A Raman spectrum consists of a number of peaks featuring wavelength position and intensity of scattered light. Each peak corresponds to characteristic chemical fingerprint that can be used to distinguish a material from others.

3.2.5.2   Experimental

Raman spectroscopy measurements were conducted on a Renishaw microscope equipped with 785 nm as source of exciting light. Powder samples were loaded onto a microscope glass and spread to obtain a thin layer. Prior to measurements, silicon wafer was used for background correction.

3.2.6 Diffuse reflectance spectroscopy

3.2.6.1 Background

The optical properties of nanostructures such as absorption coefficient, absorption and reflectance spectra and energy bandgap can be investigated using UV-Vis spectroscopy [8]. The electromagnetic radiation employed in UV-Vis spectroscopy is in the range of ultraviolet (185-400 nm) to visible (400–800 nm). The basic principle of a spectrophotometer is based on Beer-Lambert law. As described by the Beer-Lambert law, the absorbance of a sample is directly proportional to its thickness (optical path).

$$A = \varepsilon \cdot c \cdot l \tag{3.3}$$

Transmittance of a sample can be defined as:

$$T = \frac{I}{I_o} \tag{3.4}$$

where I, and I_o represent the intensities of transmitted and incident light, respectively.

For measurement of solid samples, a spectrophotometer with an integrated sphere is used. Integrating sphere is an optical arrangement consisting of a cavity whose inner surface is homogeneously coated with highly reflective material such as barium sulfate. Integrating spheres have small holes (aperture) that act as inlet and outlet ports so that radiation passes through the sample, enters the sphere and then is collected by the detector.

3.2.6.2 Experimental

UV-Vis Diffuse reflectance spectra (DRS) of the prepared samples were collected using a Perkin Elmer Lamda 950 spectrophotometer equipped with a 150 mm integrating sphere using $BaSO_4$ for background correction. Powder samples were loaded onto a quartz cell sample holder which was placed inside the spectrophotometer. The band gap energy was calculated using Kubelka-Muck function:

$$F(R) = \frac{(1-R)^2}{2R} \tag{3.5}$$

in which R is the reflectance.

3.3 Photoelectrochemical performance measurements

3.3.1.1 Background

Chronoamperometry is a well-established electrochemical characterization technique which can provide information about catalyst stability and reaction kinetics. In chronoamperometry measurements, a fixed potential is applied to the working electrode, while current density response, resulting from faradaic processes occurring at the electrode, is recorded as a function of time [9]. Changes in the current density are related to a rise or decrease in the diffusion layers of the analyte at the surface of the working electrode. Generally, a stable photocurrent density reveals the stability of photoelectrodes while a photocurrent density drop is observed in case of unstable photoelectrodes. Additionally, chronoamperometric techniques enable the identification of any corrosion and degradation of the photocatalyst.

3.3.1.2 Experimental

Photoelectrochemical measurements (Chronoamperometry) of all catalysts were carried out in a three-electrode home-made cell [10], consisting of a sample-coated electrode as working electrode with an active area of 1 cm^2, Pt wire as counter electrode and Ag/AgCl (KCl 1M) as reference electrode while 0.5 M Na_2SO_4 aqueous solution served as electrolyte. The working electrode was prepared by electrophoresis deposition, as follows: 16 mg/mL of Au/Cr_2O_3 powder were dispersed in 250 mL acetonitrile solution containing 4 mg/mL iodine (making the particles positively charged). For the electrophoresis procedure, a Fluorine doped Tin Oxide (FTO) glass (sample-coated electrode) and an auxiliary FTO glass were placed in parallel (1 cm distance) and 10 V was applied between the two electrodes for 60 sec to obtain a uniform layer of Au/Cr_2O_3 deposited on FTO glass. The bottom part of the FTO glasses were immersed into the suspension (1 cm x 1 cm). All the prepared electrodes (3 x coated electrodes per sample) were measured and found to have a similar coating film after electrophoresis deposition. Then, the prepared films were dried in air and calcined at 300 °C for 1 h. Chronoamperometry experiments were performed using an Autolab PGSTAT 302N electrochemical workstation in the presence of a solar simulator (Newport 92250A, AM 1.5G, 100 mW·cm^{-2}), illuminating the electrodes with an active area of 1 cm^2 (optical window of the reactor).

3.4 Reactor design

Initially, polymethyl methacrylate (PMMA) sheets were cut and engraved in different dimensions using Trotec Speedy laser cutter/engraver. The fabrication of these parts allowed the most effective use of the laser cutting and engraving process and therefore optimization of reactor design parameters. In order to ensure maximization of the illuminated surface area of dispersed plasmonic NPs in the water or toluene based solutions, the dimensions of the cell were minimized to the desired values. In this direction, the flow cell has been designed in such a way that the nanofluid is irradiated for the longest possible period of time. A longer irradiation time of NPs increases the duration of LSPR effect of each nanoparticle resulting in enhanced photothermal/photocatalytic process. The fluids were irradiated with laser light traveling in and against flow direction showing similar results in the temperature change. However, when high concentration of NPs was used, irradiation in the direction of flow affected negatively the uniform flow of Au/TiO_2 and Au/Cr_2O_3 fluids due to precipitation.

3.4.1 Fabrication of continuous flow container for laser induced plasmonic heating experiment

A Trotec Speedy 300 laser cutter/engraver was used to fabricate a continuous flow container made of PMMA sheet as described in earlier publication [2]. A sandwich type container was fabricated by sealing two PMMA sheets as shown in Fig. 3.2. The fabricated container consisted of an inlet and outlet to allow the continuous flow of the nanofluids (Fig. 3.2). The total volume of the cell was 2 mL (2 cm x 1 cm x 1cm). The different nanofluids were supplied to the PMMA container utilising a syringe pump (Genie Touch, Kent Scientific Corporation) with flow rate ranging from 0.05 to 0.4 mL·min^{-1}.
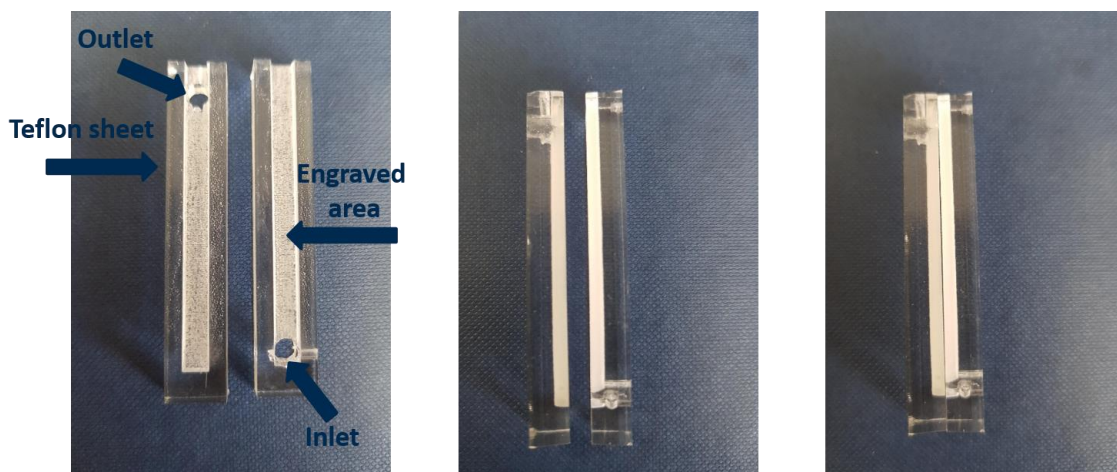
Figure 3.2. PMMA parts of continuous flow container used for laser induced plasmonic heating.

3.4.2 Fabrication of continuous flow reactor for photocatalytic oxidation of benzyl alcohol

A continuous flow reactor made of Teflon sheet was designed and fabricated using a Trotec Speedy 300 laser cutter/engraver following the design presented in section 3.4.1. Two Teflon sheets were cut/engraved in the desired dimensions and placed in such a way to seal a sandwich type reactor. Teflon sheets were used since PMMA sheets are not resistance to toluene, which used as solvent in the subsequent experiments. The continuous flow reactor consisted of an inlet and outlet to allow the flow of the electrolyte containing the dispersed as-synthesized photocatalysts. The total volume of the reactor chamber was 2 mL (2 cm x 1 cm x 1cm). A syringe pump (Genie Touch, Kent Scientific Corporation) was utilized to supply the O_2-purged solution to the reactor with flow rates in the range between 0.05 to 0.2 $mL \cdot min^{-1}$. A schematic illustration of the continuous flow reactor made by Teflon sheets is shown in Fig. 3.3.
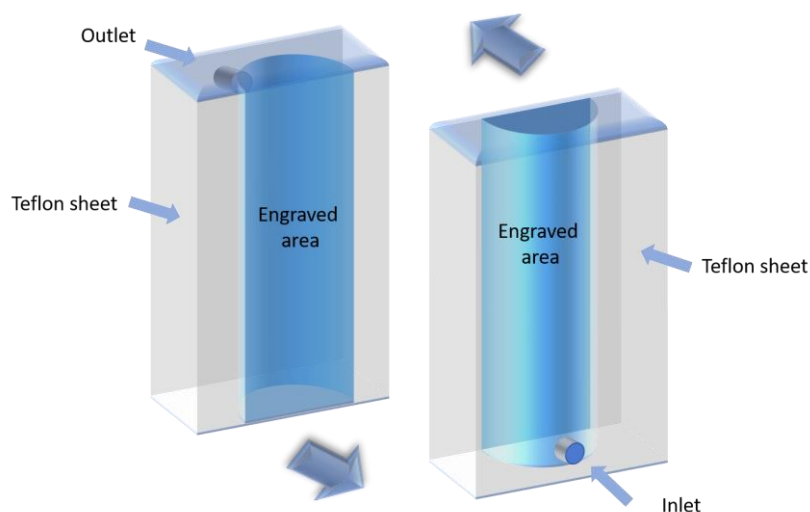
Figure 3.3. Schematic representation of Teflon parts of continuous flow reactor for photocatalytic oxidation of benzyl alcohol.

3.5 Materials testing

3.5.1 Laser induced plasmonic heating using Au/TiO$_2$ nanoparticles

A schematic illustration of the experimental set-up is presented in Fig. 3.4 [11]. The continuous flow container was irradiated from the top using 532 nm laser light while the top was covered with quartz glass. Two k-type thermocouples were installed to the data acquisition unit plugged in a computer and were placed after the inlet (before illumination) and before the outlet (after laser illumination) of the container to monitor the temperature (Fig. 3.4). Temperature measurements were recorded with PicoLog thermocouple data logger (TC-08) until a thermal steady state has been reached. The starting temperature of TiO$_2$ and Au/TiO$_2$ water-based nanofluids was 20.3˚C and the error bar was estimated at ±0.1 ℃.
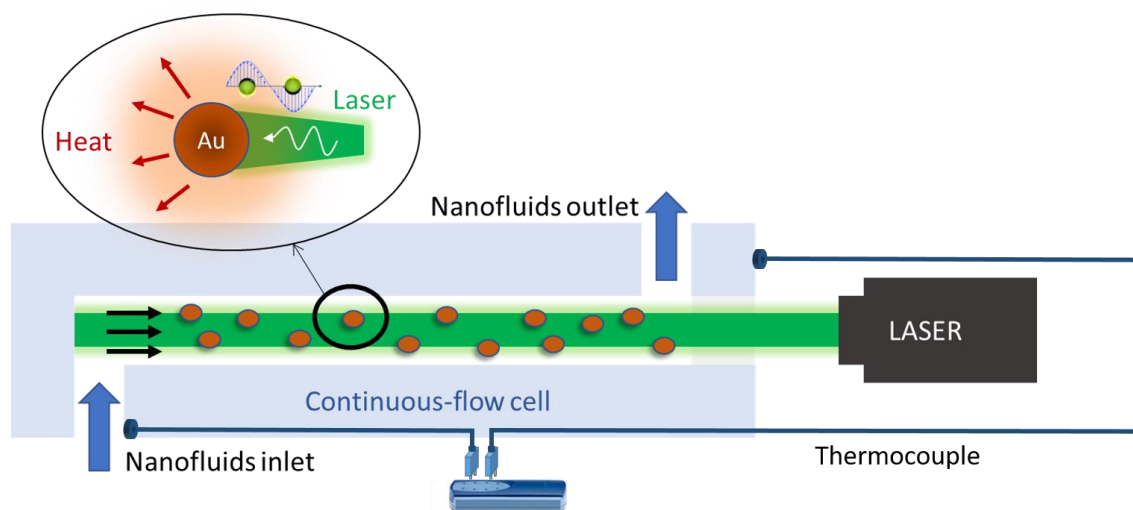
Figure 3.4. Schematic representation of experimental set-up for laser induced plasmonic heating under continuous flow conditions.

3.5.2 Photocatalytic oxidation of benzyl alcohol

The photocatalytic performance of monometallic Au/Cr_2O_3, Ag/Cr_2O_3 and bimetallic $Ag-Au/Cr_2O_3$ microspheres was evaluated by benzyl alcohol photo-oxidation under 500 mW, 532 nm laser irradiation using two different types of reactor: A batch type reactor (5 mL round bottom flask, Fig. 3.5) and the fabricated continuous flow reactor (Fig. 3.6). 1 mg/mL of photocatalyst was dispersed in toluene (solvent) containing 0.1M benzyl alcohol (reactant) and then the suspension was ultrasonicated and purged with O_2. The top of the reactors was covered with quartz glass to allow the light source inside. The temperature of the systems was controlled by a water bath at 21 °C running through the outer case of the reactors to avoid light induced heating. Two k-type thermocouples were installed to the data acquisition unit plugged in a computer and were placed after the inlet (before illumination) and before the outlet (after laser illumination) of the continuous flow reactor to monitor the temperature. In case of continuous flow experiments, the O_2-purged solution was supplied to the reactor using a syringe pump with different flow rates in the range between 0.05 to 0.2 mL·min^{-1} (Fig. 3.6). The photocatalytic oxidation of benzyl alcohol was carried out under 532 nm laser irradiation at room temperature.
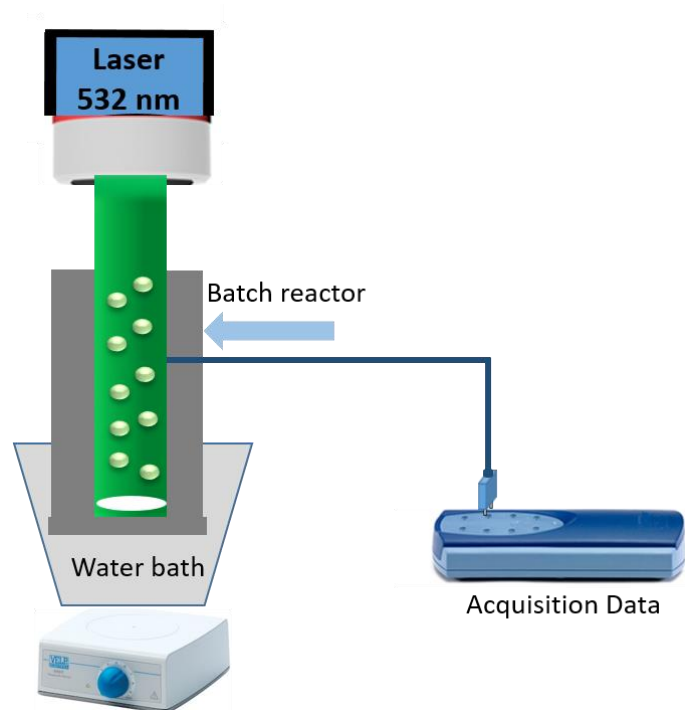
Figure 3.5. Schematic representation of experimental set-up for for photocatalytic oxidation of benzyl alcohol.

Figure 3.6. Schematic representation of experimental set-up for photocatalytic oxidation of benzyl alcohol under continuous flow conditions.

Blank experiments were conducted in the absence of photocatalyst and light. Controlled experiments were performed to explore the mechanism of benzyl alcohol photo-oxidation utilising different trapping agents such as tert-butyl alcohol (TBA), ammonium oxalate (AO), AgNO$_3$ and 1,4-benzoquinone (BQ), which served as the hydroxyl radical (OH$\cdot$), hole (h$^+$), electron (e$^-$) and superoxide radicals ($\cdot$O$_2^-$) scavengers respectively. For controlled experiments, 50 μmol of radical scavengers were added to the above photocatalytic oxidation reaction system. To test the recyclability of Au/Cr$_2$O$_3$, after completion of the reaction, the catalyst was collected by filtration, air-dried at 75 °C overnight and re-used for the subsequent reaction cycles. Benzyl alcohol conversion and benzaldehyde selectivity of aldehyde were defined using the equations as follows:

$$Conversion\ (\%) = [\,C_0 - C_{alcohol})/C_0]\ x\ 100\% \tag{3.6}$$

$$Selectivity\ (\%) = \left[\frac{C_{aldehyde}}{C_0 - C_{alcohol}}\right] x 100\% \tag{3.7}$$

where C$_0$ is the concentration of alcohol prior to reaction initiation, C$_{alcohol}$ is the remaining concentration of alcohol after 3 h irradiation and C$_{aldehyde}$ is the concentration of formed benzaldehyde after 3 h irradiation.

3.5.3   Photocatalytic degradation of methyl orange using peristaltic pump

Photocatalytic degradation of methyl orange (MO) was carried out using 0.84 wt.% Au/TiO$_2$ NPs as photocatalyst in a commercial photochemical flow reactor equipped with an LED lamp with emission at 530 nm (easy-Photochem from Vapourtec) as described above. Fig. 3.7a illustrates the experimental setup used for the MO degradation. 5 mg of Au/TiO$_2$ NPs were dispersed into a 10 mL aqueous solution containing 10 mg/L MO. The suspension was then pumped into the reactor circularly using a peristaltic pump at a flow rate of 1 mL/min employing 1 mm PTFE tubing. The dispersion was cycled for the required time and 0.2 mL samples were collected at regular interval times and analysed using UV-Vis spectrophotometer. The use of peristaltic pump enables the heterogeneous mixture to pass easily through the system and offers consistent light penetrations and controlled exposure times. Fig. 3.7b shows the UV-Vis absorption spectra of the pristine MO solution (before irradiation) and that of the decomposed dye solutions in the presence of Au/TiO$_2$ photocatalyst, which

clearly indicate decomposition of MO along with decrease in absorbance over irradiation time.
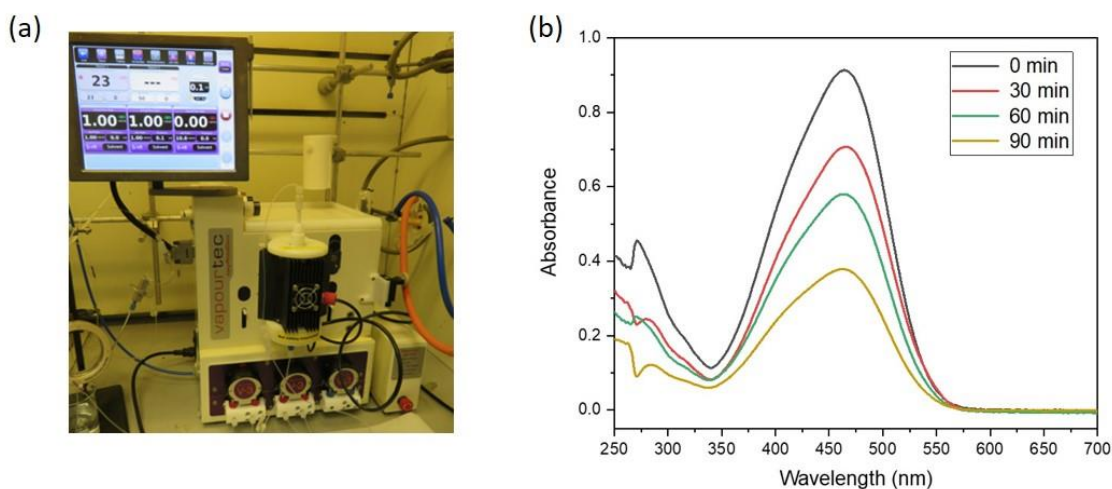
Figure 3.7. (a) Experimental set-up of the Photochem flow reactor from Vapourtec and (b) UV-Vis spectra of MO under LED irradiation.

3.6   Analytical techniques

3.6.1   Background

Gas chromatography (GC) is a widely used analytic technique for separation and quantification of chemical compounds [12]. A gas chromatograph consists of an injector, a column and a detector. A small amount of sample is introduced to the injector, which has a dual mode of sample vaporization and mixing with the carrier gas. Then, the injected sample passes through a column with controlled temperature where it takes place the separation of the different analytes. At the end of the column the carrier gas passes through the detector prior to atmosphere exposure. High purity hydrogen, helium and nitrogen are the most common carrier gases.

3.6.2   Experimental

The starting materials and reaction mixture were analyzed by a gas chromatograph equipped with flame ionization detector (FID) using DB-624 capillary column and He as carrier gas. Particularly, 2 μL of the testing sample were injected in the GC with the following operating conditions: Initially, oven temperature was set at 40 ºC and hold for 2 min. Then, a raise from 40 ºC to 200 ºC was conducted at a heating rate of 5 ºC/min and hold for 20 min. Total run time was 35 min while Helium was used as a carrier gas. GC peak area can be used to identify and quantify the benzyl alcohol (reactant) and

benzaldehyde (expected product) concentration. For this purpose, two calibration curves with known concentrations (mol/mL) of benzyl alcohol and benzaldehyde which permit the quantification of concentration in tested samples were developed. Benzyl alcohol and benzaldehyde were diluted in toluene solutions in different concentrations to set up the desired calibration tables. As it can be seen, (Fig. 3.8-3.9) both calibration curves exhibit a linear trend with correlation $R^2>0.99$. From the calibration curves, the qualitative and quantitative analysis of the reactants consumed over irradiation time and products formed was established.
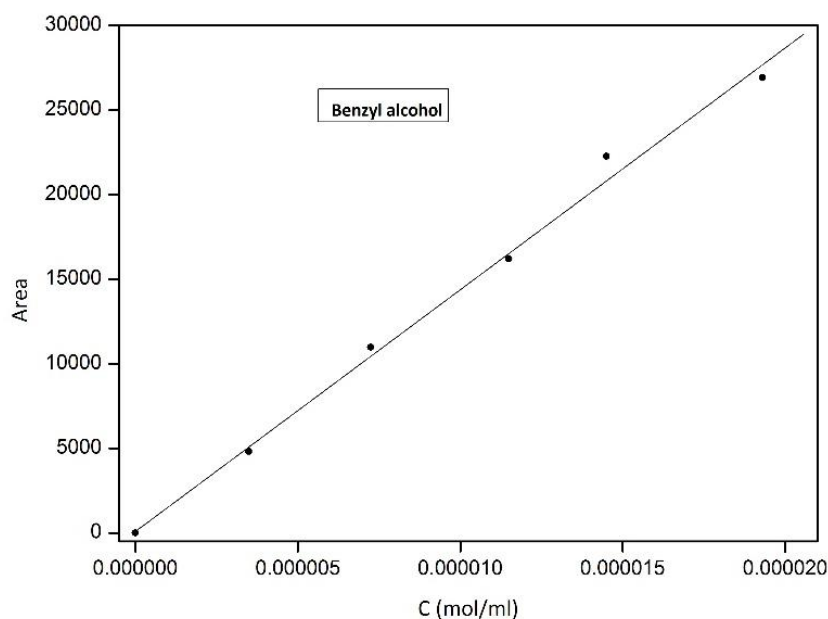
Figure 3.8. Calibration curve for benzyl alcohol.
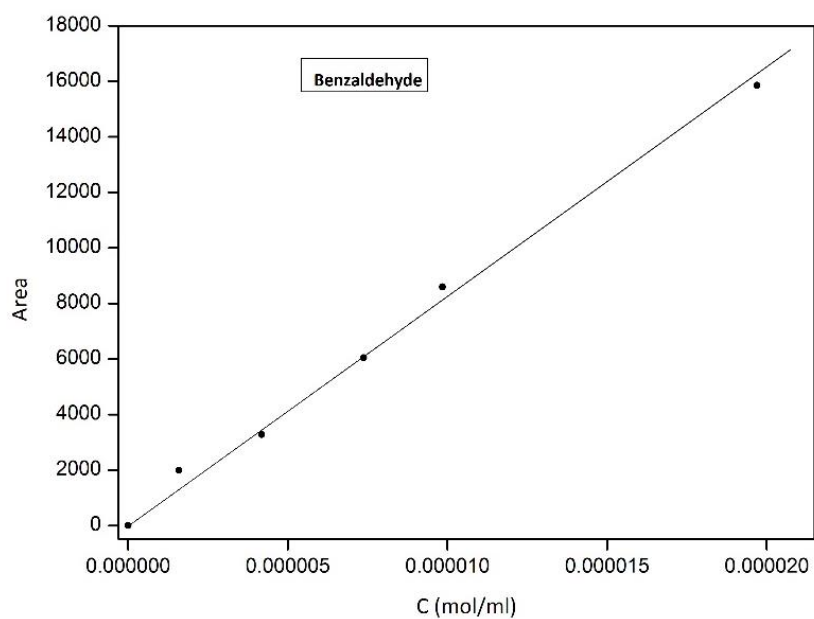
Figure 3.9. Calibration curve for benzaldehyde.

Each time a blank run was conducted before injecting the samples into GC to ensure that no impurities were left in the column. Gas chromatographic peaks of pure toluene, benzyl alcohol and benzaldehyde were identified at 6.7, 20.1 and 18.6 min retention time respectively.

3.7 References

[1] H. Xu, T. Lou, Y. Li, Synthesis and characterize of trivalent chromium $Cr(OH)_3$ and Cr_2O_3 microspheres, Inorganic Chemistry Communications, 7 (2004) 666-668.

[2] L. Collado, A. Reynal, J.M. Coronado, D.P. Serrano, J.R. Durrant, V.A. de la Peña O'Shea, Effect of Au surface plasmon nanoparticles on the selective CO_2 photoreduction to CH_4, Applied Catalysis B: Environmental, 178 (2015) 177-185.

[3] Y. Xu, Q. Lin, B. Liu, F. Jiang, Y. Xu, X. Liu, A Facile Fabrication of Supported Ni/SiO_2 Catalysts for Dry Reforming of Methane with Remarkably Enhanced Catalytic Performance, Catalysts, 9 (2019) 183-191.

[4] P.-C. Lin, S. Lin, P.C. Wang, R. Sridhar, Techniques for physicochemical characterization of nanomaterials, Biotechnology Advances, 32 (2014) 711-726.

[5] B.J. Inkson, (2016), Scanning Electron Microscopy (SEM) and Transmission Electron Microscopy (TEM) for Materials Characterization, in Materials Characterization Using Nondestructive Evaluation (NDE) Methods, Woodhead Publishing, pp. 17-43.

[6] Lamas D.G., Neto M., Kellermann G., Craievich A.F., (2017), X-Ray Diffraction and Scattering by Nanomaterials, in Nanocharacterization Techniques, William Andrew Publishing, pp. 111-182.

[7] Pazos-Perez N., Alvarez-Puebla R. (2012), Surface Enhanced Raman Spectroscopy (SERS)-Encoded Particles, in Raman Spectroscopy for Nanomaterials Characterization, Springer Berlin Heidelberg, pp. 33-49.

[8] Peña-Rodríguez O, Pal U (2013), Exploiting the tunable optical response of metallic nanoshellS, in UV-VIS and Photoluminescence Spectroscopy for Nanomaterials Characterization XII, Springer Berlin Heidelberg, pp. 99-149.

[9] X. Shi, L. Cai, M. Ma, X. Zheng, J.H. Park, General Characterization Methods for Photoelectrochemical Cells for Solar Water Splitting, ChemSusChem, 8 (2015) 3192-3203.

[10] E. Kalamaras, M. Belekoukia, J.Z.Y. Tan, J. Xuan, M.M. Maroto-Valer, John M. Andresen, A microfluidic photoelectrochemical cell for solar-driven CO_2 conversion into liquid fuels with CuO-based photocathodes, Faraday Discussions, 215 (2019) 329-344.

[11] M. Belekoukia, E. Kalamaras, J.Z.Y. Tan, F. Vilela, S. Garcia, M.M. Maroto-Valer, J. Xuan, Continuous flow-based laser-assisted plasmonic heating: A new

approach for photothermal energy conversion and utilization, Applied Energy, 247 (2019) 517-524.

[12] Stauffer E., Dolan J.A., Newman R., (2008), Gas Chromatography—Mass Spectrometry, in Fire Debris Analysis, Academic Press, Burlington, pp. 235-293.

Chapter 4- Continuous Flow-Based Laser-Assisted Plasmonic Heating: A New Approach for Photothermal Energy Conversion and Utilization

4.1 Introduction

As described in Chapter 2, metal NPs such as Au, Ag and Cu exhibit considerable photothermal performance due to their unique characteristics such as absorption of photons and scattering [1]. Metal nanoparticles convert the absorbed photons to heat energy, which is then transferred to surrounded medium, increasing the temperature. Plasmonic metal nanoparticles have been used in different applications including industrial and residential process heat, biomedical applications and photocatalytic processes, due to their significant improvement of optical absorption and photothermal effect, which is attributed to the LSPR effect on the surface of plasmonic nanoparticles. For instance, Chen and co-workers performed several experimental studies on the optical properties of metal NPs (Au NPs size – 25, 33 and 40 nm, Au NPs size – 10 nm and Ag NPs size – 30 nm)) and the photothermal conversion efficiency of thermal collectors [2-4]. The results indicated that nanofluids containing Au and Ag obtained the highest photothermal conversion efficiency. Qin and co-workers investigated the heat generation of gold nanoparticles (10 -100 nm) for photothermal therapy under laser irradiation [5]. In another study, Wang *et al.* reported that the photothermal effect generated by Au nanorods (1.4, 1.9, 2.3 and 3.7 wt% Au loading, width and length of Au nanorods were 12 nm and 34 nm with an aspect ratio of 2.9) supported on TiO_2 microspheres promoted the RhB degradation rate [6].

Among the noble metals, Au NPs have higher chemical stability to oxidation compared to Ag and Cu and relatively high absorption and scattering properties, which enable them more attractive metals for photothermal applications [3, 7, 8]. Although plasmonic metal NPs have shown a good activity in photochemical processes they are not considered as ideal materials for large-scale applications due to aggregation, low stability and high-cost. For this reason, metal oxide materials are used as supports to further enhance the functionality and stability of metal NPs by providing a large surface area to enable a uniform dispersion of metal [7, 9]. TiO_2 is one of the most promising semiconductors that favours from its chemical and thermal stability and has been employed as an efficient support for particularly low Au loadings under visible light to

promote effectively several plasmonic photocatalytic and photoelectrocatalytic processes [10, 11].

So far, as described in Chapter 2, many studies have investigated the feasibility of using plasmonic metals in photothermal processes. Although there have been many approaches in photothermal heat generation from plasmonic nanoparticles, these studies mainly investigated the optical properties of the nanoparticles with limited photothermal experiments and evaluation of the parameters that affect significantly the efficiency of photothermal conversion.

Additionally, the existing technology of batch-type systems that have been mainly used in photothermal processes has limitations in large-scale applications due to long time-scale of operation hours [3, 4]. Development of a continuous-flow system is a promising approach to deal with the required needs of designing a system that comprises advanced light harvesting and reduction of photon loss, characteristics that can ensure a photothermal process with high conversion efficiency [12-14].

The objective of this Chapter was to systematically investigate the surface plasmon resonance and particularly the plasmonic heating effect of Au NPs evaluating their potential use in photocatalytic processes. Herein, plasmonic heating experiments of Au NPs decorated on TiO_2 were performed under continuous flow conditions using visible laser irradiation. The developed flow system benefits from improved heat and mass transfer, enhanced light utilization and allows control of operating conditions over fluids. The optical and physical properties of Au/TiO_2 NPs with various Au loadings were characterized. Additionally, the effect of Au loading, flow rate, Au/TiO_2 NP concentration and laser intensity versus flow rate on the photothermal properties of nanofluids was explored by measuring the temperature change.

4.2 Results and discussion

4.2.1 Characterization of Au/TiO_2 NPs

The structural properties of the plasmonic NPs were identified by X-Ray diffraction, as shown in Fig. 4.1. The presence of anatase and rutile phases of TiO_2-P25 was confirmed by the XRD patterns. The diffraction peaks detected at $2\theta = 25°$, $38°$ and $48°$ were indexed to lattice planes (101), (004) and (200) of anatase phase while the diffraction peaks at $2\theta = 27°$, $41°$, $54°$ and $63°$ were assigned to (110), (111), (220) and (002) lattice planes of rutile phase of TiO_2 respectively. No characteristic peaks associated to Au were observed in the Au loaded TiO_2 samples. This can probably be attributed to the small particle size of Au NPs in accordance with TEM analysis (NPs, ≤

5 nm) and low Au concentration. Additionally, overlap of expected Au (111, 200) reflection peaks with TiO_2 anatase (004) and TiO_2 rutile (111) makes it difficult to identify Au particles.
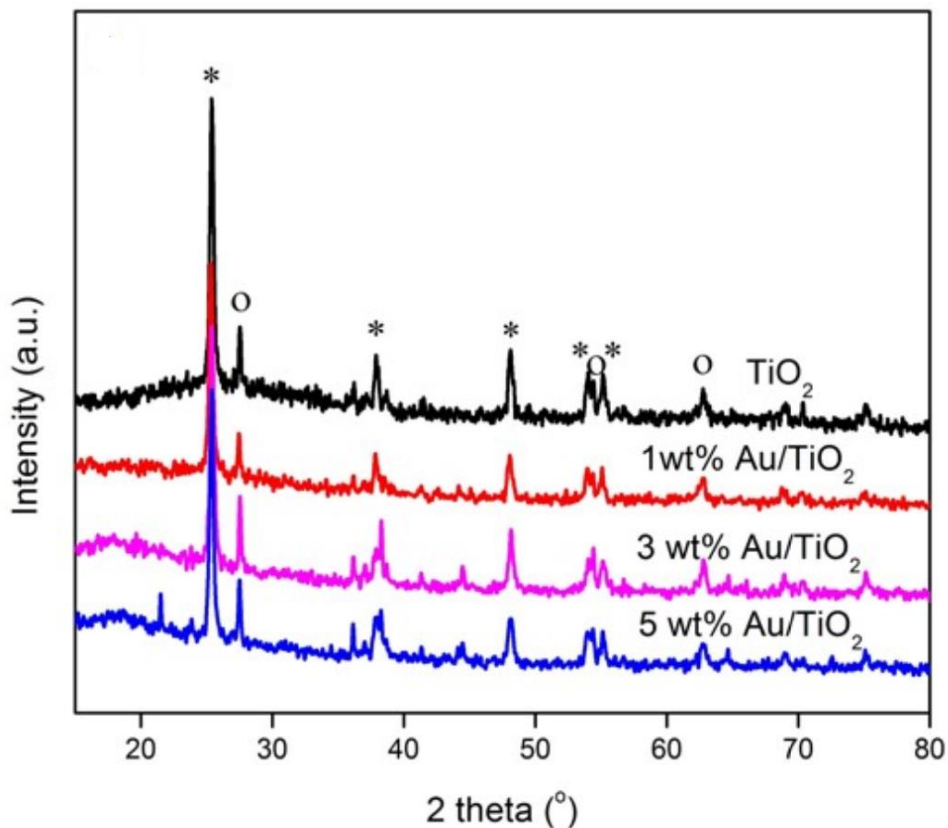
Figure 4.1. XRD pattern of pure TiO_2 anatase (*) and rutile (o) and Au/TiO_2 samples.

Further investigation of the crystal structure of Au/TiO_2 nanopowders was performed using Raman spectroscopy. Raman spectra of the different samples are shown in Fig. 4.2. The characteristic bands of anatase phase positioned at 142, 395, 515 and 638 cm^{-1}, which correspond to $E_g(1)$, $B_{1g}(1)$, A_{1g} + $B_{1g}(2)$ and $E_g(2)$ vibrational modes respectively, are present in all tested samples. After Au loading, no characteristic peak corresponding to Au nanoparticles was detected. However, for Au/TiO_2 samples, by increasing Au loading, the intensity of the main anatase peak at 142 cm^{-1} was slightly decreased as well as shifted to 145 and 147 cm^{-1} for 3 and 5 wt.% Au content respectively. This indicates that the Au loading created lattice distortions, known as crystalline defects within TiO_2, which increased by increasing Au content. As a result, the characteristic vibrational frequency of TiO_2 was affected [15, 16]. A further increase of Au content to 5 wt.%, led to a decrease of the intensity of 395, 515 and 638 cm^{-1}

peaks of TiO_2 which revealed the increased crystalline defects. This observation is in agreement with the large nanoparticles identified in TEM images.
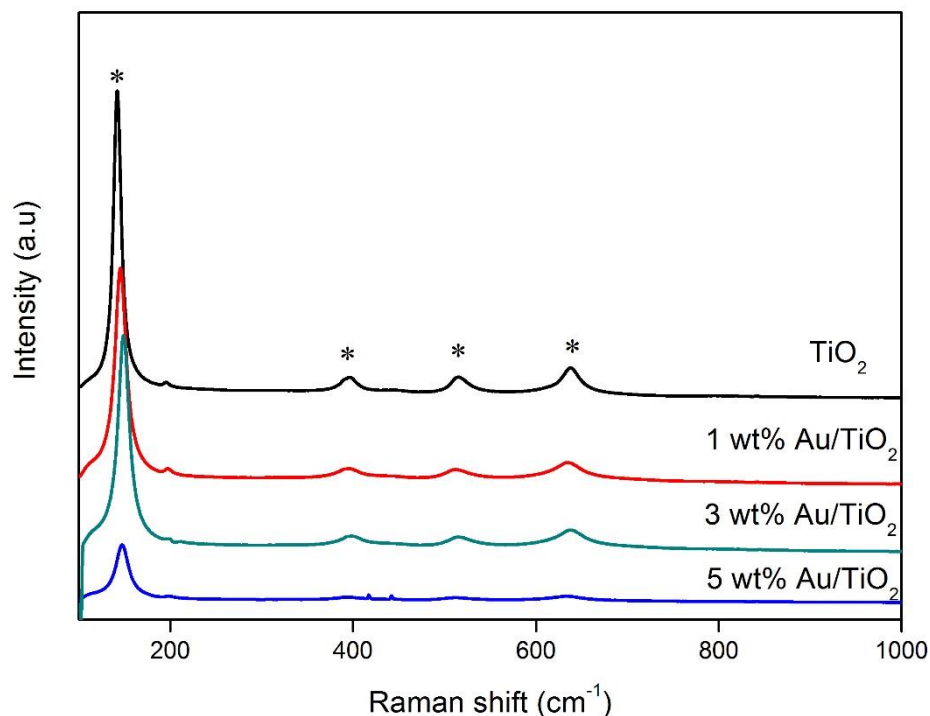
Figure 4.2. Raman spectra of pure TiO_2 anatase (*) and rutile (o) and Au/TiO_2 samples.

Fig. 4.3 shows the UV-Vis diffuse reflectance spectra (DRS) of bare TiO_2 and Au/TiO_2 samples. The pure TiO_2-P25 powder showed intense absorption below 400 nm. Contrary to pure TiO_2, Au/TiO_2 nanoparticles demonstrated a significant absorption in the visible region, particularly in the range 500-550 nm. This effect can be ascribed to the localised surface plasmon resonance (LSPR) of Au nanoparticles [17]. Additionally, an enhanced intensity of LSPR band at 532 nm was observed by increasing Au loading from 1 to 5 wt.%, which was also indicated by the color change of Au/TiO_2 powders from light to dark purple. This happens because the surface plasmon resonance wavelength is dependent on the metal content and particle size of noble metal [18].
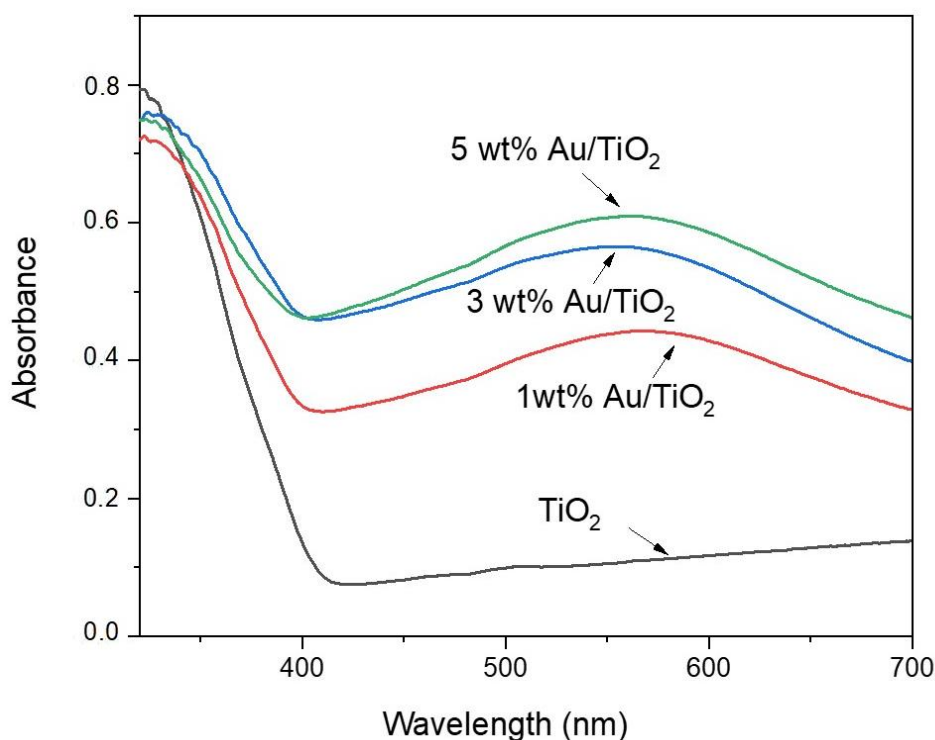
Figure 4.3. UV-Vis diffuse reflectance spectra of the as-prepared samples.

The energy bandgap of the synthesized samples was estimated (Fig. 4.4) utilizing the Kubelka-Munk function [19]:

$$F(R) = \frac{(1-R)^2}{2R} \tag{3.5}$$

The bandgap for P25-TiO$_2$ was estimated at 3.2 eV, which is in agreement with the literature. In case of Au loaded TiO$_2$ nanoparticles, an increase in the Au content from 1 to 5 wt.% led to a decrease of the band gap of TiO$_2$. Specifically, the band gap values were found at 3.07, 2.88 and 2.96 eV for 1, 3 and 5 wt.% Au, respectively. The decrease of TiO$_2$ bandgap stems from increased crystalline defects within TiO$_2$ by increasing Au loading. It has been reported that the electrons transferred from TiO$_2$ to Au cause shifting of the Fermi level closer to the conduction band of TiO$_2$ until the two systems reach an equilibrium [20, 21]. Therfore, the involved band edge energy in the electron transfer between metal and semiconductor is lower than that of bare TiO$_2$.
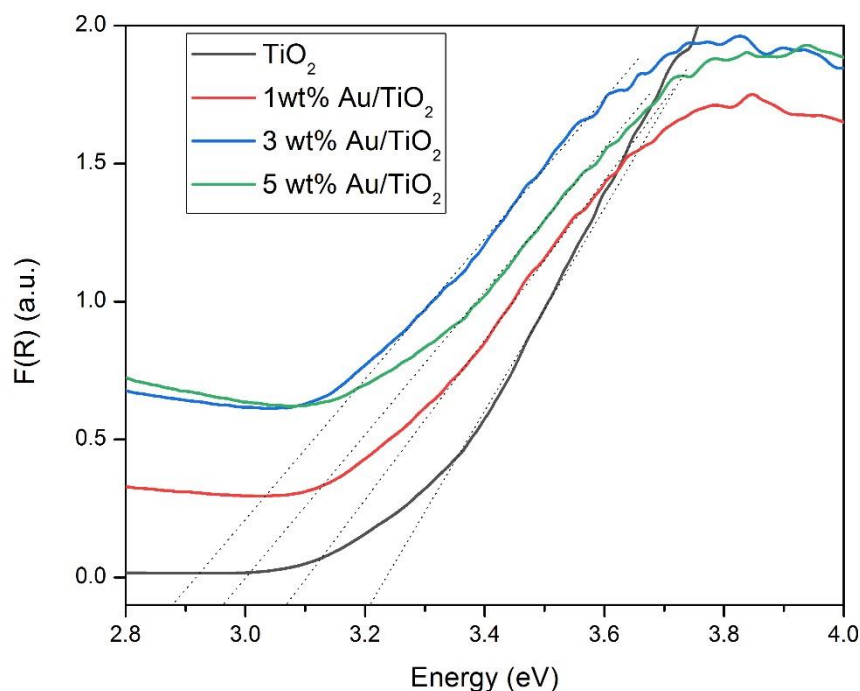
Figure 4.4. Plots of transformed Kubelka–Munk function versus the energy of absorbed light of the as-prepared samples.

The morphology of the samples with different Au loading (1, 3 and 5 wt. %) was studied by HR-TEM. It should be mentioned that no significant alternation was observed in the morphology of TiO_2 sample when Au NPs with different concentration were loaded. TEM images (Fig. 4.5a-c) showed that the surface of TiO_2 was uniformly decorated by a significant amount of small Au NPs. The concentration of Au increased by increasing the Au content to 3 and 5 wt.%. However, the average size of Au NPs enlarged with higher distribution upon further increasing the gold content and a few Au NPs tended to agglomerate in case of 5 wt.% (Fig. 4.5c). Specifically, nanoparticle size was calculated at 3.3, 3.6 and 8.1 nm for 1, 3 and 5 wt.% respectively. The crystalline structure of Au and TiO_2 NPs was confirmed from the ring pattern as it can be seen from the selected area electron diffraction (SAED) pattern (Fig 4.5d). The lattice spacing of 0.325 nm and 0.169 nm correspond to (110) and (211) crystal plane of rutile phase of TiO_2 while 0.235 nm correspond to (111) lattice fringe of Au.
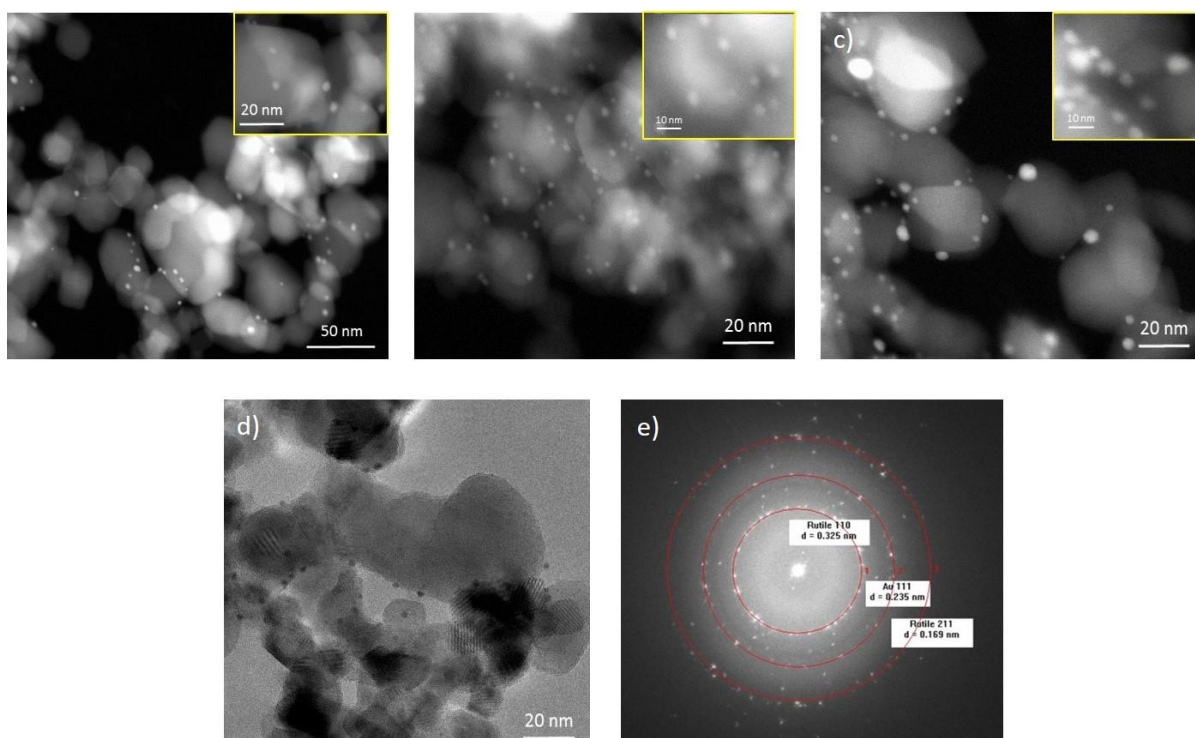
Figure 4.5. TEM images for a) 1 wt.% Au/TiO$_2$, b) 3 wt.% Au/TiO$_2$, c) 5 wt.% Au/TiO$_2$, d) TEM image of 3 wt.% Au/TiO$_2$ NPs and e) the selected area electron diffraction (SAED) pattern.

The presence of homogeneously distributed Au, Ti and O elements was confirmed using EDX elemental mapping (Fig. 4.6). Au NPs deposited on the surface of TiO$_2$ were clearly detected in the elemental mapping. EDX analysis showed that the amount of Au attached on TiO$_2$ surface during the synthesis process was lower than the nominal one. Approximately 40% reduction of the actual gold was observed, which is in agreement with the literature [10, 11]. More specifically, the nominal gold content was found to be 0.56, 0.84 and 1.89% for 1, 3 and 5 wt.%, respectively. This trend is highly related to the fact that the number of TiO$_2$ adsorption sites is reduced due to high pH values of synthesis solution leading to limited Au deposition [11]. It should be also noted that the deposition efficiency of this method decreases by increasing the amount of the gold in the synthesis solution. From this point, Au loaded photocatalysts will be named with their actual amount based on EDX measurments, 0.56 for 1 wt.%, 0.84 for 3 wt.% and 1.86% for 5 wt.%.
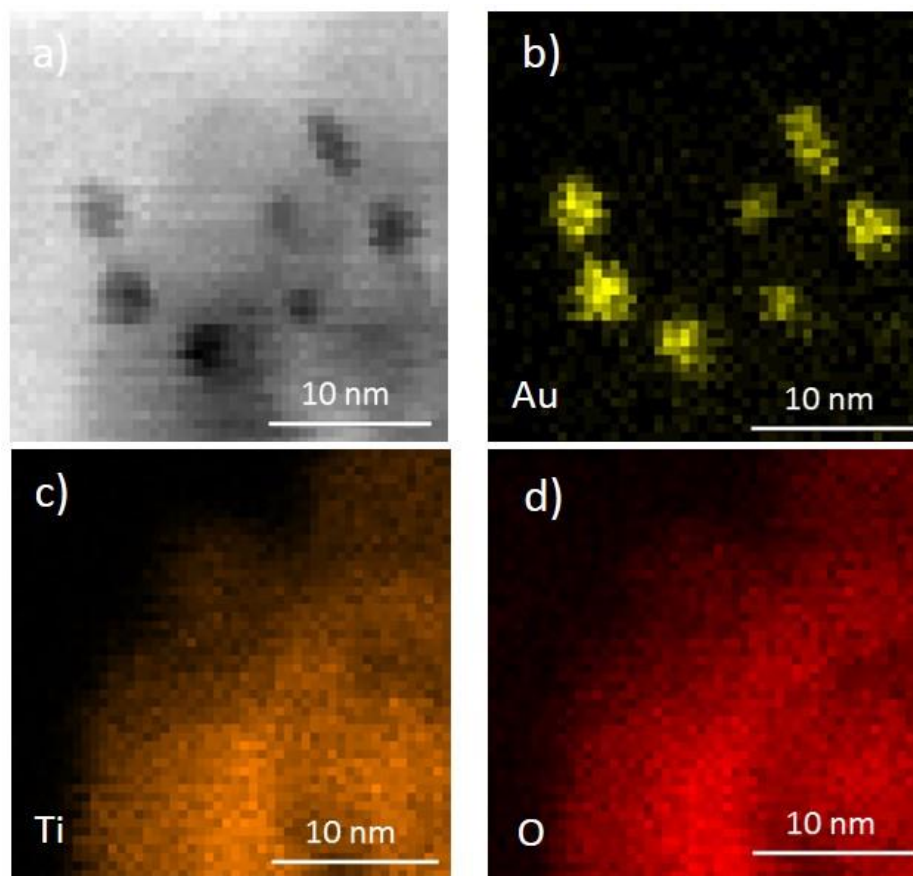
Figure 4.6. TEM-EDX mapping for 3 wt. % Au/TiO$_2$ sample.

4.2.2 Laser induced plasmonic heating

4.2.2.1 Photothermal effect

An experimental exploration of the effect of localized plasmonic heat produced by Au NPs was performed using 532 nm laser irradiation. Fig. 4.7 shows the recorded temperature profile of the different TiO$_2$ and Au/TiO$_2$ water-based nanofluids (0.6 mg mL^{-1}) under 532 nm laser excitation using a flow rate of 0.1 mL min^{-1}. The inlet temperature for the different nanofluids including pure water was 20.4 ± 0.1 ℃. All nanofluids presented higher temperature under laser irradiation compared to pure milli-Q water, in which temperature raised just ~ 0.5 ℃. A remarkable increase in temperature of Au nanofluid under laser irradiation can be seen in Fig. 4.7. It should be mentioned that the temperature of all Au/TiO$_2$ nanofluids was significantly higher compared to pure TiO$_2$ nanofluid (22.3 ℃), indicating a higher optical absorption of the nanoparticles. As expected, the different Au loading affected significantly the temperature profile. More specifically, the temperature reached up to 28.6 ℃ when 0.84 wt.% Au/TiO$_2$ nanofluid was used instead of 0.56 wt.% Au/TiO$_2$. However, a further increase of Au loading to 1.89 wt.% resulted in lower temperature compared to 0.84

wt.%. Generally, by changing the Au loading, parameters like Au particle size, morphology of the sample as well as the metal dispersion can be altered. The temperature decrease for higher Au loading is related to the increase of the mean size of Au NPs and to the formation of Au agglomerates, as can be seen from TEM images (Fig. 4.5). In case of excess Au loading, particles tend to agglomerate, resulting in limited conversion of the absorbed energy to thermal energy and thus the temperature increase is reduced. This phenomenon is attributed to the plasmonic coupling effect caused by particle interaction [22]. Additionally, nanofluids with small metal NPs have higher thermal conductivity compared to nanofluids consisting of larger NPs, which results to faster temperature increase of the nanofluid containing smaller NPs [23]. As a result, the temperature of the nanofluid containing smaller NPs increases faster in comparison with that of larger NPs.
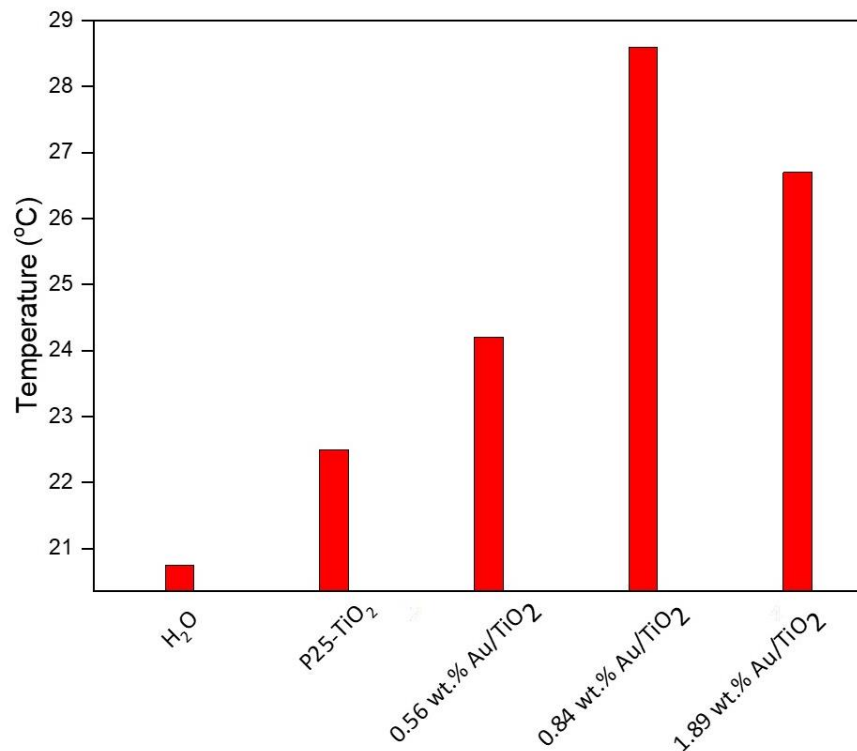
Figure 4.7. Temperature of pure milli-Q water, TiO_2 nanofluid and 0.56, 0.84 and 1.89 wt.% of Au/TiO_2 nanofluids for 0.6 mg mL^{-1} concentration 0.1 mL min^{-1} flow rate.

4.2.2.2 Effect of flow rate

The performance of different nanofluids at flow rates ranging from 0.05 to 0.4 mL min^{-1} was investigated (Fig. 4.8). For milli-Q water solution, no significant change of temperature was observed with different flow rates. In the case of nanofluids, the same trend was observed. By increasing the flow rate from 0.05 to 0.1 mL min^{-1} a higher temperature was achieved while a further increase of the flow rate up to 0.4 mL min^{-1}

led to the lowering of the temperature. At large residence time, the lower temperature observed is attributed to mass transfer limitations of the nanofluid due to low flow rate (< 0.1 mL min^{-1}) [24, 25]. Particularly, blocking effect was observed from the dispersed NPs in the fluid in flow rates lower than 0.1 mL min^{-1}. Under fast flow rates, mass transport is improved but the nanofluid doesn't remain under illumination for sufficient time to obtain the maximum temperature increase. All the different nanofluids, achieved the maximum temperature when an optimal flow rate was set at 0.1 mL min^{-1}. The highest recorded temperature for 0.84 wt.% Au loading using 0.1 mL min^{-1} flow rate was 28.6 ℃, while 1.8 ℃ decrease was noticed when the flow rate was set at 0.4 mL min^{-1}.
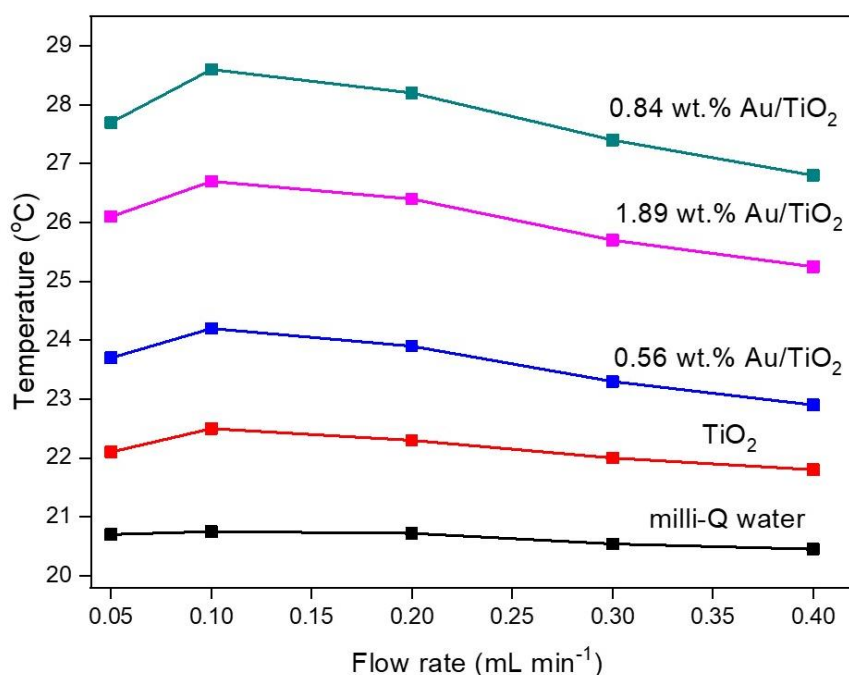
Figure 4.8. Temperature of pure milli-Q water, TiO$_2$ nanofluid and 0.56, 0.84 and 1.89 wt.% of Au/TiO$_2$ nanofluids for 0.6 mg mL^{-1} concentration and flow rates 0.05, 0.1, 0.2, 0.3 and 0.4 mL min^{-1}.

4.2.2.3   Effect of concentration

The effect of concentration on temperature performance using 0.84 wt.% Au/TiO$_2$ was further evaluated (Fig. 4.9). Four different nanofluids of 0.84 wt.% Au/TiO$_2$, with concentrations varied from 0.2 to 1.4 mg mL^{-1}, were prepared and tested under the same conditions as described above using flow rates between 0.05 and 0.4 mL min^{-1}. Fig. 4.9 shows a significant temperature rise by increasing Au NPs concentration up to 1 mg mL^{-1}. Among the tested nanofluids, the sample with 1 mg mL^{-1} concentration exhibited the highest temperature up to 31.5 ℃ with flow rate 0.1 mL min^{-1}. According to Beer-Lambert law, when the concentration of Au/TiO$_2$ NPs increased, the amount of

suspended nanoparticles in milli-Q water was higher, so more light was confined in the nanofluid, resulting in higher temperature [4]. However, upon further increasing the concentration to 1.4 mg mL^{-1}, the temperature significantly decreased to 26.3 $^{\circ}$C. This phenomenon can be ascribed to a possible saturation of the absorption of light caused by a further increase of the concentration [26].
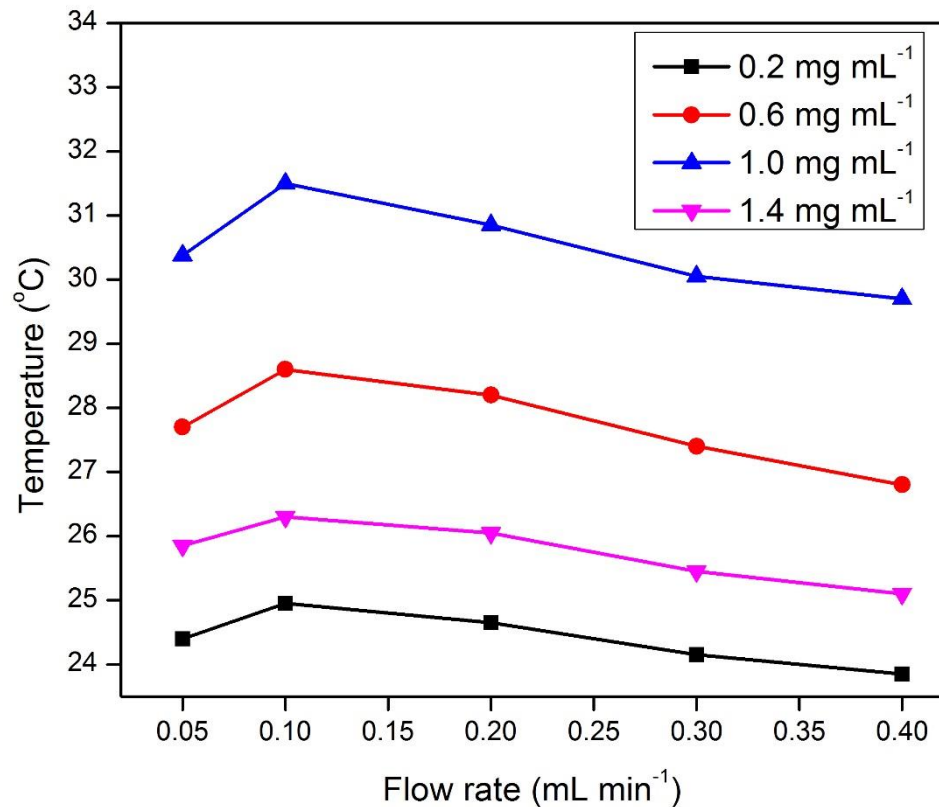
Figure 4.9. Temperature of 0.84 wt % Au/TiO$_2$ for 0.1 mL min^{-1} flow rate using 0.2, 0.6, 1.0 and 1.4 mg mL^{-1} concentration.

Fig. 4.10 shows that the optical absorption of Au/TiO$_2$ nanofluid increases up to 1 mg mL^{-1} concentration, while a further increase up to 1.4 mg mL^{-1} is causing a saturation in the optical absorption of the nanofluid, which can be attributed to a non-uniform distribution of NPs causing precipitation. For high concentration of nanofluid, laser light is mostly absorbed by the upper layer close to the surface while the lower layers of the nanofluid will not receive enough irradiation, resulting in increased heat loss from the surface to the walls of the reactor (low thermal conductivity but still possible to enable a small amount heat loss) [2]. Additionally, in case of high concentration, the interaction between the particles of the nanofluid should be considered. Particularly, the presence of both thermal superposition effect and plasmonic coupling with other NPs

increases the number of resonant clusters and therefore the probability of aggregations of NPs. In this way, plasmonic coupling affects negatively the photothermal performance by reducing the increase in the temperature [27].
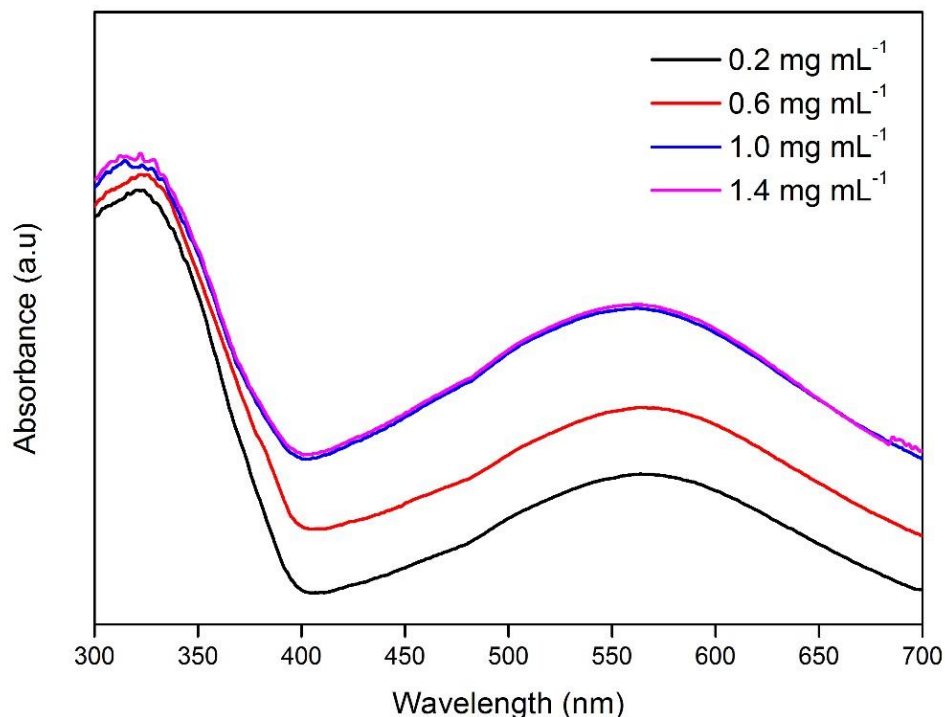
Figure 4.10. Absorbance of 0.84 wt.% nanofluid for different concentrations.

4.2.2.4   Effect of light intensity

Fig. 4.11 shows the temperature of the different nanofluids under laser irradiation at different power densities while the concentration of Au/TiO_2 and the flow rate were set to 1 mg mL^{-1} and 0.1 mL min^{-1} and respectively. As it can be seen, by increasing the laser power intensity, the Au nanofluid's temperature presented a remarkable rise. Specifically, a temperature increase of 11.5 $^{\circ}C$ caused by Au nanoparticles laser intensity of 63.3 W/cm^2 is the highest value obtained. The main reason for this phenomenon is that higher laser power density leads to higher light density, and thus, the heat generated by Au nanoparticles will subsequently increase. In this way, by increasing the laser intensity, a temperature rise of the heated medium can be achieved [8].
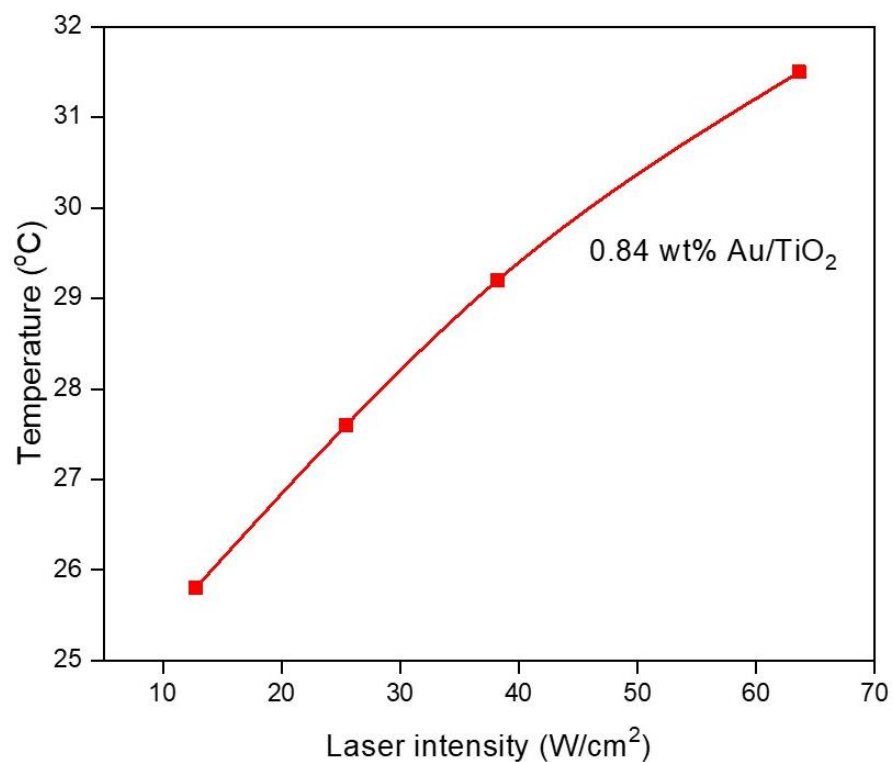
Figure 4.11. Temperature of 0.84 wt % Au/TiO_2 vs laser power intensity for 0.1 mL min^{-1} flow rate and 1 mg mL^{-1} concentration.

Finally, the stability of the samples was evaluated before and after the photothermal experiments using UV-Vis spectroscopy. UV-Vis absorbance spectra showed excellent stability of Au/TiO_2 nanofluids with a slight decrease of the absorption of 0.84 wt.% Au/TiO_2 sample as it can be seen in Fig. 4.12. Additionally, the TEM images unveiled no obvious change in the morphology and the size of Au NPs on TiO_2.
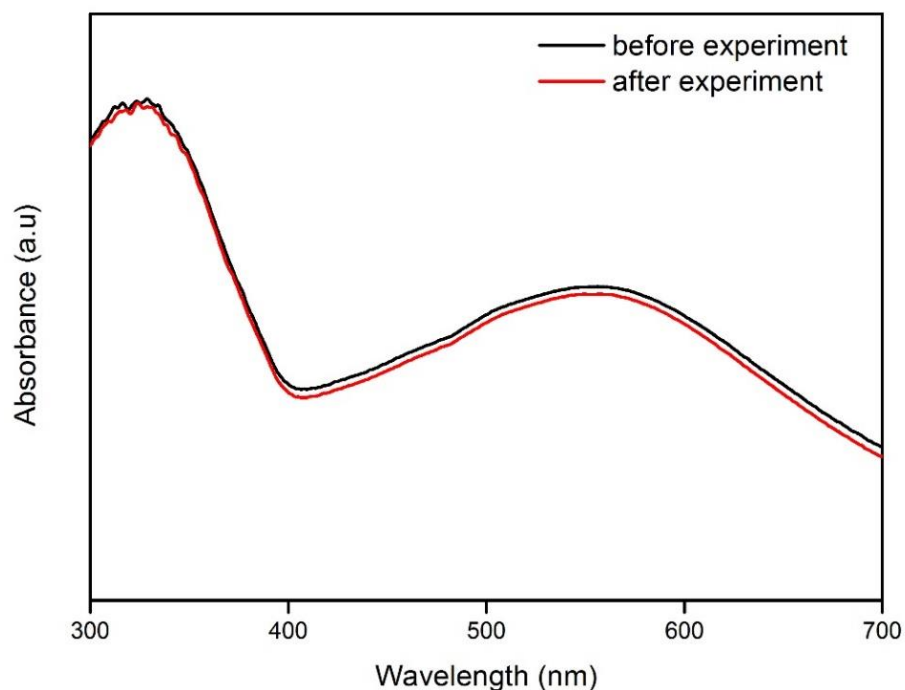
Figure 4.12. Absorbance of 0.84 wt.% nanofluid before and after photothermal experiment.

4.3 Conclusions

The work outlined in this Chapter met the objectives given to explore the plasmonic heating effect of Au nanoparticles under continuous flow conditions using 532 nm laser irradiation. Au nanoparticles were decorated on TiO_2 surface utilising deposition-precipitation method and the optical properties of Au/TiO_2 nanoparticles were investigated, indicating that plasmonic nanoparticles exhibited a remarkable absorption in the region 500-550 nm, attributed to the LSPR effect excited on Au NPs' surface. Regarding photothermal experiments it can be concluded that all the different nanofluids containing Au presented higher temperature compared to TiO_2 nanofluid and pure water showing the importance of plasmonic nanofluids. A further investigation of Au loading on the photothermal performance revealed the importance of Au content without excessive amounts to optimize plasmonic heating effect. From the tested samples, 0.84 wt.% Au/TiO_2 achieved the highest temperature (28.5 °C) while TiO_2 nanofluid reached 28.5 °C. However, a further increase of Au content to 1.89 wt.% led to a decrease in temperature (26 °C), indicating an excessive Au loading. Additionally, the influence of residence time of the fluid under laser irradiation was investigated. It was confirmed that the optimal flow rate was 0.1 mL min^{-1} for all nanofluids, while the

generation of plasmonic heating for 0.84 wt.% Au loading sample was further investigated by studying the effect of nanoparticle concentration and laser intensity. The results showed that temperature reached 31.5 °C upon increasing concentration to 1 mg mL^{-1} with laser intensity 500 mW, after which decreased significantly. It can be concluded that the presence of plasmonic nanoparticles and particularly NPs size and concentration affect remarkably the efficiency of photothermal processes.

This study offered an enhanced understanding of the fundamental aspects of plasmon-based photothermal performance under well-controlled continuous flow conditions. This work contributed to the overall aim of this thesis by demonstrating the surface plasmon resonance and particularly the photothermal effect of Au NPs. The concept of continuous-flow plasmonic heating of Au/TiO$_2$ nanofluid, enabled the research work in Chapters 5 and 6 by extending the use of plasmonic metals, which benefit from considerable optical and photothermal properties, in photocatalytic applications.

4.4 References

[1] P.K. Jain, X. Huang, I.H. El-Sayed, M.A. El-Sayed, Noble Metals on the Nanoscale: Optical and Photothermal Properties and Some Applications in Imaging, Sensing, Biology, and Medicine, Accounts of Chemical Research, 41 (2008) 1578-1586.

[2] M. Chen, Y. He, X. Wang, Y. Hu, Complementary enhanced solar thermal conversion performance of core-shell nanoparticles, Applied Energy, 211 (2018) 735-742.

[3] M. Chen, Y. He, J. Zhu, D.R. Kim, Enhancement of photo-thermal conversion using gold nanofluids with different particle sizes, Energy Conversion and Management, 112 (2016) 21-30.

[4] M. Chen, Y. He, J. Huang, J. Zhu, Synthesis and solar photo-thermal conversion of Au, Ag, and Au-Ag blended plasmonic nanoparticles, Energy Conversion and Management, 127 (2016) 293-300.

[5] Z. Qin, J.C. Bischof, Thermophysical and biological responses of gold nanoparticle laser heating, Chemical Society Reviews, 41 (2012) 1191-1217.

[6] X. Wang, M. Zhu, Y. Sun, W. Fu, Q. Gu, C. Zhang, Y. Zhang, Y. Dai, Y. Sun, Particle & Particle Systems Characterization, 33 (2016) 140-149.

[7] N. Zhou, V. Lopez-Puente, Q. Wang, L. Polavarapu, I. Pastoriza-Santos, Q.-H. Xu, Plasmon-enhanced light harvesting: applications in enhanced photocatalysis, photodynamic therapy and photovoltaics, RSC Advances, 5 (2015) 29076-29097.

[8] Z. Qin, J.C. Bischof, Thermophysical and biological responses of gold nanoparticle laser heating, Chemical Society Reviews, 41 (2012) 1191-1217.

[9] Q. Xiao, E. Jaatinen, H. Zhu, Direct Photocatalysis for Organic Synthesis by Using Plasmonic-Metal Nanoparticles Irradiated with Visible Light, Chemistry – An Asian Journal, 9 (2014) 3046-3064.

[10] V. Jovic, W.-T. Chen, D. Sun-Waterhouse, M.G. Blackford, H. Idriss, G.I.N. Waterhouse, Effect of gold loading and TiO_2 support composition on the activity of Au/TiO2 photocatalysts for H_2 production from ethanol–water mixtures, Journal of Catalysis, 305 (2013) 307-317.

[11] L. Collado, A. Reynal, J.M. Coronado, D.P. Serrano, J.R. Durrant, V.A. de la Peña O'Shea, Effect of Au surface plasmon nanoparticles on the selective CO_2 photoreduction to CH4, Applied Catalysis B: Environmental, 178 (2015) 177-185.

[12] F. Rechberger, M. Niederberger, Translucent nanoparticle-based aerogel monoliths as 3-dimensional photocatalysts for the selective photoreduction of CO_2 to methanol in a continuous flow reactor, Materials Horizons, 4 (2017) 1115-1121.

[13] D. Erickson, D. Sinton, D. Psaltis, Optofluidics for energy applications, Nat Photon, 5 (2011) 583-590.

[14] Y. Su, N.J.W. Straathof, V. Hessel, T. Noël, Photochemical Transformations Accelerated in Continuous-Flow Reactors: Basic Concepts and Applications, Chemistry – A European Journal, 20 (2014) 10562-10589.

[15] Y. Li, H. Wang, Q. Feng, G. Zhou, Z.-S. Wang, Gold nanoparticles inlaid TiO_2 photoanodes: a superior candidate for high-efficiency dye-sensitized solar cells, Energy & Environmental Science, 6 (2013) 2156-2165.

[16] T. Han, H. Wang, X. Zheng, Gold nanoparticle incorporation into nanoporous anatase TiO_2 mesocrystal using a simple deposition–precipitation method for photocatalytic applications, RSC Advances, 6 (2016) 7829-7837.

[17] D. Buso, J. Pacifico, A. Martucci, P. Mulvaney, Gold-Nanoparticle-Doped TiO_2 Semiconductor Thin Films: Optical Characterization, Advanced Functional Materials, 17 (2007) 347-354.

[18] C. Wang, O. Ranasingha, S. Natesakhawat, P.R. Ohodnicki, M. Andio, J.P. Lewis, C. Matranga, Visible light plasmonic heating of Au-ZnO for the catalytic reduction of CO2, Nanoscale, 5 (2013) 6968-6974.

[19] A.B. Murphy, Band-gap determination from diffuse reflectance measurements of semiconductor films, and application to photoelectrochemical water-splitting, Solar Energy Materials and Solar Cells, 91 (2007) 1326-1337.

[20] F. Cui, Z. Hua, C. Wei, J. Li, Z. Gao, J. Shi, Highly dispersed Au nanoparticles incorporated mesoporous TiO2 thin films with ultrahigh Au content, Journal of Materials Chemistry, 19 (2009) 7632-7637.

[21] S. Oros-Ruiz, R. Gómez, R. López, A. Hernández-Gordillo, J.A. Pedraza-Avella, E. Moctezuma, E. Pérez, Photocatalytic reduction of methyl orange on Au/TiO_2 semiconductors, Catalysis Communications, 21 (2012) 72-76.

[22] V. Siahpoush, S. Ahmadi-kandjani, A. Nikniazi, Effect of plasmonic coupling on photothermal behavior of random nanoparticles, Optics Communications, 420 (2018) 52-58.

[23] Q. He, S. Wang, S. Zeng, Z. Zheng, Experimental investigation on photothermal properties of nanofluids for direct absorption solar thermal energy systems, Energy Conversion and Management, 73 (2013) 150-157.

[24] L. Li, R. Chen, X. Zhu, H. Wang, Y. Wang, Q. Liao, D. Wang, Optofluidic Microreactors with TiO_2-Coated Fiberglass, ACS Applied Materials & Interfaces, 5 (2013) 12548-12553.

[25] N. Wang, Y.P. Zhang, L. Lei, H.L.W. Chan, X.M. Zhang, Photocatalytic Microreactor Using Monochromatic Visible Light, Advanced Materials Research, 254 (2011) 219-222.

[26] Y. Xuan, H. Duan, Q. Li, Enhancement of solar energy absorption using a plasmonic nanofluid based on TiO_2/Ag composite nanoparticles, RSC Advances, 4 (2014) 16206-16213.

[27] J. Xu, X. Yan, G. Liu, J. Xie, The critical nanofluid concentration as the crossover between changed and unchanged solar-driven droplet evaporation rates, Nano Energy, 57 (2019) 791-803.

Chapter 5 - High Performing Au-decorated Cr_2O_3 Microspheres for Laser Induced Photo-oxidation of Benzyl Alcohol to Benzaldehyde

5.1   Introduction

In Chapter 4, the plasmonic heating effect of Au NPs decorated on TiO_2 was evaluated under continuous flow conditions using visible laser irradiation and the surface plasmon resonance of Au NPs was confirmed. The concept of continuous-flow based plasmonic heating of Au/TiO_2 nanofluid could be promising in assisting photocatalytic oxidation reactions.

As explained in Chapter 2 (Section 2.4), coupling semiconductors with plasmonic metal nanoparticles (NPs) is an efficient approach to obtain high-efficient semiconductor photocatalysts [1-3]. So far, many studies have reported the utilisation of noble metals decorated on semiconducting metal oxides for the selective oxidation of aromatic alcohols. For instance, Tsukamoto *et al.* assessed the photocatalytic activity of Au NPs decorated on the commercial TiO_2 (P25) through benzyl alcohol oxidation with visible illumination (>450 nm), achieving 79% of benzaldehyde after 4 h of reaction [4]. In another study, Tao and co-workers demonstrated that the utilisation of Pd decorated on the $BiVO_4$ nanoflakes exhibited an enhanced activity for the photo-oxidation of benzyl alcohol under 300 W Xe lamp illumination for 8 h (53% conversion with 99% selectivity) compared to pure $BiVO_4$ nanoflakes (12% conversion) [5]. However, these photocatalysts mainly absorb light in the UV region with limited absorption to visible irradiation and have high recombination rate of the excited electron-hole pairs, restricting the overall photo-oxidation performance. Therefore, despite the significant advances made in the photo-oxidation of benzyl alcohol by decorating metal oxides with noble metals, there are still limitations in terms of reaction rate and photonic efficiency. Additionally, the existing studies have been devoted to enhancing the photocatalytic performance without efficient use of light energy resulting in long reaction time with limited yield.

Cr_2O_3, a *p*-type semiconductor known for its unique optical properties with a remarkable absorption both in the UV and visible region with absorption bands at 380, 460 and 600 nm, offers an alternative approach as support [6, 7]. Moreover, it is a chemically stable material with corrosion resistance and has been successfully used as a catalyst in different applications, including water oxidation, toluene oxidation, methyl orange degradation and H_2 production [8-11]. To the best of our knowledge, Au/Cr_2O_3

has not been used as the photocatalyst in the photocatalytic oxidation of aromatic compounds.

So far, most of the research work reported on photo-oxidation processes mainly focuses on solar irradiation and conventional artificial light sources. Several studies revealed that the use of monochromatic laser light offers a solution to overcome several demanding issues, including low reaction rate and low photonic efficiency [12-14]. Laser light benefits from its characteristic properties, including monochromaticity, coherence, directionality and high intensity. Particularly, the unique properties of laser light allow unprecedentedly high degree of control over reaction conditions for the production of high-value chemicals, resulting in enhancement of photocatalytic processes with high selectivity towards the desired product [15]. In addition, localized heating due to the LSRP allows low operating temperature, reducing energy consumption [16] and high reaction rate [17]. However, laser-assisted heterogeneously catalyzed oxidation of benzyl alcohol has not yet been performed.

The objective of Chapter 5 was to investigate the performance of Au NPs decorated on the surface of Cr_2O_3 microspheres *via* photocatalytic oxidation of benzyl alcohol to benzaldehyde under monochromatic visible laser irradiation as an efficient source of light. Cr_2O_3 microspheres were hydrothermally-synthesized and Au NPs were decorated on the surface of Cr_2O_3 using deposition-precipitation (DP) method and their optical and physical properties were explored. The production of benzaldehyde was evaluated by investigating the effect of Au loading, indicating the importance of optimised metal loading. Finally, the photothermal effect of Au NPs on the photocatalytic oxidation of benzyl alcohol to benzaldehyde was explored.

5.2   Results and discussion

5.2.1   Characterization of the fabricated Au/Cr_2O_3 photocatalysts

The crystal structure of Cr_2O_3 microspheres was characterised using X-Ray Diffraction (XRD) spectroscopy. Before annealing, amorphous trivalent chromium, $Cr(OH_3)$, was observed in the XRD pattern (Fig. 5.1a). After annealing at 900 °C, crystallized structure of Cr_2O_3 (JCPDS: 38-1479) corresponding to rhombohedral phase was obtained (Fig. 5.1b). The diffraction peaks at 2θ= 24.4°, 33.7°, 36.3°, 41.5°, 50.3°, 54.9°, 63.5° and 65.2 are indexed to (012), (104), (110), (113), (024), (116), (214), and (300) crystal planes of Cr_2O_3, respectively. No diffraction peaks associated to Au (Fig. 5.1c-e) were identified for all Au-loaded sample due to low Au concentration and small particle size of Au NPs (<10 nm, see TEM images, Fig. 5.6).
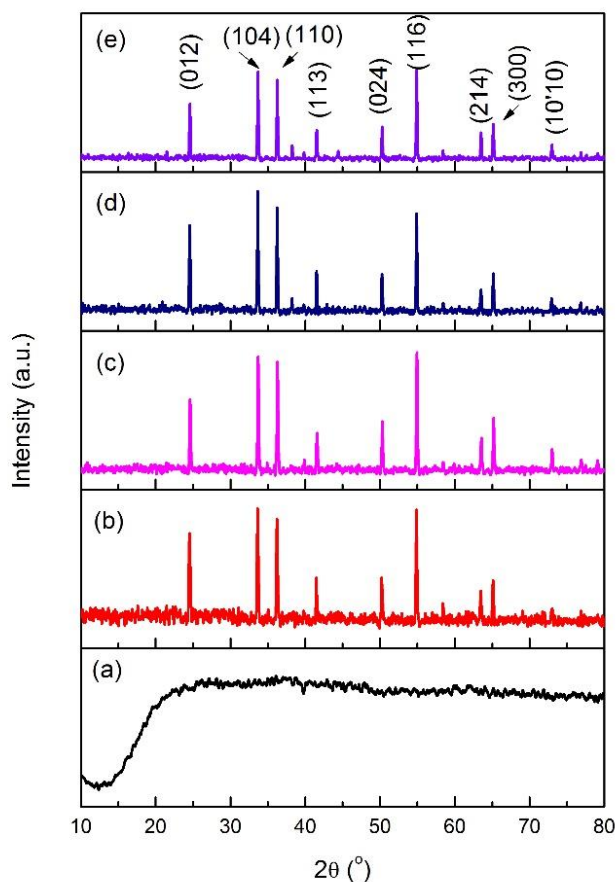
Figure 5.1. XRD pattern of (a) amorphous and (b) crystallized Cr_2O_3, (c) 1, (d) 3 and (e) 5 wt.% Au/Cr_2O_3 samples.

Raman spectroscopy was used to further investigate the crystal structure of Au/Cr_2O_3 (Fig. 5.2a). The peaks positioned at 308, 348, 548 and 607 cm^{-1} are assigned to the $E_g(2)$, $E_g(3)$, $A_{1g}(2)$ and $E_g(5)$ vibrational modes of Cr_2O_3, respectively. The highest band located at 548 cm^{-1} corresponds to A_{1g} symmetry, which agrees with the reported literature [28]. For Au loaded Cr_2O_3 samples, no characteristic Raman peaks of Au NPs were detected. However, slight changes in line intensity and position of the main Cr_2O_3 peak were observed after Au loading (Fig. 5.2b). Particularly, when the Au content gradually increased up to 5 wt.%, the intensity of Cr_2O_3 peak positioned at 548 cm^{-1} showed a significant decrease. In addition, the E_g peak at 548 cm^{-1} slightly shifted to higher wavenumbers 550, 551 and 553 cm^{-1} (Fig. 5.2b) for 1, 3 and 5 wt.% Au loading, respectively. The shifting of the main peak of Au/Cr_2O_3 samples compared to the pristine Cr_2O_3 can be attributed to the lattice distortions generation within Cr_2O_3 after Au loading. The formation of crystalline defects within Cr_2O_3 affected the vibrational frequency of Cr_2O_3, shifting the main peak to higher wavenumbers [10, 18].
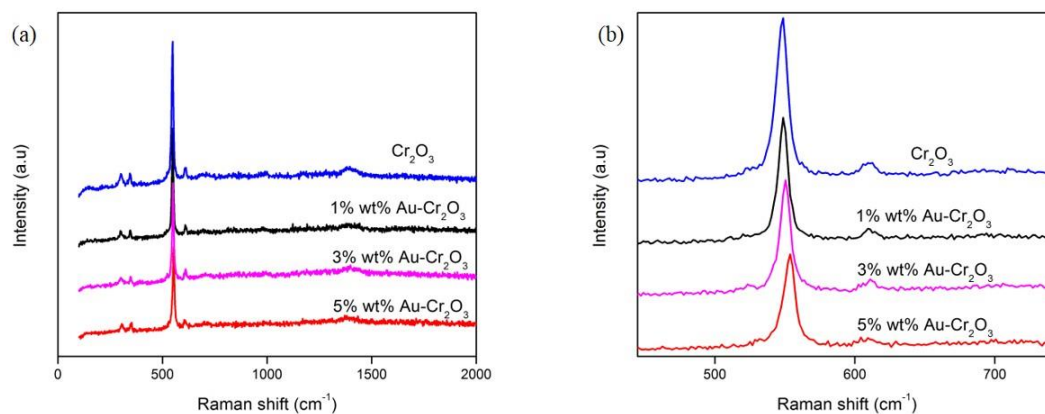
Figure 5.2. (a) Raman spectra and (b) zoomed in main peak of pure Cr_2O_3 and 1, 3 and 5 wt.% Au/Cr_2O_3 samples of Cr_2O_3.

The optical properties of pure Cr_2O_3 and Au/Cr_2O_3 photocatalysts were investigated using diffuse reflectance UV-Vis spectroscopy (Fig. 5.3). Cr_2O_3 microspheres presented a band in the UV region located at 380 nm and a significant absorption in the visible region with two well-defined absorption bands at 460 and 600 nm [11]. The absorption bands at 460 and 600 nm originate from the $^4A_{2g} \rightarrow {}^4T_{1g}$ and $^4A_{2g} \rightarrow {}^4T_{2g}$ electronic transitions of Cr_2O_3 respectively. The former is characteristic of Cr^{3+} ions in an octahedral environment and the latter implies d-d transition of Cr^{3+} in octahedral symmetry. As it can be seen from Fig. 5.3b, the synthesized Cr_2O_3 microspheres showed a green color with bandgap energy estimated using Kubelka-Munk function at 2.3 eV corresponding to the significant absorption in the visible region and a second band gap of 2.96 eV corresponding to the UV region. It should be noted that Au decorated Cr_2O_3 microspheres presented an enhanced absorption in the visible region, with a more intense broad band between 500-600 nm [19]. The absorption enhancement in the visible region was attributed to the LSPR induced electric field amplification of Au nanoparticles [20]. Plasmon band of Au NPs overlaps with the absorption of Cr_2O_3, which makes it difficult to identify clearly the strong visible absorption of Au NPs. However, upon increasing Au content to 5 wt.%, the intensity of LSPR band slightly increased. The Au deposition on Cr_2O_3 can be also confirmed with a slight change in the colour of the powder, in which the powder turned darker with increasing of Au content.
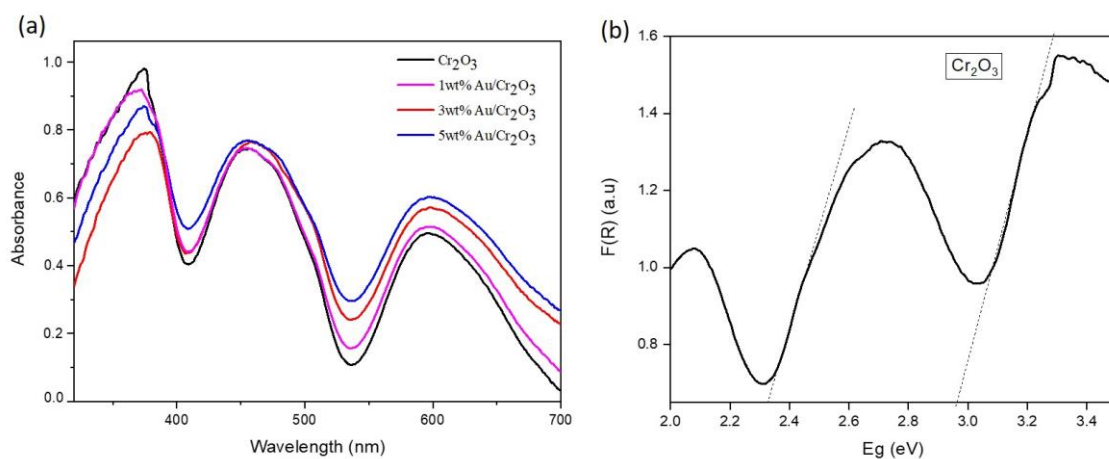
Figure 5.3. (a) UV-Vis diffuse reflectance spectra of Cr_2O_3 and 1,3 and 5 wt.% Au/Cr_2O_3 samples and (b) plots of transformed Kubelka–Munk function versus the energy of absorbed light of Cr_2O_3 sample.

The morphology of the prepared Cr_2O_3 and Au/Cr_2O_3 samples was studied using SEM and TEM. Fig. 5.4 shows SEM images of well-shaped Cr_2O_3 microspheres prepared by hydrothermal synthesis before and after calcination at 900 °C. The average diameter of the microspheres composed of smaller nanoparticles is approximately 0.5 μm.
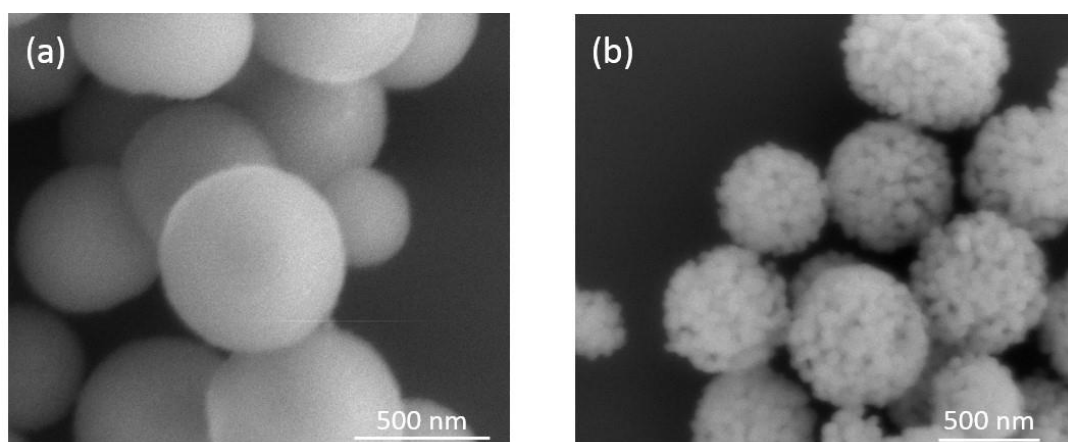
Figure 5.4. SEM images of Cr_2O_3 microspheres (a) before and (b) after calcination.

Raspberry-like structured microspheres were obtained after calcination. The spherical shape and particles size were maintained, indicating the stability of the microspheres at 900 °C (Fig 5.4b). Under closer examination (Fig 5.5), it can be seen that the annealed Cr_2O_3 microspheres are composed of smaller nanoparticles. Au nanoparticles with different loadings (1, 3, and 5 wt.%) were uniformly decorated on the surface of the Cr_2O_3 microspheres used as support (Fig. 5.5b-d). When the Au content increased from 1 to 5 wt.%, the concentration of Au NPs was significantly increased. Nevertheless, for Au loadings higher than 3 wt.%, larger Au NPs were formed while agglomeration of a

few Au NPs was also observed. The average size of Au NPs for 1, 3 and 5 wt.% was estimated at 3.5, 4.2 and 10.8 nm, respectively.
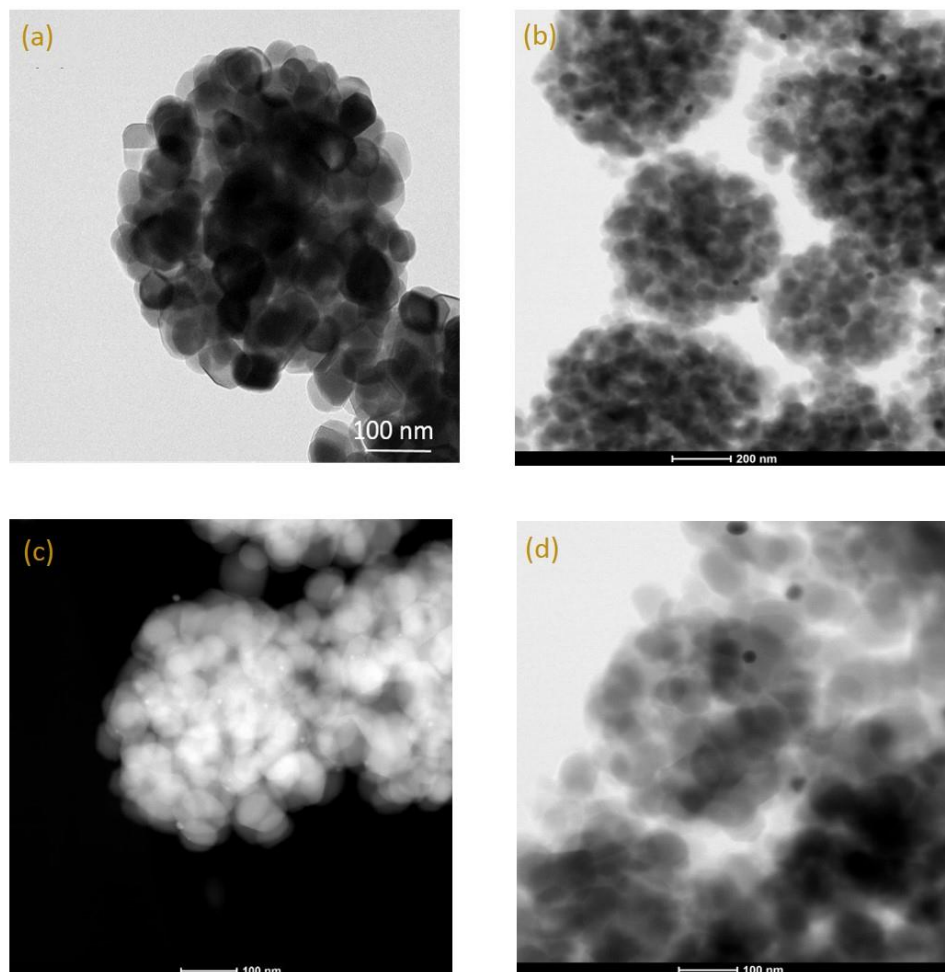
Figure 5.5. (a) HRTEM image of Cr_2O_3 microspheres after calcination and STEM images of (b) 1 wt.%, (c) 3 wt.% and d) 5 wt.% Au/Cr_2O_3 samples.

The Au NPs were homogenously distributed on the surface of Cr_2O_3 microspheres (Fig. 5.6). EDX analysis for elemental composition of Au, Cr and O revealed that the total nominal Au content utilised during DP synthesis method was ~40% less than the actual Au added. The actual Au content for 1, 3 and 5 wt.% samples was 0.64, 1.18 and 1.82%, respectively. The limited Au deposition can be ascribed to the high pH of the solution during the synthesis, causing reduced number of Cr_2O_3 adsorption sites [21]. Additionally, the efficiency of Au deposition method diminishes by gradually increasing Au content to 5 wt.%. From this point, Au loaded photocatalysts will be named with their actual amount based on EDX measurments, 0.64 for 1 wt.%, 1.18 for 3 wt.% and 1.82% for 5 wt.%.
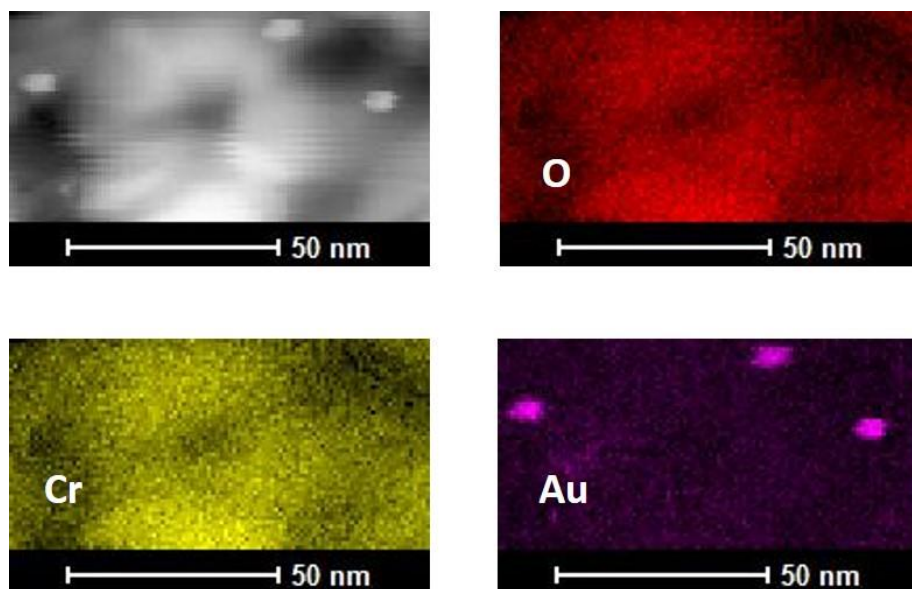
Figure 5.6. EDX elemental mapping of 3 wt.% Au/Cr$_2$O$_3$ sample.

5.2.2   Evaluation of photocatalytic performance using batch reactor

5.2.2.1   Effect of Au loading on Cr$_2$O$_3$ microspheres

The photocatalytic activities of the as-synthesized Cr$_2$O$_3$ and Au/Cr$_2$O$_3$ photocatalysts were evaluated *via* photo-oxidation of benzyl alcohol under 532 nm of laser irradiation using batch reactor. Control experiments demonstrated no detectable conversion without a photocatalyst under irradiation. Fig. 5.7 shows the plots of benzaldehyde formed under dark and after 3 h of laser irradiation for pure Cr$_2$O$_3$ and the effect of Au loading (0.64-1.82 wt.%). Under dark conditions, benzaldehyde was barely formed while upon visible light irradiation the catalytic performance of all synthesized catalysts significantly enhanced. As shown in Fig. 5.7, under light irradiation, 10.1 μmol benzaldehyde were formed using bare Cr$_2$O$_3$ as a photocatalyst, achieving 21.2% conversion of benzyl alcohol with an 88.2%, benzaldehyde selectivity (Fig. 5.8).
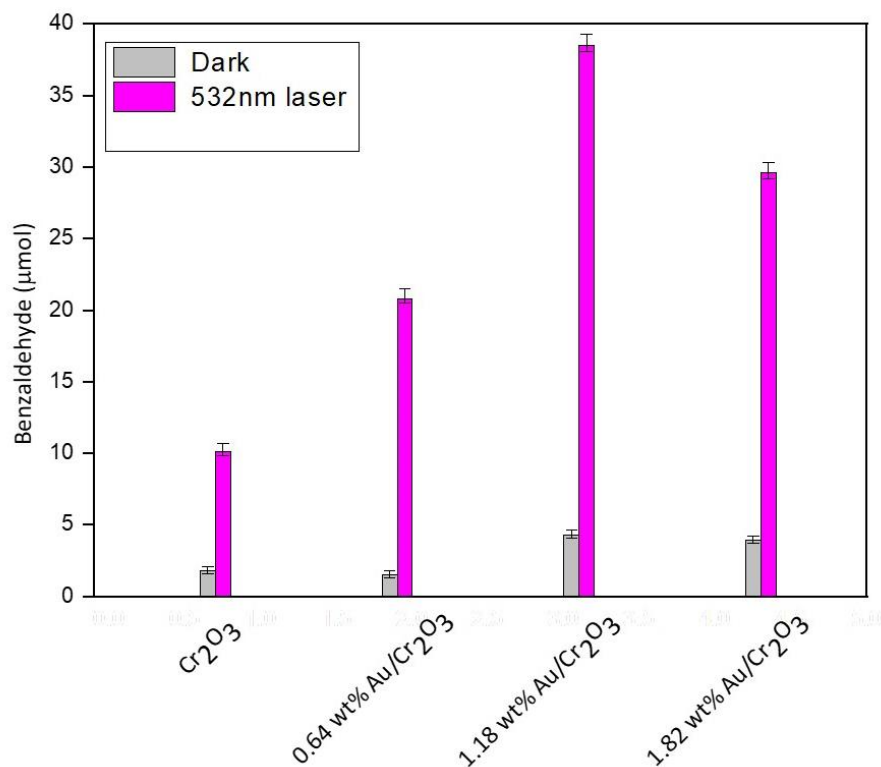
Figure 5.7. Amount of benzaldehyde produced during oxidation of benzyl alcohol in the dark and after 3 hours of 532 nm laser irradiation in the presence of 5 mg of catalyst and toluene as solvent under batch conditions.

The deposition of Au NPs onto Cr_2O_3 microspheres significantly enhanced benzaldehyde production with high selectivity. Among the supported Au photocatalysts, 1.18 wt.% Au/Cr_2O_3 produced the highest amount of benzaldehyde (38.5 μmol) with a selectivity 98.3%, which is 3.8 times higher compared to bare Cr_2O_3. Initially, the amount of produced benzaldehyde increased from 20.8 to 38.5 μmol by increasing Au content from 0.64 to 1.82 wt.%.
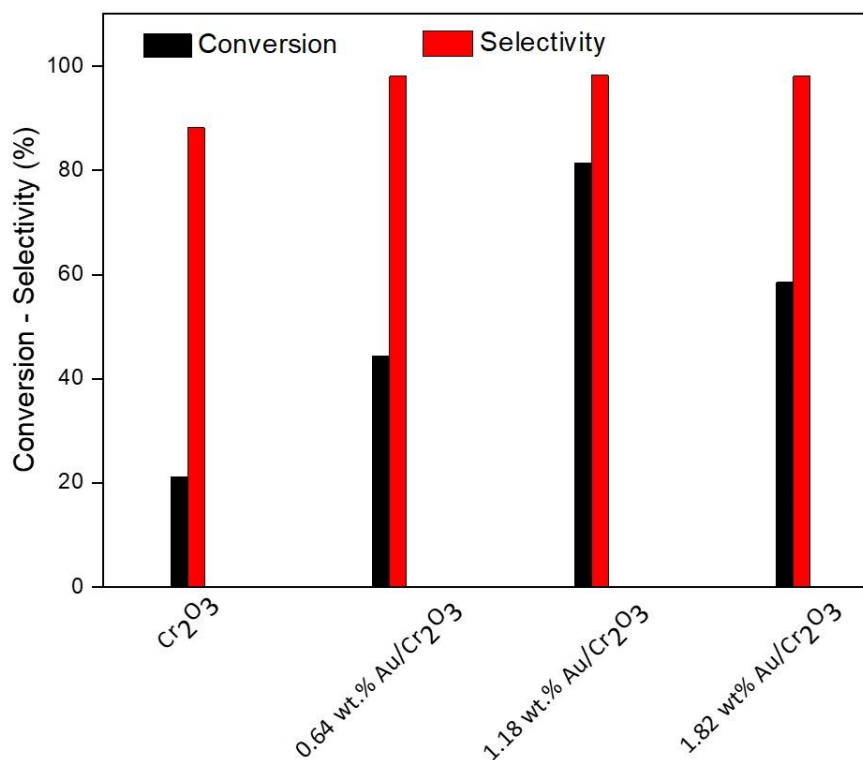
Figure 5.8. Conversion of benzyl alcohol towards benzaldehyde and selectivity of benzaldehyde.

The enhanced photocatalytic performance over Au/Cr$_2$O$_3$ photocatalysts can be ascribed to: 1) the suppression of photogenerated charge carriers recombination in Cr$_2$O$_3$ due to the presence of Au NPs, prolonging the lifetime of the electrons participate in the photoreaction and 2) the plasmon induced electromagnetic field enhancement near the surface of Au NPs in the semiconductor, which increased the generation rate of the photoexcited electron holes at Cr$_2$O$_3$ [22]. Plasmon Resonance Energy Transfer (PRET) mechanism is utilised to interpret the enhanced photocatalytic reaction *via* the presence of an intense electric field near the metal [23]. Particularly, plasmon energy is transferred to the semiconductor through the intense electric field created near the metal by incident irradiation. As incident light is falling on the metal, generation of electron hole pairs near the surface of the semiconductor is promoted *via* the dipole-dipole interaction between the metal and the semiconductor. PRET can amplify the electric field in small well-defined locations, named as hot spots. Based on Fine Difference Time Domain (FDTD) simulation study, the electric field in the hot spots shows up to 1000-fold enhancement compared to the incident electric field on the semiconductor surface, resulting to 1000 times more electron-hole generation rate and photoabsorption compared to that under normal incident light [24]. According to the literature, the overlap of LSPR band of the metal with the band gap of the semiconductor and the light

source spectrum is required to initiate the PRET mechanism [25]. In this study, the overlap between the LSPR of Au NPs with the absorbance of Cr_2O_3 and the laser light spectrum, allows the PRET mechanism (Fig. 5.9).
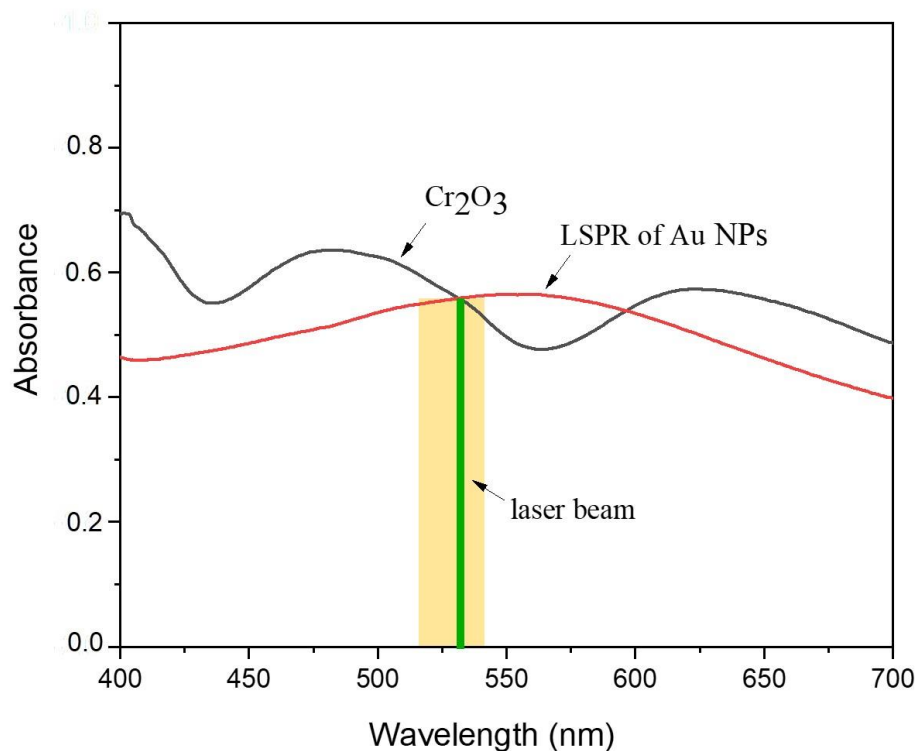
Figure 5.9. Overlap of LSPR Au NPs, Cr_2O_3 absorbance and laser light irradiation.

Nevertheless, when Au content was increased to 1.82 wt.%, a benzyl alcohol conversion of 58.5% was obtained, which was lower compared to the 1.18 wt.% of Au/Cr_2O_3 (Fig. 5.8). It can be concluded that the excessive Au loading (additional 0.64 wt.%) resulted in approximately 22% less production of benzaldehyde. Excessive Au NPs led to the formation of photogenerated charge carrier recombination centers that resulted in reduced photocatalytic activity. It should be also noted that a further increase of Au loading up to 1.82 wt.% led to an increased particle size of 10.8 nm, resulted in a decrease in the reaction rate. This decrease can be attributed to a reduction in the available metal-support sites where both metal and support are needed for the reaction to occur. [26-28]. This can be evidenced by the fact that the average size of Au NPs increases, as confirmed by TEM images (Fig. 5.5d) [29]. In order to further investigate the effect of Au loading, Au loadings 0.64 wt.% <1.18 wt.% <1.82 wt.%, were synthesized and their catalytic activity *via* benzyl alcohol oxidation was evaluated under the same reaction conditions and the results are presented in Fig. A1-A2, APPENDIX

A. The results presented a specific trend showing a decrease of benzaldehyde production for Au loadings >1.18 wt.%.

Based on the above results it can be summarized that an impressive photocatalytic activity in terms of benzyl alcohol conversion (81.4%) and benzaldehyde selectivity (98.3%) was achieved in a short reaction time (3 h) using a small amount of Au/Cr_2O_3 photocatalyst (1.18 wt.% Au loading). These findings allow a significant competitive performance with relevant research studies reported in the literature, where much longer reaction time (4-8 h) with higher amount of photocatalyst (20 mg) resulted in similar conversion [4, 30].

5.2.2.2 Kinetic study of photocatalytic oxidation of benzyl alcohol

Reaction kinetics of the photo-oxidation of benzyl alcohol were investigated to further evaluate the photocatalytic activity of the different samples. The kinetic profiles plotted in Fig. 5.10, were fitted to the pseudo-first-order kinetic model and the rate constant was estimated using the first order equation as follows:

$$ln\frac{C_0}{C_0 - x} = k \cdot t \qquad (5.1)$$

where C_0 is the initial concentration, x is the concentration of formed benzaldehyde at certain reaction time, t is the reaction time and k is the rate constant. The correlation coefficients R^2 were determined 0.958, 0.992, 0.998 and 0.998 for Cr_2O_3 and 0.64, 1.18 and 1.82 wt.% Au/ Cr_2O_3, respectively. As shown in Fig. 5.10, the reaction rate increased gradually over irradiation time for 3 h reaction. It should be noted that the presence of Au remarkably improved the reaction rate. Initially, a significant increase in the reaction rate was observed by increasing Au loading from 0.64 to 1.18 wt.%. However, a further increase to 1.82 wt.% Au loading led to a decrease in the reaction rate, implying an excessive loading.
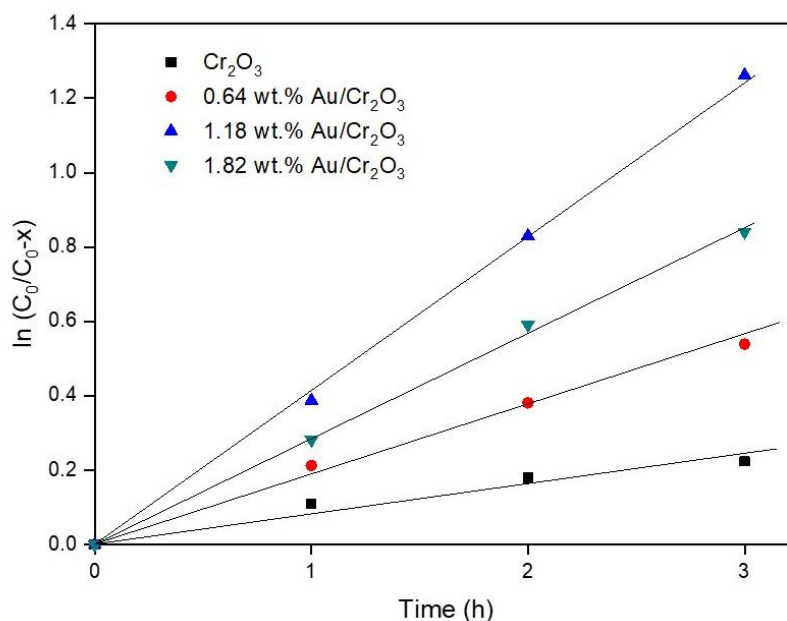
Figure 5.10. First-order kinetic plots of pure Cr_2O_3 and Au loaded samples.

It could be clearly observed that 1.18 wt.% Au/Cr_2O_3 photocatalyst possessed the highest reaction rate with a constant rate of 0.00701 min^{-1} which is 5.5 fold of bare Cr_2O_3 photocatalyst. Correspondingly, the reaction rate constant k (Fig. 5.11) of 5 wt.% Au/Cr_2O_3 was 0.00467 min^{-1}, following that of 1 wt.% (0.00299 min^{-1}) and lastly the pure Cr_2O_3 (0.00124 min^{-1}). Therefore, deposition of Au NPs on the surface of Cr_2O_3 microspheres can significantly improve benzyl alcohol oxidation rate to benzaldehyde, which can be attributed to the improved electron transfer processes and enhanced charge carriers separation.
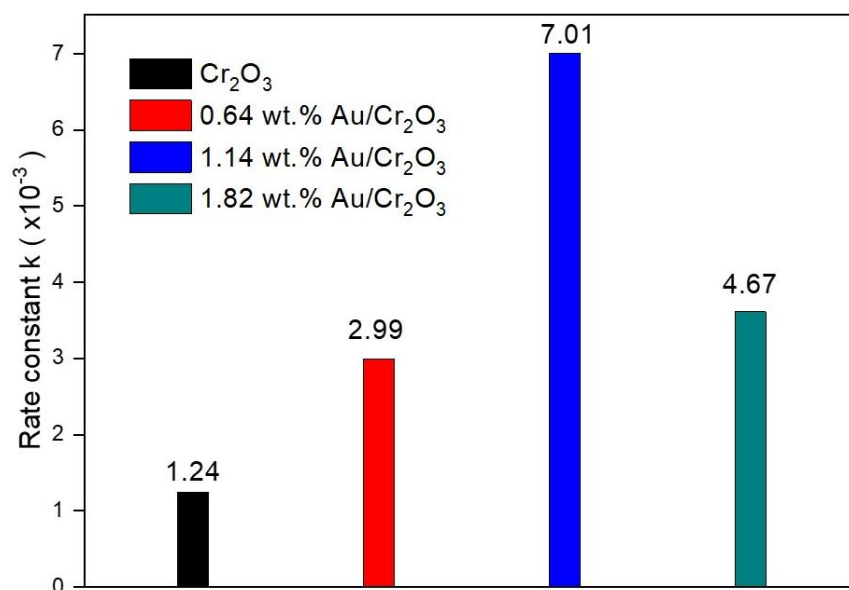
Figure 5.11. Constant rate k in the presence of pure Cr_2O_3 and Au loaded samples.

5.2.2.3 Effect of nature of the support

According to the literature, the support of plasmonic NPs can play a significant role in the activity of the photocatalyst as well as in the selectivity towards the products. To investigate the influence of the support, a 0.84 wt.% Au/TiO_2 catalyst was synthesized using deposition-precipitation method as described earlier in Chapter 3. The photocatalytic activity of 0.84 wt.% Au/TiO_2 was evaluated *via* oxidation of benzyl alcohol under the same experimental conditions of the Cr_2O_3-supported Au nanoparticles. TiO_2 was selected as support based on several studies that reported a high performance in photocatalytic reduction and oxidation reactions. Commercial P25-TiO_2 is a semiconductor with a band gap of 3.2 eV and has many advantages including high stability, low cost and non-toxicity.

As revealed from UV-Vis absorption spectra (Fig. 5.12a), 0.84 wt.% Au/TiO_2 nanoparticles exhibited absorption in the visible region with a plasmon peak located around 540 nm, revealing the presence of Au nanoparticles. EDX elemental mapping confirmed the homogeneous distribution of Au nanoparticles on the surface of TiO_2 support, while the nominal Au content was found to be 0.84% indicating that a complete Au deposition was not obtained (Fig. 5.12c).
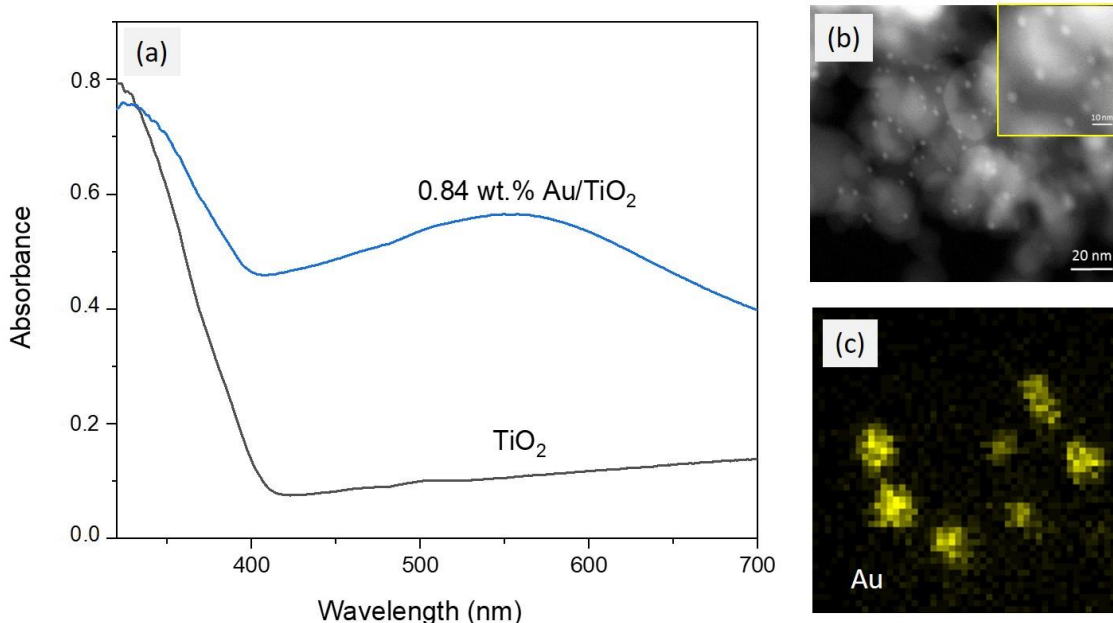
Figure 5.12. a) UV-Vis absorption spectra, b) TEM image and c) EDX mapping of 0.84 wt.% Au/TiO$_2$.

Fig. 5.13 shows conversion and selectivity of Au NPs supported on TiO$_2$ after 3 h of laser irradiation. Fig. 5.12 clearly shows that lower conversion was achieved using TiO$_2$ supported Au NPs (39.1%) compared with Cr$_2$O$_3$ supported Au NPs (81.4%) towards the photocatalytic oxidation of benzyl alcohol. The predominant reason for this trend is related to the fact that Cr$_2$O$_3$ microspheres not only play the role of support for Au NPs, but also actively participate in the photocatalytic oxidation of benzyl alcohol as it will be described below in the mechanism (section 5.2.2.6) due to their significant visible light absorption compared to TiO$_2$ NPs which absorb light only in the UV region. It should be noted that Cr$_2$O$_3$ has a band gap of 2.96 eV, calculated from the peak based on the absorption at the UV region and a second band gap of 2.3 eV corresponding to the significant absorption in the visible region while TiO$_2$ has a band gap of 3.2 eV. Another possible reason that could assist this phenomenon is related to the higher actual amount of Au NPs deposited on Cr$_2$O$_3$ microspheres (1.18 wt.%) compared to that deposited on TiO$_2$ NPs (0.84 wt.%).
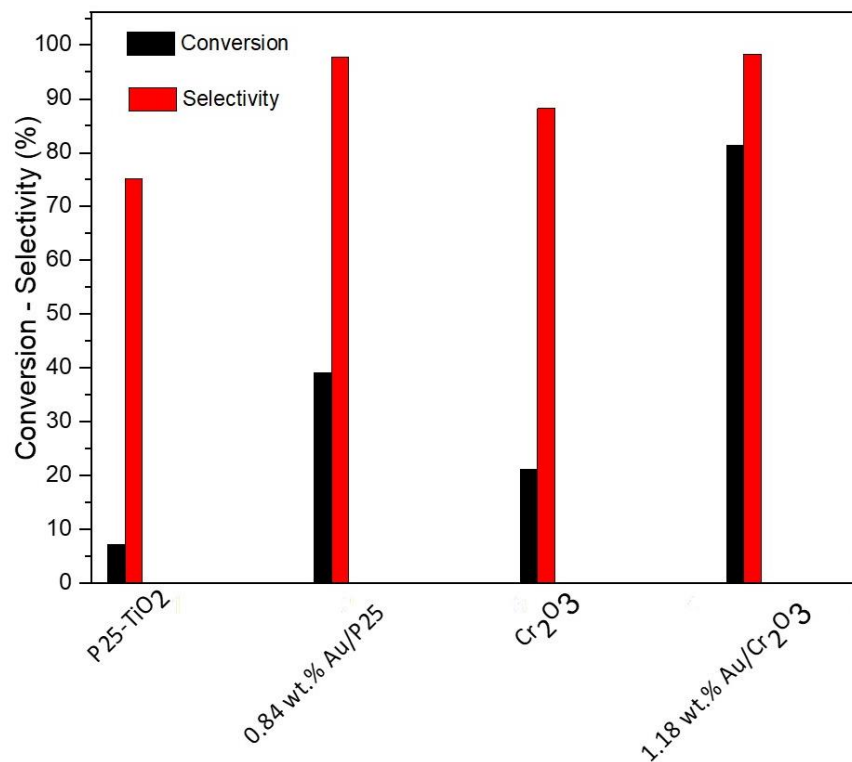
Figure 5.13. Conversion of benzyl alcohol towards benzaldehyde and selectivity of benzaldehyde.

5.2.2.4   Recyclability of photocatalysts

The recyclability of the photocatalyst is demonstrated using 1.18 wt.% Au/Cr_2O_3 for six reaction cycles (Fig. 5.14). The highest conversion (81.4%) and selectivity (98.3%) were achieved using the fresh catalyst. From the first to fifth cycle, conversions of 78.1%, 77.5%, 76.8%, 75.8% and 75.1% were obtained, respectively. For the final cycle, conversion and selectivity of greater than 74.5% and 96.1% respectively, were still obtained. From the above results, it can be concluded that the photocatalyst exhibited very good recyclability after the 6th cycle without significant loss of activity.
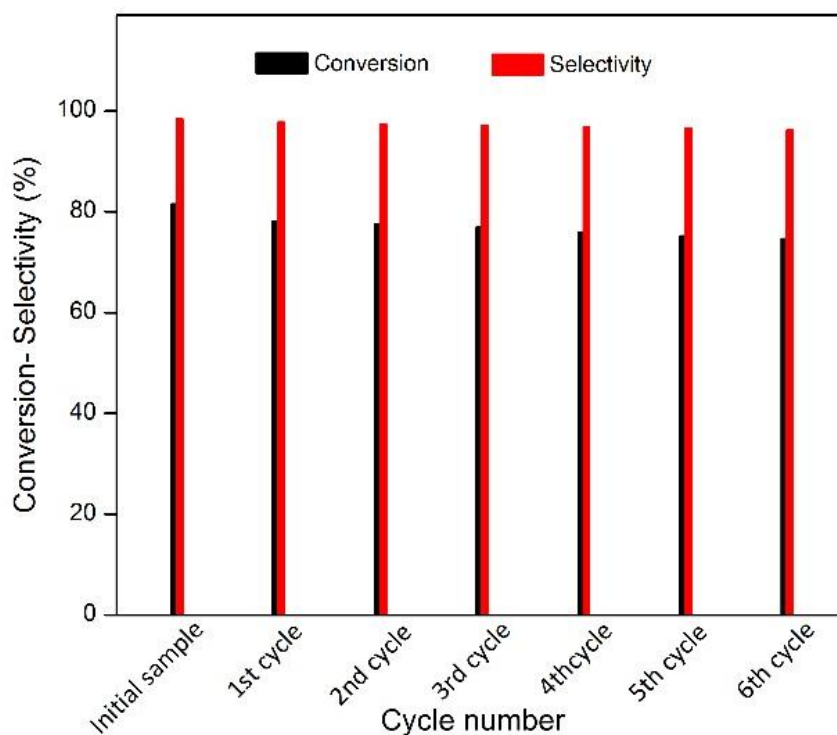
Figure 5.14. Recyclability test of 1.18 wt.% Au/Cr_2O_3 photocatalyst.

5.2.2.5   Effect of plasmonic heating on the photocatalytic activity

In order to investigate the role of photothermal effect on the photocatalytic process, the photocatalytic oxidation of benzyl alcohol was carried out under the same conditions as described above, but in the absence of water bath, which kept the temperature of the reaction constant at 21 ^{o}C. The temperature rise of the different suspensions irradiated by laser light was monitored using PicoLog thermocouple data logger (TC-08), as shown in Fig. 5.15. As it can be seen, the temperature of the photocatalytic system increases remarkably upon exposure to laser irradiation, while a steady state was observed after 25 min reaching a plateau due to equal heat dissipation to the environment. The significant temperature rise can be attributed to the strong photothermal effect of Au nanoparticles decorated on Cr_2O_3 microspheres. The temperature of Au/Cr_2O_3 suspension was significantly higher compared to pure Cr_2O_3, revealing a higher optical absorption of Au nanoparticles. It should be noted that Au loading influenced the temperature profile. Specifically, 1.18 wt.% Au/Cr_2O_3 presented the higher temperature rise (~ 17 ^{o}C) compared with that of 0.64 wt.% Au/Cr_2O_3 (~ 9 ^{o}C) and 1.82 wt.% Au/Cr_2O_3 (~ 12 ^{o}C).
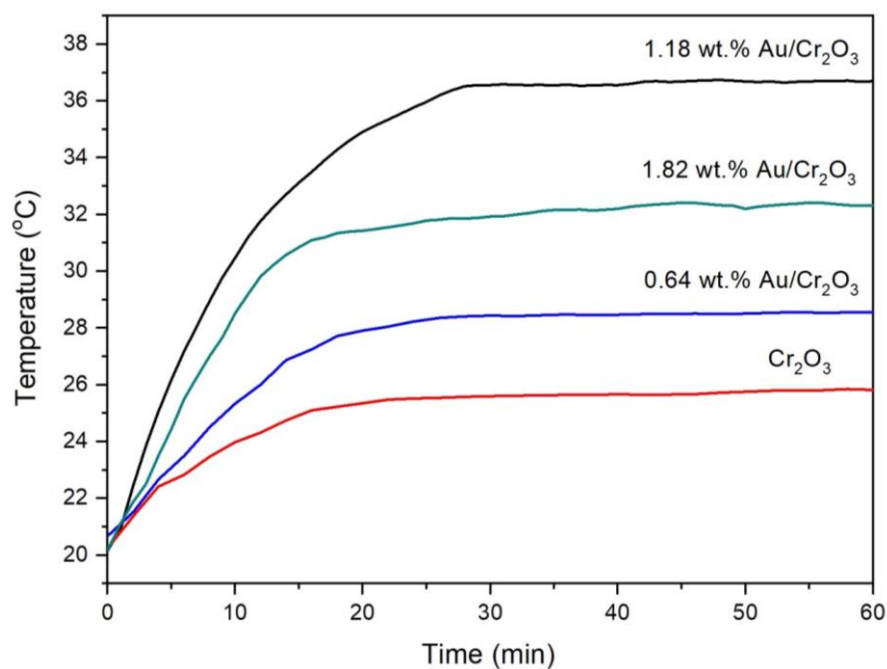
Figure 5.15. Temperature profile of pure Cr_2O_3 and Au/Cr_2O_3 toluene-based suspensions over time under batch conditions using laser irradiation.

For understanding the photothermal effect on the photocatalytic process, the reaction rate was plotted against time (Fig. 5.16) based on pseudo-first-order kinetic model and the constant rate k was calculated. With respect to the operating temperature, the contribution of the photothermal effect on the photoreaction is small at a temperature lower than 29 °C. Particularly, the values of reaction rate constant obtained for pure Cr_2O_3 (k=0.00133 min^{-1}) and for 0.64 wt.% Au/Cr_2O_3 (k=0.00326 min^{-1}) revealed an 7.2% and 9.1% rate enhancement respectively compared to that achieved when the reaction performed at a constant temperature of 21 °C. In contrast, when the operating temperature reached 32 °C, the photothermal-assisted reaction showed an enhanced constant rate (k=0.00526 min^{-1}) which provides a 11.2% rate enhancement compared to that obtained at room temperature. The rate enhancement was more significant when the temperature raised to 38 °C in case of 1.18 wt.% Au/Cr_2O_3 (k=0.00888 min^{-1}). The contribution of the photothermal effect of 1.18 wt.% Au/Cr_2O_3 on the total reaction was 26%. These findings reveal that the photothermal effect can assist significantly the photocatalytic performance.
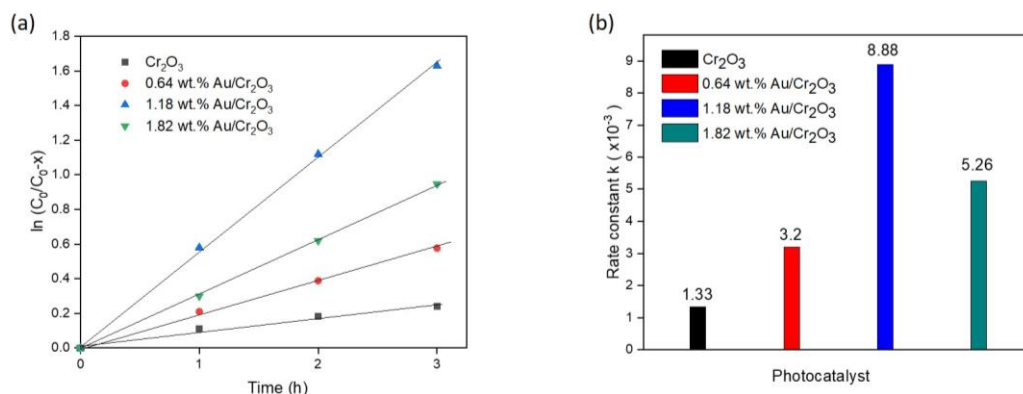
Figure 5.16. Photocatalytic oxidation of benzyl alcohol assisted by photothermal effect. (a) First-order kinetic plots of pure Cr_2O_3 and Au loaded samples and (b) constant rate k in the presence of pure Cr_2O_3 and Au loaded samples.

5.2.2.6 Photoelectrochemical test of Au/Cr$_2$O$_3$ microspheres

A series of photoelectrochemical (PEC) tests were performed to further evaluate the generation and transfer of photogenerated electrons for pure Cr_2O_3 and Au/Cr_2O_3 samples. J-t curves corresponding to light on and off measured at zero bias are shown in Fig. 5.17. Pure Cr_2O_3 produced a low photocurrent signal, whereas all Au loaded Cr_2O_3 samples exhibited improved photocurrent density, indicating an enhanced visible light harvesting and higher charge transfer efficiency in Au loaded Cr_2O_3 samples. The increase in the photocurrent response can be ascribed to the amplification of the electric field *via* SPR excitation of Au NPs [31]. 1.18 wt.% Au/Cr_2O_3 sample presented the highest photocurrent density, suggesting an effective electron transfer between Cr_2O_3 microspheres and Au NPs. This demonstrates that 1.18 wt.% Au/Cr_2O_3 photocatalyst has significantly efficient separation and prolongs the lifetime of photogenerated charge carriers upon light irradiation, which favors the photcatalytic activity. The photocurrent density of the tested samples is in agreement with the photocatalytic oxidation rate of the samples during the benzyl alcohol oxidation, indicating that SPR excitation of Au NPs can promote the charge carrier formation near the surface of Cr_2O_3 microspheres.
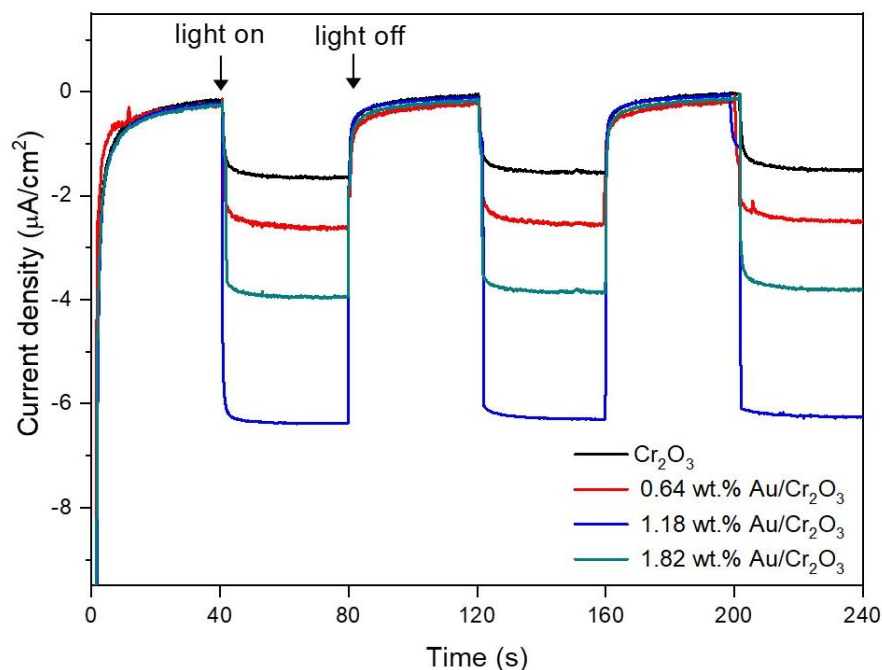
Figure 5.17. Photocurrent response of (a) Cr_2O_3, (b) 0.64, (c) 1.18 and (d) 1.82 wt.% Au/Cr_2O_3 in the presence of a solar simulator (Newport 92250A, AM 1.5G, 100 mW·cm-2). Photoelectrochemical measurements of all catalysts were carried out using an Autolab PGSTAT 302N electrochemical workstation in a three-electrode home-made cell, consisting of a sample-coated electrode as working electrode, Pt wire as counter electrode and Ag/AgCl (KCl 1M) as reference electrode while 0.5 M Na_2SO_4 aqueous solution served as electrolyte, section 3.3.1.2.

5.2.2.7 Investigation of photo-oxidation mechanism

To gain insights into the reaction mechanism, controlled experiments were conducted to detect the main oxidative species for the photocatalytic oxidation of benzyl alcohol in the presence of 1.18 wt.% Au/Cr_2O_3 using different radical scavengers (Fig. 5.18). The presence of tert-butyl alcohol (TBA) had almost no significant effect in the reaction process, implying that $OH^{\cdot}$ were not the primary active species. However, upon adding AO, $AgNO_3$ and BQ scavengers the conversion decreased to 40.2%, 27.2% and 32.4%, respectively. Under air atmosphere, the conversion of benzyl alcohol was higher (61.5%) but still lower than that obtained using pure oxygen (81.4%), indicating that O_2 is a crucial oxidizing agent in the photo-oxidation process. These findings revealed that both $^{\cdot}O_2^{-}$ and h^{+} were the dominant active species in the photo-oxidation of benzyl alcohol into the corresponding aldehyde. Based on these results, it can be concluded that oxygen acts as a trap to capture photogenerated electrons, providing $^{\cdot}O_2^{-}$, which could suspend the charge carrier recombination and promote the oxidation of benzyl alcohol.
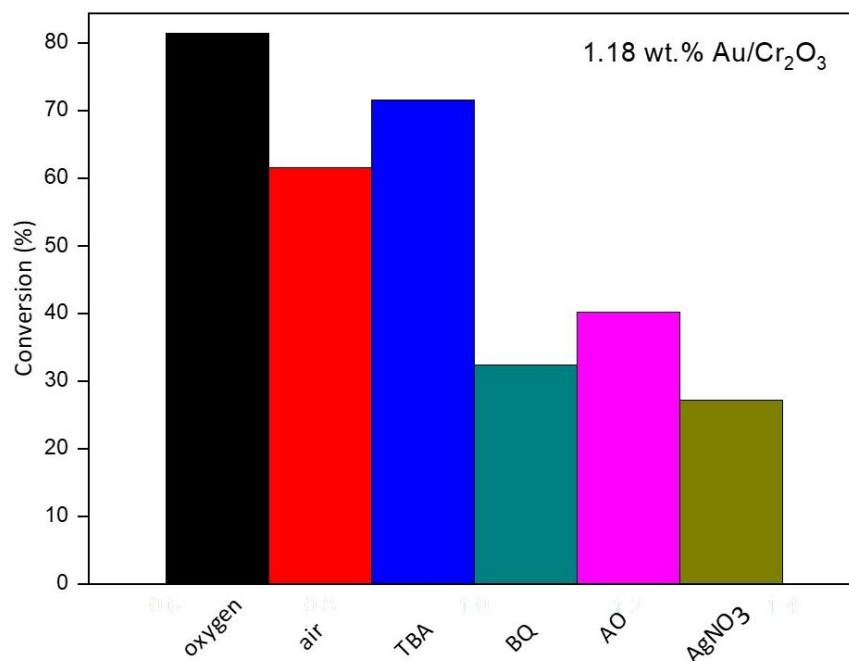
Figure 5.18. Photocatalytic oxidation process under O_2 and air atmosphere. Controlled experiments utilizing trapping agents: tert-butyl alcohol (TBA), 1,4-benzoquinone (BQ), ammonium oxalate (AO) and $AgNO_3$. Capture experiments were carried out using 1.21 wt.% Au/Cr_2O_3 sample.

Based on the above results, a mechanism for the photocatalytic oxidation of benzyl alcohol into benzaldehyde using Au/Cr_2O_3 is suggested (Fig. 5.19). Under visible light illumination, incident photons are absorbed by Cr_2O_3 microspheres (2.3 eV band gap corresponding to the absorption in the visible region) producing electron-hole pairs. Meanwhile, the local electric field enhancement around Au NPs and nearby the Cr_2O_3 microspheres, caused by excitation of Au NPs, promotes the electron-hole pair formation on Cr_2O_3 surface with higher rate compared to normal incident light. Subsequently, electrons migrate from the conduction band of Cr_2O_3 to Au across the Schottky barrier. The oxygen molecules function as a trap to capture the electrons on Au NPs, providing superoxide radical species ($^{\cdot}O_2^{-}$) [Eq. 5.2], which could suspend the charge carrier recombination and promote the oxidation of benzyl alcohol [4, 32]. Meanwhile, the holes on the surface of Cr_2O_3 contributed to the activation of aromatic alcohol following the pathway in Eq. 5.3. Then, $^{\cdot}O_2^{-}$ radicals could in turn trap two protons from the activated aromatic alcohol adsorbed at the neighbor sites to produce benzaldehyde [Eq 5.4]. It should be noted here that in the case of photothermal-assisted photocatalytic process, plasmonic NPs act as photothermal conversion medium and photocatalysts simultaneously. During the photothermal process, metal nanoparticles convert the absorbed photons to thermal energy, which is then transferred to surrounded medium, increasing the temperature. In turn, the increased temperature of plasmonic

103

NPs promotes carriers mobility, enabling carriers in the particles to be transferred faster at higher temperatures.

$$O_2 \xrightarrow{e^-} \cdot O_2^- \tag{5.2}$$

$$Ph - CH_2 - OH \xrightarrow{h^+} Ph - \overset{+\cdot}{C}H_2 - OH \tag{5.3}$$

$$Ph - \overset{+\cdot}{C}H_2 - OH \xrightarrow{\cdot O_2^-} Ph - CH = O + H_2O_2 \tag{5.4}$$
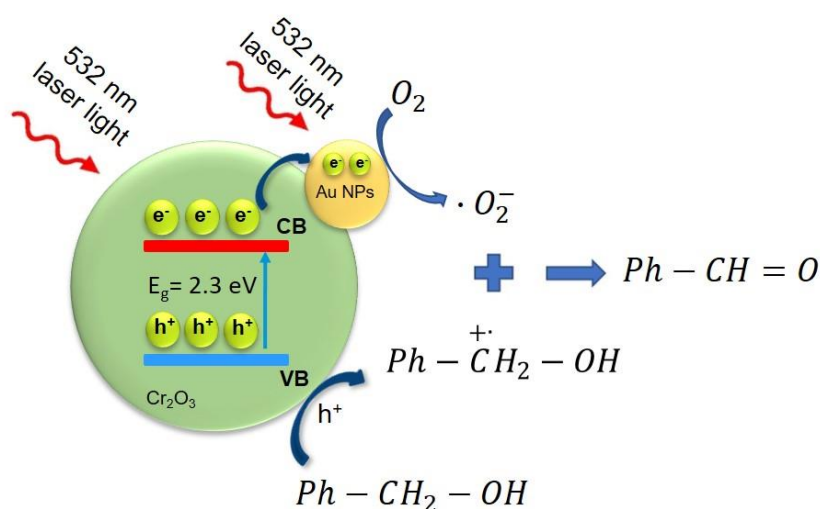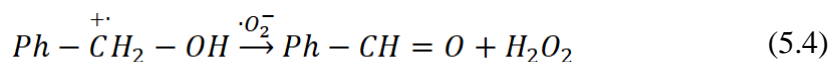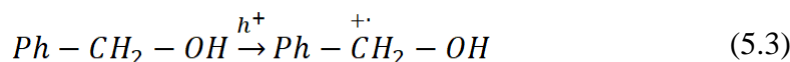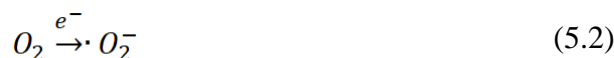
Figure 5.19. Proposed mechanism for formation of benzaldehyde from benzyl alcohol over Au/Cr$_2$O$_3$ under 532 nm laser irradiation.

5.3   Conclusions

The work outlined in this Chapter met the objective set in the thesis by showing that Au/Cr$_2$O$_3$ microspheres were used as efficient photocatalysts for the selective oxidation of benzyl alcohol to benzaldehyde, achieving high benzyl alcohol conversion with high benzaldehyde selectivity. A facile DP method has been applied to deposit Au NPs onto the surface of the hydrothermally-synthesized Cr$_2$O$_3$ microspheres. Au/Cr$_2$O$_3$ photocatalysts showed a remarkably absorption in the visible region, matching with the wavelength of laser employed as light source. It can be concluded that all Au loaded photocatalysts exhibited improved photocatalytic performance in benzyl alcohol photo-oxidation compared to pure Cr$_2$O$_3$. The enhanced photocatalytic activity can be ascribed to the improved formation rate of photogenerated charge carriers near the surface of Cr$_2$O$_3$ induced by LSPR of Au NPs and the efficient separation of photogenerated

electron hole pairs when Cr_2O_3 is decorated with Au NPs. Additionally, the effect of Au loading on the photocatalytic performance was investigated. It was confirmed that Au loading is very important to optimize yield towards benzaldehyde. From the tested samples, 1.18 wt.% Au/Cr_2O_3 achieved the highest benzyl alcohol conversion (81.4%) with benzaldehyde selectivity (98.3%) after 3 h under monochromatic laser irradiation (532 nm). However, a further increase of Au content to 1.82 wt.% led to a decrease in the reaction rate, indicating an excessive Au loading. The mechanistic studies of benzyl alcohol reaction indicated that the presence of O_2 is of crucial importance for the photo-oxidation reaction process. Finally, the role of photothermal effect on photocatalytic oxidation of benzyl alcohol was investigated and the results revealed an oxidation rate enhancement of 26% using 1.18 wt% Au/Cr_2O_3 photocatalyst.

The successful application of monometallic Au nanoparticles decorated on Cr_2O_3 microspheres for the photo-oxidation of benzyl alcohol to benzaldehyde inspired the work in Chapter 6 by investigating the effect of incorporating a second metal like Ag and particularly the significance of Ag/Au ratio.

5.4 References

[1] A.S. Sharma, H. Kaur, D. Shah, Selective oxidation of alcohols by supported gold nanoparticles: recent advances, RSC Advances, 6 (2016) 28688-28727.

[2] C. Wang, D. Astruc, Nanogold plasmonic photocatalysis for organic synthesis and clean energy conversion, Chemical Society Reviews, 43 (2014) 7188-7216.

[3] S. Linic, P. Christopher, D.B. Ingram, Plasmonic-metal nanostructures for efficient conversion of solar to chemical energy, Nature Materials, 10 (2011) 911-921.

[4] D. Tsukamoto, Y. Shiraishi, Y. Sugano, S. Ichikawa, S. Tanaka, T. Hirai, Gold Nanoparticles Located at the Interface of Anatase/Rutile TiO_2 Particles as Active Plasmonic Photocatalysts for Aerobic Oxidation, Journal of the American Chemical Society, 134 (2012) 6309-6315.

[5] X. Tao, L. Shao, R. Wang, H. Xiang, B. Li, Synthesis of BiVO4 nanoflakes decorated with AuPd nanoparticles as selective oxidation photocatalysts, Journal of Colloid and Interface Science, 541 (2019) 300-311.

[6] H. Sun, L. Wang, D. Chu, Z. Ma, A. Wang, Synthesis of porous Cr_2O_3 hollow microspheres *via* a facile template-free approach, Materials Letters, 140 (2015) 35-38.

[7] S.A. Makhlouf, Z.H. Bakr, H. Al-Attar, M.S. Moustafa, Structural, morphological and electrical properties of Cr_2O_3 nanoparticles, Materials Science and Engineering: B, 178 (2013) 337-343.

[8] Z. Hu, M. Xu, Z. Shen, J.C. Yu, A nanostructured chromium(iii) oxide/tungsten(vi) oxide p–n junction photoanode toward enhanced efficiency for water oxidation, Journal of Materials Chemistry A, 3 (2015) 14046-14053.

[9] G. Bai, H. Dai, Y. Liu, K. Ji, X. Li, S. Xie, Preparation and catalytic performance of cylinder- and cake-like Cr_2O_3 for toluene combustion, Catalysis Communications, 36 (2013) 43-47.

[10] H. Zhou, S. Xu, D. Zhang, S. Chen, J. Deng, One step in situ synthesis of core–shell structured Cr_2O_3:P@fibrous-phosphorus hybrid composites with highly efficient full-spectrum-response photocatalytic activities, Nanoscale, 9 (2017) 3196-3205.

[11] J. Ding, J. Ming, D. Lu, W. Wu, M. Liu, X. Zhao, C. Li, M. Yang, P. Fang, Study of the enhanced visible-light-sensitive photocatalytic activity of Cr_2O_3-loaded titanate nanosheets for Cr(vi) degradation and H2 generation, Catalysis Science & Technology, 7 (2017) 2283-2297.

[12] K. Hayat, M.A. Gondal, M.M. Khaled, S. Ahmed, Kinetic study of laser-induced photocatalytic degradation of dye (alizarin yellow) from wastewater using

nanostructured ZnO, Journal of Environmental Science and Health, Part A, 45 (2010) 1413-1420.

[13] H. Huang, M. Sivayoganathan, W.W. Duley, Y. Zhou, Efficient localized heating of silver nanoparticles by low-fluence femtosecond laser pulses, Applied Surface Science, 331 (2015) 392-398.

[14] X. Liu, Y. Yang, X. Shi, K. Li, Fast photocatalytic degradation of methylene blue dye using a low-power diode laser, Journal of Hazardous Materials, 283 (2015) 267-275.

[15] J. Huang, M. Zhang, J. Wang, X. Hu, R. Luque, F.L.Y. Lam, A comprehensive study on the effect of preparation methods for Au-core@shell silica materials in room temperature oxidative amide formation, Journal of Materials Chemistry A, 3 (2015) 789-796.

[16] C. Wang, O. Ranasingha, S. Natesakhawat, P.R. Ohodnicki, M. Andio, J.P. Lewis, C. Matranga, Visible light plasmonic heating of Au-ZnO for the catalytic reduction of CO_2, Nanoscale, 5 (2013) 6968-6974.

[17] C.J.B. Alejo, C. Fasciani, M. Grenier, J.C. Netto-Ferreira, J.C. Scaiano, Reduction of resazurin to resorufin catalyzed by gold nanoparticles: dramatic reaction acceleration by laser or LED plasmon excitation, Catalysis Science & Technology, 1 (2011) 1506-1511.

[18] S. Shaukat, M. Khaleeq-ur-Rahman, U. Ilyas, S. Naseem, I.M. Dildar, A. Latif, R.S. Rawat, Tailoring of optical band gap and electrical conductivity in a-axis oriented Ni doped Chromium Oxide thin films, Ceramics International, 44 (2018) 11187-11195.

[19] J. Lu, H. Wang, D. Peng, T. Chen, S. Dong, Y. Chang, Synthesis and properties of Au/ZnO nanorods as a plasmonic photocatalyst, Physica E: Low-dimensional Systems and Nanostructures, 78 (2016) 41-48.

[20] D.B. Ingram, P. Christopher, J.L. Bauer, S. Linic, Predictive Model for the Design of Plasmonic Metal/Semiconductor Composite Photocatalysts, ACS Catalysis, 1 (2011) 1441-1447.

[21] L. Collado, A. Reynal, J.M. Coronado, D.P. Serrano, J.R. Durrant, V.A. de la Peña O'Shea, Effect of Au surface plasmon nanoparticles on the selective CO_2 photoreduction to CH_4, Applied Catalysis B: Environmental, 178 (2015) 177-185.

[22] S.K. Cushing, J. Li, F. Meng, T.R. Senty, S. Suri, M. Zhi, M. Li, A.D. Bristow, N. Wu, Photocatalytic Activity Enhanced by Plasmonic Resonant Energy Transfer from Metal to Semiconductor, Journal of the American Chemical Society, 134 (2012) 15033-15041.

[23] M.R. Khan, T.W. Chuan, A. Yousuf, M.N.K. Chowdhury, C.K. Cheng, Schottky barrier and surface plasmonic resonance phenomena towards the photocatalytic reaction: study of their mechanisms to enhance photocatalytic activity, Catalysis Science & Technology, 5 (2015) 2522-2531.

[24] W. Hou, Z. Liu, P. Pavaskar, W.H. Hung, S.B. Cronin, Plasmonic enhancement of photocatalytic decomposition of methyl orange under visible light, Journal of Catalysis, 277 (2011) 149-153.

[25] N. Zhou, V. Lopez-Puente, Q. Wang, L. Polavarapu, I. Pastoriza-Santos, Q.-H. Xu, Plasmon-enhanced light harvesting: applications in enhanced photocatalysis, photodynamic therapy and photovoltaics, RSC Advances, 5 (2015) 29076-29097.

[26] V. Jovic, W.-T. Chen, D. Sun-Waterhouse, M.G. Blackford, H. Idriss, G.I.N. Waterhouse, Effect of gold loading and TiO_2 support composition on the activity of Au/TiO_2 photocatalysts for H_2 production from ethanol–water mixtures, Journal of Catalysis, 305 (2013) 307-317.

[27] J. Fang, S.-W. Cao, Z. Wang, M.M. Shahjamali, S.C.J. Loo, J. Barber, C. Xue, Mesoporous plasmonic Au–TiO2 nanocomposites for efficient visible-light-driven photocatalytic water reduction, International Journal of Hydrogen Energy, 37 (2012) 17853-17861.

[28] P. Wongwisate, S. Chavadej, E. Gulari, T. Sreethawong, P. Rangsunvigit, Effects of monometallic and bimetallic Au–Ag supported on sol–gel TiO_2 on photocatalytic degradation of 4-chlorophenol and its intermediates, Desalination, 272 (2011) 154-163.

[29] B. Cojocaru, Ş. Neaţu, E. Sacaliuc-Pârvulescu, F. Lévy, V.I. Pârvulescu, H. Garcia, Influence of gold particle size on the photocatalytic activity for acetone oxidation of Au/TiO_2 catalysts prepared by dc-magnetron sputtering, Applied Catalysis B: Environmental, 107 (2011) 140-149.

[30] X. Wang, D. Baiyila, X. Li, Macroporous TiO_2 encapsulated Au@Pd bimetal nanoparticles for the photocatalytic oxidation of alcohols in water under visible-light, RSC Advances, 6 (2016) 107233-107238.

[31] S. Mubeen, G. Hernandez-Sosa, D. Moses, J. Lee, M. Moskovits, Plasmonic Photosensitization of a Wide Band Gap Semiconductor: Converting Plasmons to Charge Carriers, Nano Letters, 11 (2011) 5548-5552.

[32] P. Christopher, H. Xin, A. Marimuthu, S. Linic, Singular characteristics and unique chemical bond activation mechanisms of photocatalytic reactions on plasmonic nanostructures, Nature Materials, 11 (2012) 1044-1050.

Chapter 6 - Continuous Flow Photocatalytic Synthesis of Benzaldehyde with Ag-Au Bimetallic Nanoparticles Supported on Cr_2O_3 Microspheres

6.1 Introduction

In Chapter 5, the successful application of monometallic Au nanoparticles decorated on Cr_2O_3 microspheres for the photo-oxidation of benzyl alcohol to benzaldehyde was demonstrated. The anchoring of noble metals on semiconductors extends the light absorption to the visible region, promoting the formation of photoexcited electrons or plasmonic hot electrons and facilitates the separation of photoinduced charge carriers at the interface between metal and semiconductor [1]. As explained in Chapter 2, bimetallic NPs, composed of two different metal elements, show enhanced photocatalytic performance over their monometallic counterparts due to the synergistic effects between the metals [2, 3]. The synergistic effects could arise from the efficient charge transfer and interfacial collaboration by the two metals [4].

As discussed in section 2.5, Chapter 2, many studies have reported the loading of bimetallic NPs on semiconducting materials for the oxidation of aromatic alcohols. For example, Tao *et al.* reported a benzyl alcohol conversion of 71.8% with 99% benzaldehyde selectivity after 8 h irradiation in the presence of $Au/Pd/BiVO_4$, which is 6 times higher compared to that of pure $BiVO_4$ and 1.35 times that of monometallic $Pd/BiVO_4$, revealing the synergistic effect between the two metals [5]. Sahoo *et al.* reported the photocatalytic superiority of AuAg/Graphene oxide (GO)/ Layered double hydroxide (LDH) *via* oxidation of benzyl alcohol which presented 2.5 times higher performance (82.7% benzaldehyde yield and 90% selectivity) than GO/LDH after 3 h visible irradiation without any indication of activity loss after 5 cycles [2]. In another study, Wang and co-workers showed that the loading of bimetallic Au/Pd NPs on Bi_2WO_6 enhanced the photocatalytic performance, after 5 h irradiation, obtaining 80% benzyl alcohol conversion with 86% benzaldehyde selectivity [6]. According to the authors, the optimum Au/Pd ratio plays a significant role in the conversion efficiency of the photocatalytic oxidation of benzyl alcohol. Although many studies reported the photocatalytic oxidation of alcohols in the presence of noble metals, the conversion efficiency is still low in terms of yield and selectivity. It is imperative to explore advanced photocatalysts combined with noble metals to improve the efficiency of photocatalytic oxidation of benzyl alcohol. Chromium (III) oxide (Cr_2O_3), which is a p-

type semiconductor with absorption bands at UV region (380 nm) and Visible region (460 and 600 nm), with bandgap energy estimated using Kubelka-Munk function at 2.3 eV corresponding to the significant absorption in the visible region and a second band gap of 2.96 eV [7]. Cr_2O_3 microspheres decorated with bimetallic AuAg NPs has not been used as photocatalyst in the photocatalytic oxidation of aromatic compounds.

So far, the most common approaches for selective oxidation of aromatic alcohols are based on the utilization of batch reactors [8, 9]. While batch reactors are used in a wide variety of reactions due to their versatility, the long reacton times are major barrier for large scale applications. The slow reaction rates are attributed mainly to insufficient mass and photon transfer in the reaction system [10]. As described in section 2.4, Chapter 2, continuous flow reactors offer many advantages due to the enhanced mass and heat transfer while at the same time improve the safety and sustainability for fine chemicals and pharma industries [11, 12]. Flow reactors enable the synthesis of fine chemical and drugs with high yields at a very short time while solvent and energy waste can be decreased up to 90%. [13, 14].

The objective of Chapter 6 was to investigate the stability and activity of bimetallic Ag-Au NPs supported on Cr_2O_3 microspheres *via* photocatalytic oxidation of benzyl alcohol under batch and continuous flow conditions. Au and Ag nanoparticles were uniformly decorated on hydrothermally synthesized Cr_2O_3 microspheres by deposition precipitation and wet impregnation method respectively. The optical and physical properties of the as-prepared photocatalysts were characterized by SEM, TEM, EDX, DRS and XRD. Under batch conditions, the effect of different ratio of Ag/Au was explored, indicating the importance of optimized Ag/Au ratio on the performance of selective alcohol oxidation. In terms of continuous flow synthesis of benzaldehyde, the influence of flow rate, catalyst concentration and laser intensity on benzaldehyde production was evaluated. Finally, the photothermal effect of Ag and Au NPs on the reaction rate under continuous flow conditions was studied.

6.2 Results and discussion

6.2.1 Characterization of synthesized photocatalysts

The crystallinity and phase identification of the as-prepared photocatalysts was identified by XRD patterns (Fig. 6.1). As revealed from Fig. 6.1a, Cr_2O_3 showed a high crystallinity corresponding to the crystallographic phase of JCPDS: 38-1479. The diffraction peaks detected at $2\theta = 24.4°$, $33.7°$, $36.3°$, $41.5°$, $50.3°$, $54.9°$, $63.5°$ and 65.2 were assigned to (012), (104), (110), (113), (024), (116), (214), and (300) crystal planes

of Cr_2O_3, respectively [15]. After the deposition of noble metals, no characteristic diffraction peaks of Au or Ag were observed due to the low content and small particle size of the metal nanoparticles as confirmed from TEM images (Fig. 6.5).
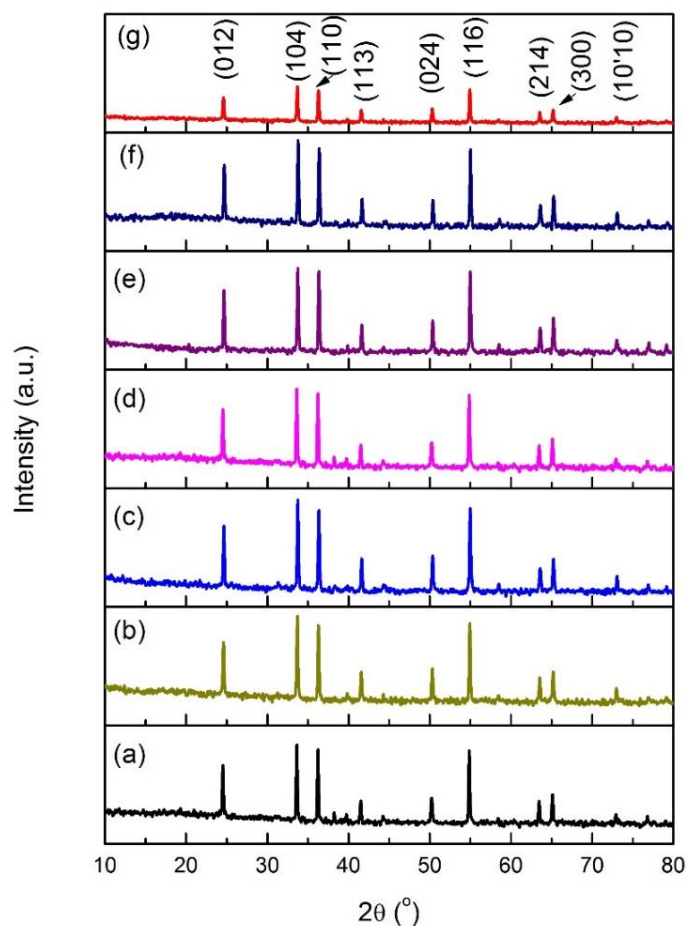
Figure 6.1. XRD pattern of (a) crystallized Cr_2O_3, (b) $1Ag/Cr_2O_3$, (c) $3Au/Cr_2O_3$, (d) $0.5Ag$-$3Au/Cr_2O_3$, (e) $1Ag$-$3Au/Cr_2O_3$, (f) $2Ag$-$3Au/Cr_2O_3$ and (g) $3Ag$-$3Au/Cr_2O_3$.

The UV-Vis diffuse reflectance spectra of bare Cr_2O_3 microspheres, monometallic Au, Ag and bimetallic Ag-Au/Cr_2O_3 photocatalysts are shown in Fig. 6.2. Cr_2O_3 microspheres exhibited two defined absorption peaks in the visible region located at 460 and 600 nm, which were consistent with these reported in the literature [16]. The band gap energy of Cr_2O_3 was calculated at 2.3 eV corresponding to the significant absorption in the visible region and a second band gap of 2.96 eV [17]. Monometallic Au and Ag NPs decorated on Cr_2O_3 exhibited a more intense absorption especially in the wavelength range of 500-600 nm and 430-530 nm respectively, which can be ascribed to the surface plasmon resonance of metal NPs [18, 19]. In the case of

bimetallic NPs, 0.5Ag-3Au/Cr_2O_3 microspheres have an enhanced absorption between 530-600 nm with a SPR peak shifted to 591 nm, which is close to the peak of 3Au/Cr_2O_3. By increasing Ag content in Ag/Au ratio, the SPR peak blue-shifted towards that of Ag NPs. Particularly, the peak shifted to 583, 572 and 559 nm for 1Ag-3Au/Cr_2O_3, 2Ag-3Au/Cr_2O_3 and 3Ag-3Au/Cr_2O_3 respectively [20, 21]. The sample slightly changed colour with different Ag/Au ratio, indicating the successful deposition of Au and Ag. It can be concluded that the SPR peak of Ag-Au NPs can be altered by changing the content of Au and Ag NPs.
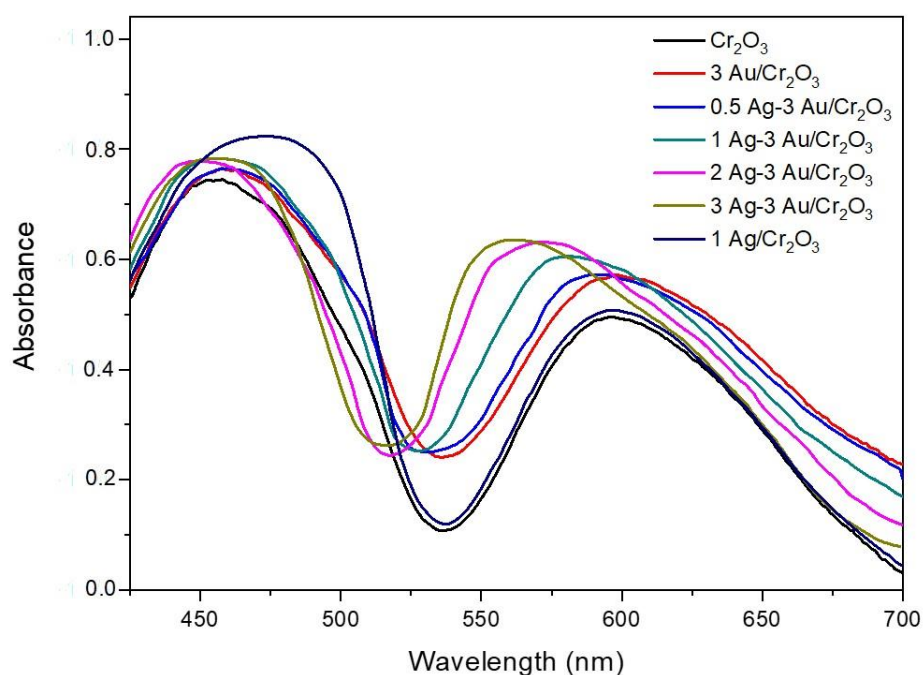
Figure 6.2. Diffuse reflectance spectra of Cr_2O_3, 3 Au/Cr_2O_3, 0.5Ag-3Au/Cr_2O_3, 1Ag-3Au/Cr_2O_3, 2Ag-3Au/Cr_2O_3, 3Ag-3Au/Cr_2O_3 and 1Ag/Cr_2O_3.

The morphology of as-synthesized Cr_2O_3 and bimetallic Au and Ag NPs with different molar ratio was studied using SEM and TEM. Fig. 6.3a,b show SEM and TEM images of hydrothermally synthesized raspberry-like structured Cr_2O_3 microspheres with average diameter of 500 nm. Bimetallic nanoparticles appear to have similar morphologies compared to that of monometallic Ag and Au. Particularly, Ag and Au NPs with a spherical shape were homogeneously distributed on the surface of Cr_2O_3 microspheres (Fig. 6.3c-h). By increasing Ag content from 0.5 to 3 wt.%, a slight increase of Ag particle size (3.3 – 5.8 nm) was observed.
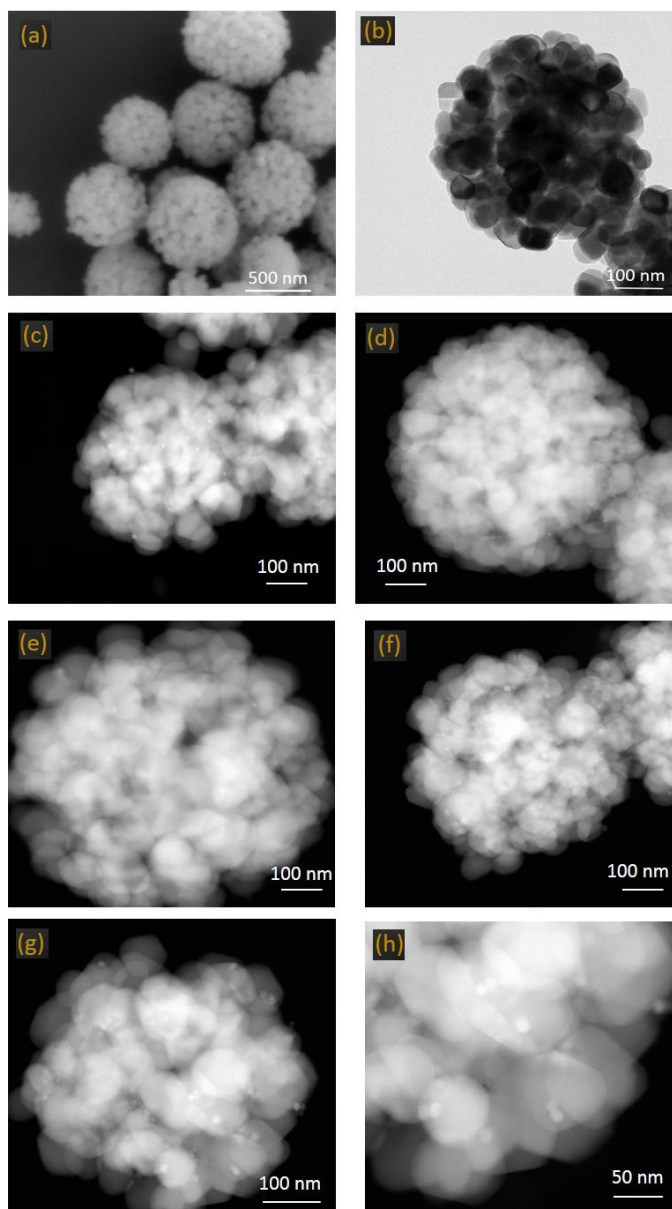
Figure 6.3. (a) SEM and (b) TEM images of Cr_2O_3 microspheres. STEM images of (c) $1Ag/Cr_2O_3$, (d) $3Au/Cr_2O_3$, (e) $0.5Ag-3Au/Cr_2O_3$, (f) $1Ag-3Au/Cr_2O_3$, (g) $2Ag-3Au/Cr_2O_3$ and (h) $3Ag-3Au/Cr_2O_3$.

EDX elemental mapping confirmed the uniform distribution of the elements Au, Ag, Cr and O. (Fig. 6.4). Au and Ag NPs decorated on Cr_2O_3 microspheres were clearly identified in the mapping data. EDX analysis showed that the actual Au content for 3 wt.% was 1.21%, which can be attributed to the high pH of the solution during the deposition-precipitation method, resulting in limited number of Cr_2O_3 adsorption sites [22]. The nominal and actual loading of Au and Ag NPs are listed in Table 6.1. From this point, Au-Ag loaded photocatalysts will be named with their actual amount based on EDX measurments, 0.34Ag-1.21Au for 0.5% Ag – 3% Au wt.%, 0.78Ag-1.22Au for 1% Ag – 3% Au, 1.48Ag-1.18Au for 2% Ag – 3% Au, 2.24Ag-1.22Au for 3% Ag – 3% Au, 0.82Ag for 1 wt.% Ag and 1.18Au for 3 wt.% Au.
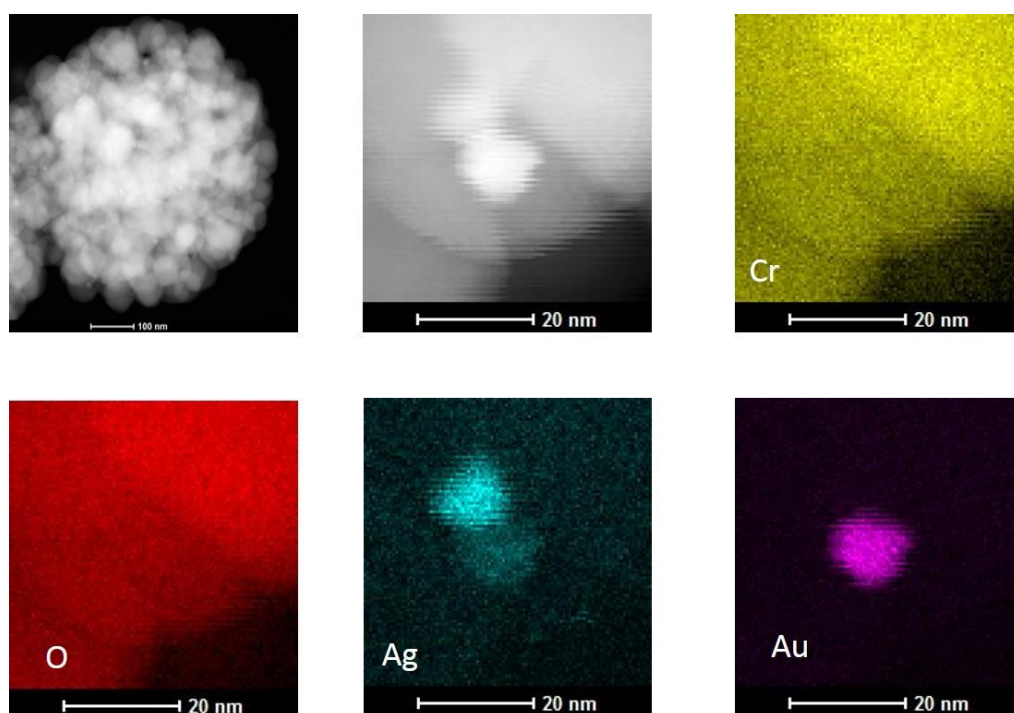
Figure 6.4. EDX elemental mapping of 0.5Ag-3Au/Cr_2O_3 photocatalyst.

Table 6.1. Nominal and actual loading of Ag and Au NPs estimated using EDX.

Nominal loading of photocatalysts	Actual Ag (wt.%)	Actual Au (wt.%)
0.5% Ag – 3% Au	0.34	1.21
1% Ag – 3% Au	0.78	1.28
2% Ag – 3% Au	1.48	1.18
3% Ag – 3% Au	2.24	1.22
1% Ag	0.82	-
3% Au	-	1.18

6.2.2 Batch experiments

6.2.2.1 Effect of Ag-Au ratio

The photocatalytic performance of pure Cr_2O_3, mono- and bi- metallic Ag-Au/Cr_2O_3 photocatalysts was investigated *via* the photocatalytic oxidation of benzyl alcohol. The conversion of benzyl alcohol and produced benzaldehyde after 3 h reaction under 532 nm laser irradiation are illustrated in Fig. 6.5-6.6. By introducing plasmonic metals, the

photocatalytic performance towards selective oxidation of benzyl alcohol was promoted.
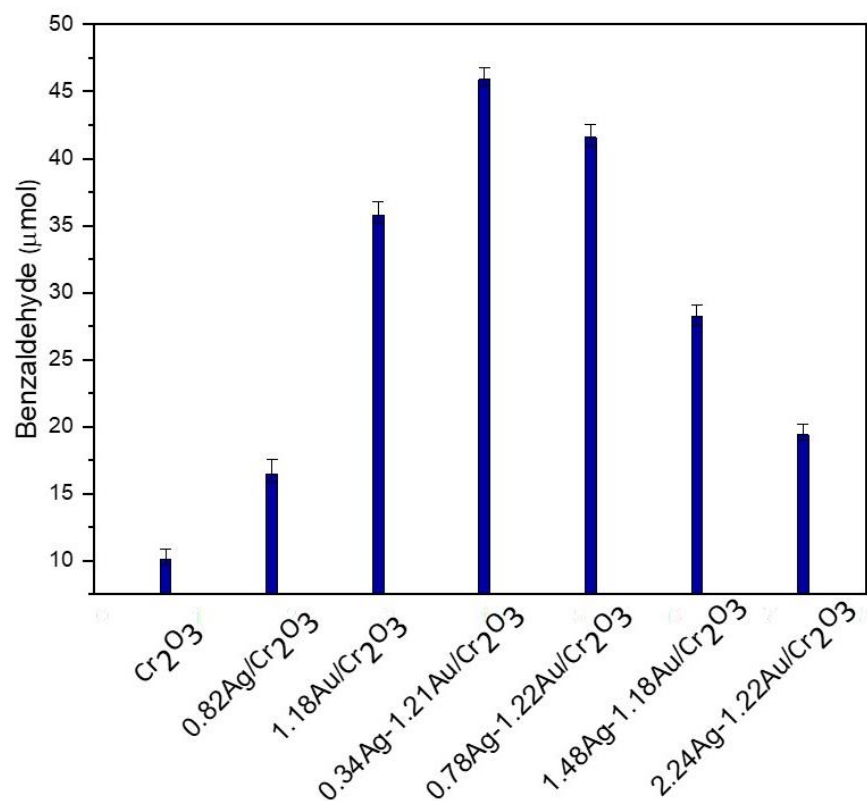
Figure 6.5. Amount of benzaldehyde produced during photo-oxidation of benzyl alcohol.

Monometallic Au or Ag NPs decorated on Cr_2O_3 exhibited an enhanced conversion (81.4 % and 39.1 % respectively) along with high selectivity of formed benzaldehyde compared to pure Cr_2O_3 microspheres (21.2%). The improved photo-oxidation of benzyl alcohol can be attributed to the increased generation rate of the photoexcited electron holes at Cr_2O_3 and the suppression of photogenerated charge carriers recombination due to the presence of metal [23-25]. It should be noted that 1.18 wt.% Au loading (Fig. 5.7-5.8, Chapter 5) and 1 wt.% Ag loading (Fig. A3-A4, APPENDIX A) were selected as the samples with the highest photocatalytic activity for comparison with bimetallic photocatalysts with different Ag-Au ratio.
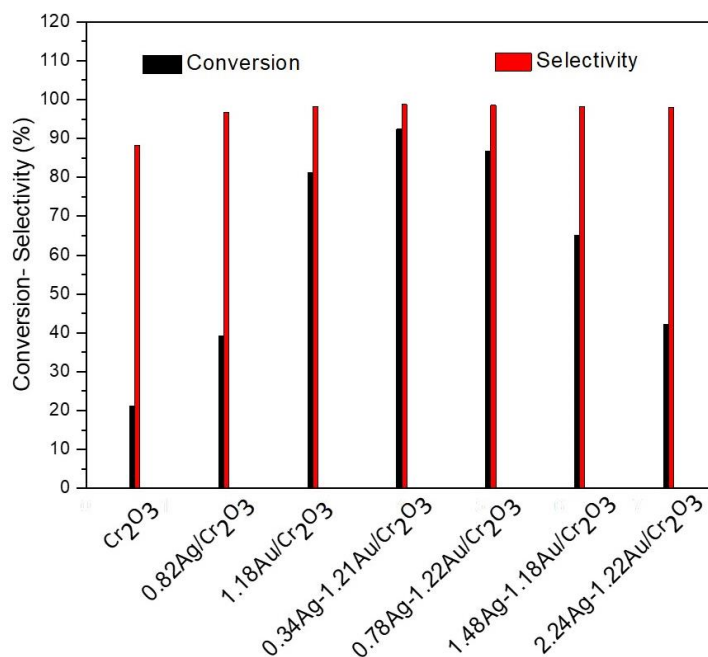
Figure 6.6. Conversion of benzyl alcohol to benzaldehyde and selectivity of benzaldehyde.

Based on the highest benzyl alcohol conversion achieved using 1.18 wt.% Au/Cr_2O_3 as demonstrated in Chapter 5, herein the effect of bimetallic AuAg NPs was explored using different Ag/Au ratio by keeping constant Au content to 1.18 wt.%. Fig. 6.6 shows that a significant photocatalytic performance for all bimetallic $Ag-Au/Cr_2O_3$ was obtained. The results revealed that Ag/Au ratio plays an important role in the photocatalytic activity. $0.34Ag-1.21Au/Cr_2O_3$ photocatalyst showed the highest light-enhanced activity by converting 92.4% of benzyl alcohol, producing 45.7 μmol of benzaldehyde with 98.8 % selectivity, which is 4.5 times that of pure Cr_2O_3 and 1.3 times of $1.18Au/Cr_2O_3$. The enhanced photocatalytic performance of bimetallic Ag-Au NPs can be attributed to the synergistic effect of Ag and Au, leading to efficient charge transfer and separation of the photogenerated electron-hole pairs between bimetallic NPs [26, 27]. TEM images (Fig. 6.3) evidently demonstrate that the AuAg NPs are spherical and uniformly dispersed on the surface of Cr_2O_3 microspheres, which proves the stability of the AuAg alloyed NPs. This can offer advanced properties with respect to the photocatalytic activity. Photoluminescence (PL) studies (Fig. 6.7) of pure Cr_2O_3, Au/Cr_2O_3 and $Ag-Au/Cr_2O_3$ were undertaken to investigate the efficiency of charge carrier traping and transfer in order to evaluate the recombination rate of charge carriers. Fig. 6.7 depicts the Photoluminescence (PL) spectra of pure Cr_2O_3, $1.18Au/Cr_2O_3$ and $0.34Ag-1.21Au/Cr_2O_3$ in the wavelength range of 300-800 nm. The first peak, around 400 nm, can be assigned to the contribution of the band to band recombination process. The intensity of PL signal indicates the recombination rate of photo-generated electron–hole pairs. PL spectra shows significantly smaller band to band PL amplitude for Ag-

Au/Cr$_2$O$_3$ compared to Au/Cr$_2$O$_3$ and Cr$_2$O$_3$ suggesting a suppression in the rate of electron/hole recombination when the semiconductor is functionalized with metal NPs.
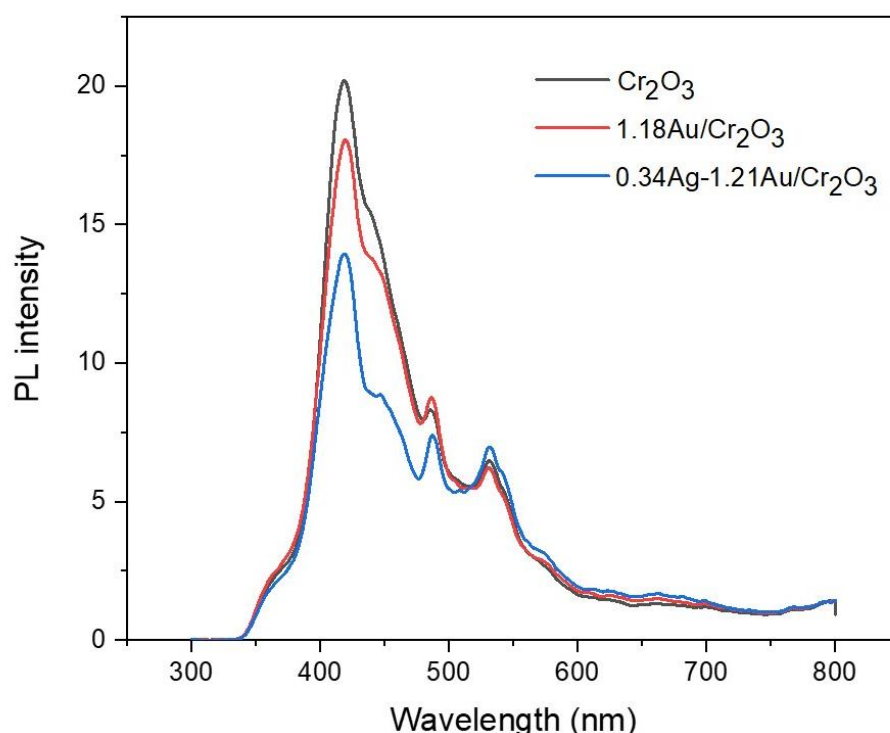
Figure 6.7. The fluorescence of the powder samples was measured employing a Fluorescence Spectrometer Perkin Elmer LS 55, using 300 nm as excitation wavelength and a cut-off filter at 350nm.

Nevertheless, a slight decrease of benzyl alcohol conversion was observed by further increasing Ag loading under the same Au content. Particularly, 86.8 %, 65.1 % and 42.1 % of benzyl alcohol was converted for 0.78Ag-1.22Au/Cr$_2$O$_3$, 1.48Ag-1.18Au/Cr$_2$O$_3$ and 2.24Ag-1.22Au/Cr$_2$O$_3$ photocatalysts respectively, indicating the superior activity of Au NPs in Ag-Au for enhancing the photocatalytic activity. The different photocatalytic performance due to metal NPs loading can be explained from a structural point of view. It should be noted that the presence of Au in the Au-Ag alloyed NPs is predominant, which means that for Ag loadings > 0.78 wt.% where the actual amount of Ag NPs is higher compared to that of Au (1.18 wt%), the Au active sites would be limited resulting in reduced photocatalytic activity [6]. Additionally, by increasing Ag loading, larger Ag NPs were acquired from TEM images (Fig. 6.3), which can induce the formation of new charge carrier recombination centers and thereby reduce the efficiency of charge separation. This behaviour agrees with other studies reported the

size-dependency of metal NPs in the photocatalytic performance, showing that catalysts with small NPs are moe active due to the more reductive character of the composite

6.2.2.2 Kinetic study of photocatalytic oxidation of benzyl alcohol

In order to further assess the effect of Ag/Au ratio on the photocatalytic oxidation of benzyl alcohol, reaction kinetics were investigated. Fig. 6.8 shows that the reaction rates fitted the pseudo-first-order kinetic model according to the following equation:

$$ln\frac{C_0}{C_0 - x} = k \cdot t \qquad (6.1)$$

where C_0 is the initial concentration, x is the concentration of formed benzaldehyde at certain reaction time, t is the reaction time and k is the rate constant. As it can be seen in Fig. 6.8, the reaction rate increased gradually over irradiation time for 3 h reaction. It should be noted that the reaction rate of benzyl alcohol oxidation was significantly affected by Ag/Au ratio. Particularly, by gradually increasing Ag content from 0.34 to 2.24 wt.% a decrease in the reaction rate was observed indicating that an excessive Ag loading could weaken charge transfer at the interfaces of bimetallic NPs.
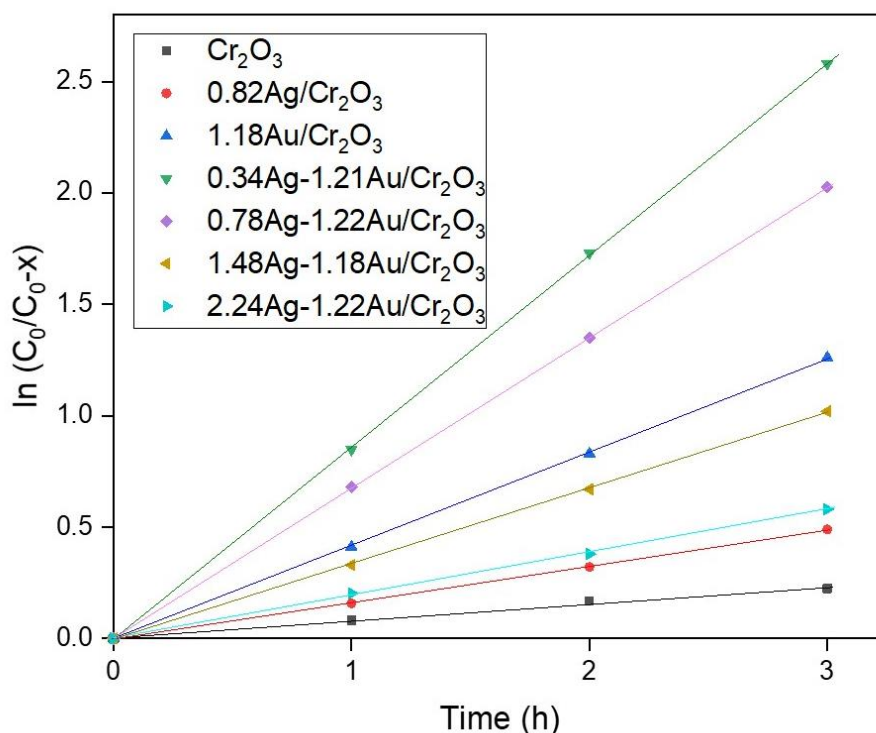
Figure 6.8. First-order kinetic plots of pure Cr_2O_3, monometallic and bimetallic photocatalysts.

The corresponding rate constants (k) for all photocatalysts were calculated and depicted in Fig. 6.9 with correlation coefficients $R^2 > 0.99$. It could be clearly seen that

0.34Ag-1.21Au/Cr_2O_3 photocatalyst possessed the highest reaction rate with a constant rate of 0.0143 min^{-1} which is 11.5 folds of bare Cr_2O_3 photocatalyst, following by 0.78Ag-1.22Au/Cr_2O_3 (0.0112 min^{-1}), 1.18Au/Cr_2O_3 (0.00701 min^{-1}), 1.48Ag-1.18Au/Cr_2O_3 (0.00567 min^{-1}), 2.24Ag-1.22Au/Cr_2O_3 (0.00322 min^{-1}), 0.82Ag/Cr_2O_3 (0.00272 min^{-1}) and Cr_2O_3 (0.00124 min^{-1}). Therefore, the synergistic effect of Ag and Au NPs decorated on the surface of Cr_2O_3 microspheres with an optimized Ag/Au ratio can significantly improve benzyl alcohol oxidation rate to benzaldehyde, implying improved electron transfer processes and enhanced charge carriers separation.
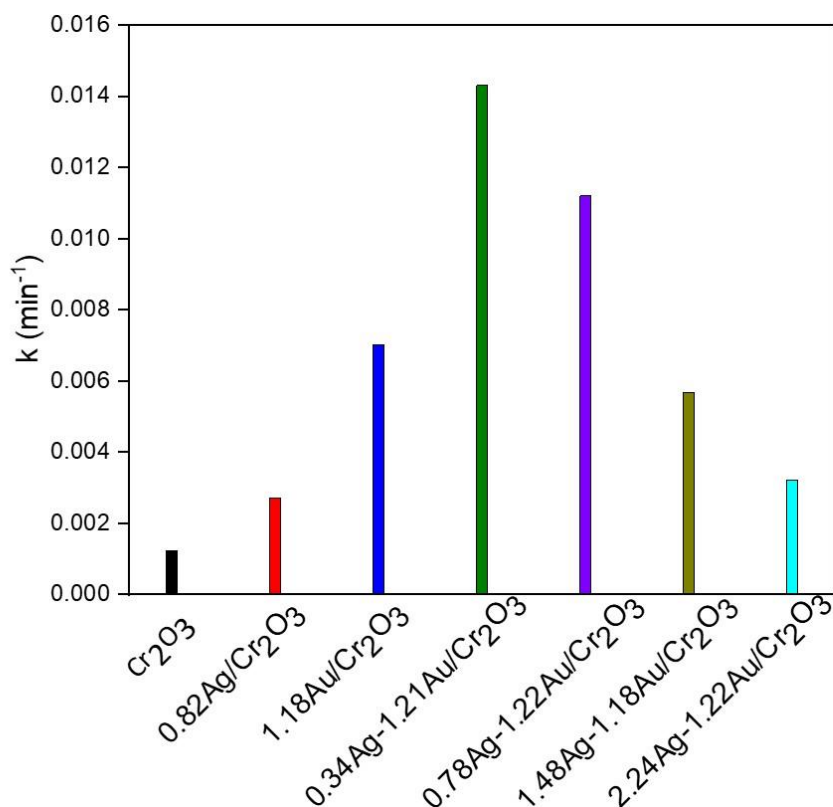
Figure 6.9. Constant rate k in the presence of pure Cr_2O_3, monometallic and bimetallic photocatalysts.

6.2.2.3   Photoelectrochemical test of Ag-Au/Cr_2O_3 microspheres

Fig. 6.10 shows the photocurrent responses of pure Cr_2O_3, 1Ag/Cr_2O_3, 3Au/Cr_2O_3 and bimetallic 0.34Ag-1.18Au/Cr_2O_3 photoelectrodes, which could evaluate the generation and transfer of photogenerated charge carriers. The photocurrent density is greatly improved over all metal-loaded Cr_2O_3 photocatalysts compared to pure Cr_2O_3. The periodic on/off photocurrents follow the order of 0.34Ag-1.21Au/Cr_2O_3 > 1.18Au/Cr_2O_3 > 0.82Ag/Cr_2O_3 > Cr_2O_3. This enhancement can be attributed to the efficient separation of the photogenerated electron-hole pairs due to the interaction between metal NPs and Cr_2O_3 microspheres [28]. The highest photocurrent response

was achieved using 0.34Ag-1.21Au/Cr_2O_3, which is consistent with the activity during photo-oxidation of benzyl alcohol, revealing the promoted generation of charge carriers near the surface of Cr_2O_3 due to the SPR excitation of metal NPs.
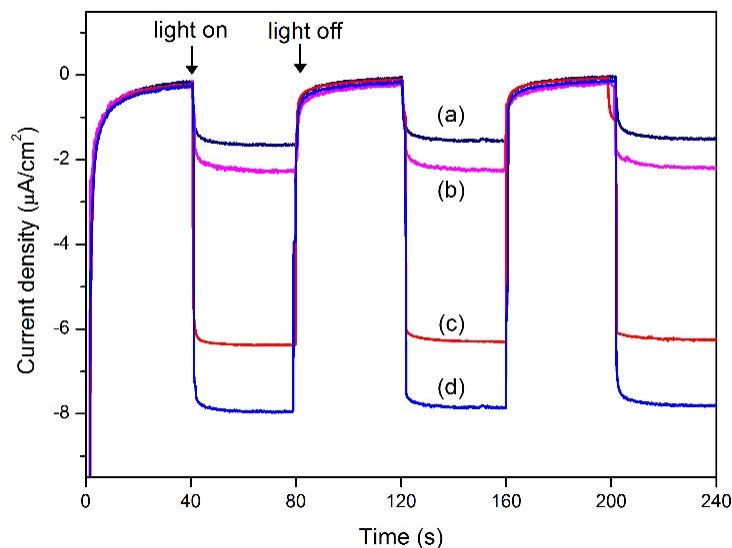
Figure 6.10. Photocurrent response of (a) Cr_2O_3, (b) 0.82Ag/Cr_2O_3, (c) 1.18Au/Cr_2O_3 and (d) 0.34Ag-1.21Au/Cr_2O_3.

6.2.3 Continuous flow experiments

6.2.3.1 Effect of flow rate

The photocatalytic performance of pure Cr_2O_3, monometallic and bimetallic NPs with optimized Ag/Au ratio was further investigated under continuous flow conditions. For continuous flow experiments, a flow reactor was designed and fabricated, as described earlier in section 3.4.2. The effect of flow rate in the photocatalytic oxidation of benzyl alcohol was investigated and the results are illustrated in Fig. 6.11. All photocatalysts presented the same trend by increasing the flow rate from 0.05 to 0.2 mL min^{-1}. Initially, an increase in the flow rate from 0.05 to 0.1 mL min^{-1} led to a higher benzyl alcohol conversion of 88.5% with 98.9 % benzaldehyde selectivity. At large residence time, the lower benzyl alcohol conversion is attributed to mass transfer limitations in terms of transfer capability of the fluid due to low flow rate (< 0.1 mL min^{-1}) [29, 30]. Especially, at very low flow rates (< 0.1 mL min^{-1}), blocking effect was observed from the dispersed NPs in the fluid. Upon further increasing the flow rate to 0.2 mL min^{-1}, only 58.5 % of benzyl alcohol was converted, indicating a decrease of the photocatalytic performance. It should be noted that the flow rate is associated with the effective

residence time. At high flow rates (> 0.15 mL min^{-1}), an enhancement in the mass transport is obtained but at the same time the interaction time between the reaction mixture containing the photocatalyst and laser irradiation is limited, leading in a decrease of the reaction rate to complete the desired photocatalytic reaction [31]. The highest benzyl alcohol conversion of 88.5 % was achieved using a flow rate of 0.1 mL min^{-1}.
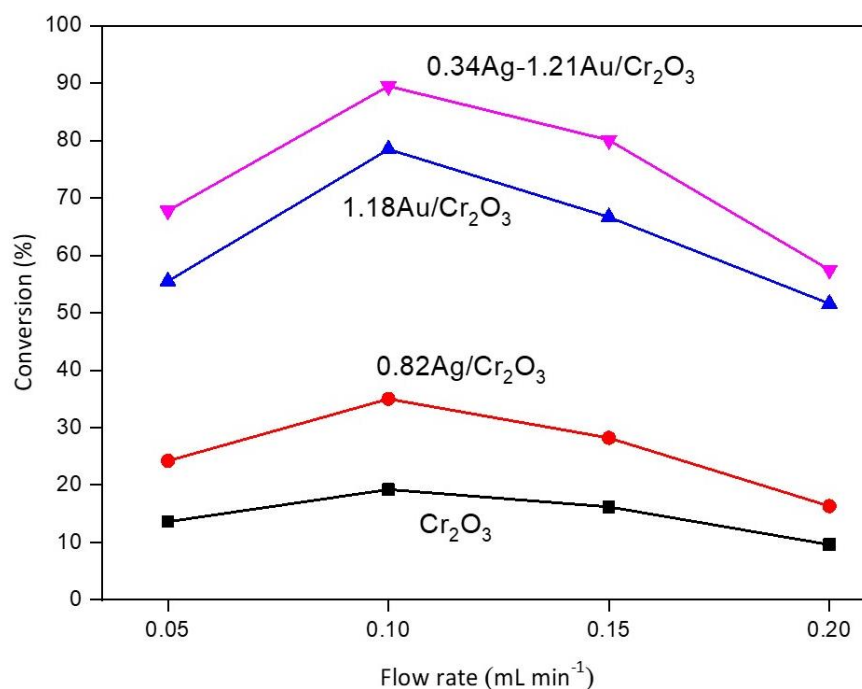
Figure 6.11. Conversion of benzyl alcohol for pure Cr_2O_3, $0.82Ag/Cr_2O_3$, $1.18Au/Cr_2O_3$ and $0.34Ag$-$1.21Au/Cr_2O_3$ for 0.5 mg mL^{-1} catalyst concentration and flow rates 0.05, 0.1, 0.15 and 0.2 mLmin^{-1}.

6.2.3.2   Effect of catalyst concentration

In addition to the influence of flow rate, the effect of photocatalyst concentration on benzaldehyde production was studied. Photocatalytic oxidation experiments were carried out with concentrations ranging from 0.2 to 1.5 mg mL^{-1} and the change of benzyl alcohol conversion with concentration is depicted in Fig. 6.12. Benzaldehyde production was significantly enhanced by increasing concentration to 1 mg mL^{-1} converting 93.7% of benzyl alcohol, while a further increase of concentration at 1.5 mg mL^{-1} led to a decrease of the converted benzyl alcohol to 84.1%. In line with the Beer-Lambert law, more photons are confined in the fluid due to the higher number of NPs in the reaction mixture, offering more active sites, resulting in enhanced benzaldehyde production [32]. The main cause of the decreased benzaldehyde for 1.5 mg mL^{-1} concentration is associated with a possible saturation of light absorption. For high

concentrations, laser light could be mainly absorbed by the upper layer close to the surface of the solution, resulting in a non-uniform distribution of light and therefore loss of photons [2]. Another possible cause for the decreased photocatalytic oxidation efficiency at high concentration of photocatalyst could be the existence of mass transfer limitations.
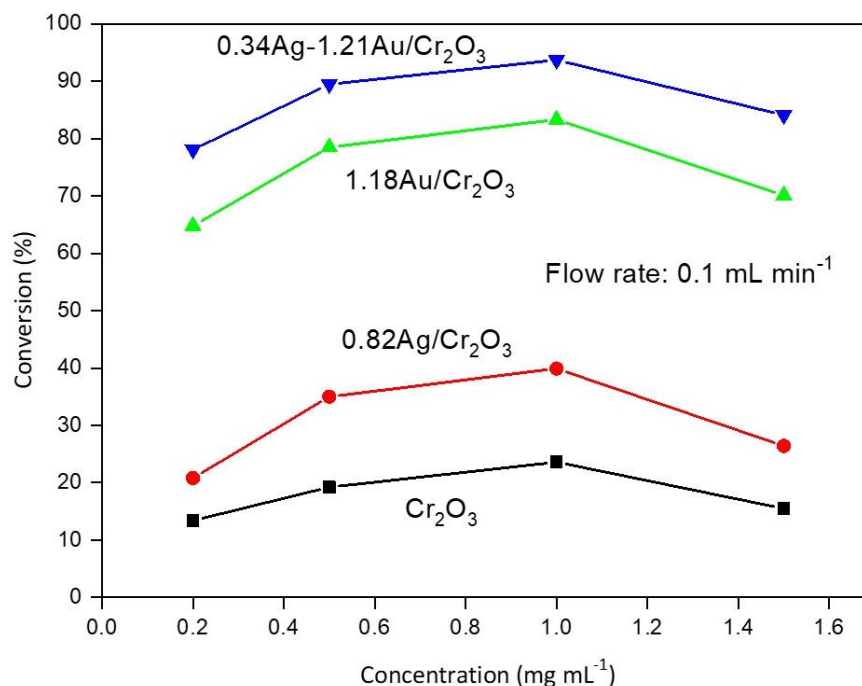
Figure 6.12. Conversion of benzyl alcohol for pure Cr_2O_3, $0.82Ag/Cr_2O_3$, $1.18Au/Cr_2O_3$ and $0.34Ag$-$1.21Au/Cr_2O_3$ for 0.1 mL min^{-1} flow rate using 0.2, 0.5, 1.0 and 1.5 mg mL^{-1} catalyst concentration.

6.2.3.3 Effect of light intensity

Light intensity plays a significant role on the photocatalytic oxidation rate of benzyl alcohol. Fig. 6.13 shows benzyl alcohol conversion as a function of laser intensity varying from 12.7 to 63.3 W/cm^2, while flow rate and catalyst amount were set at 0.1 mL min^{-1} and 1 mg mL^{-1}, respectively. Benzaldehyde production for $0.34Ag$-$1.21Au/Cr_2O_3$ photocatalyst was remarkably increased by increasing incident laser power intensity and the highest conversion of 93.7% benzyl alcohol was obtained at 500 mW. Generally, an increase of light intensity results in higher photon production with a strong electromagnetic field formed around the NPs, affecting accordingly the oxidation rate of the reaction [33].
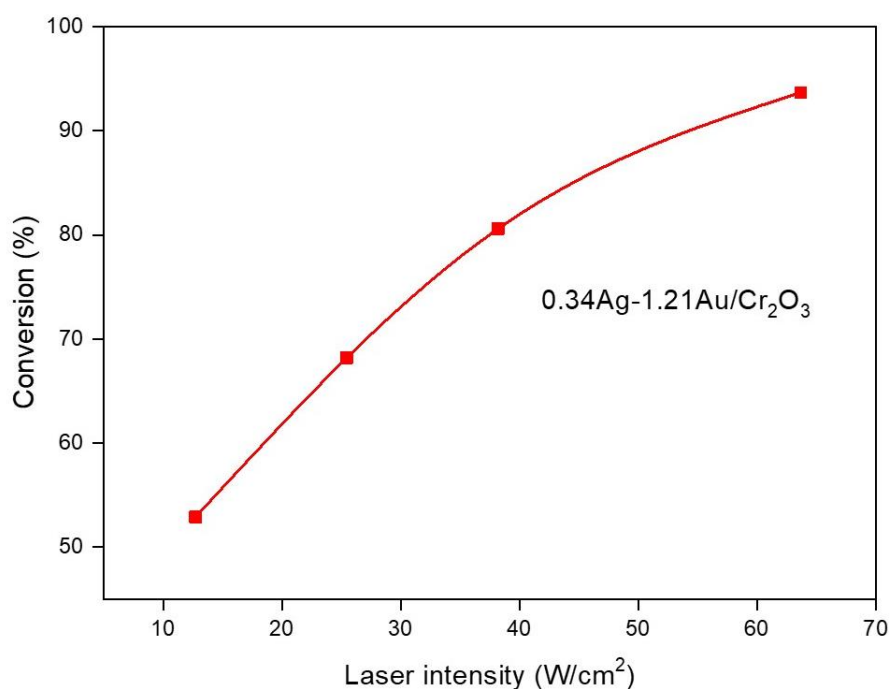
Figure 6.13. Conversion of benzyl alcohol vs laser power intensity using 0.34Ag-1.21Au/Cr$_2$O$_3$ photocatalyst for 0.1 mL min^{-1} flow rate and 1 mg mL^{-1} concentration.

Fig. 6.14 shows the reaction rate constants (k) versus residence time in the presence of 0.34Ag-1.21Au/Cr$_2$O$_3$ photocatalyst for concentration 1 mg mL^{-1} and light intensity 63.3 W/cm^2. Generally, an increase in the residence time up to 20 min led to an increase in the reaction rate constant from 0.079 to 0.113 min^{-1}. However, increasing further the residence time to 40 min resulted in lower reaction rate constant (0.028 min^{-1}), which is consistent with the conversion efficiency results versus flow rate as described in section 6.2.3.1. Benzaldehyde production was compared under batch and continuous flow conditions and the reaction rate constant was calculated based on pseudo-first order model for both batch and continuous flow system. It should be noted that the reaction rate constant of the photocatalytic oxidation using continuous flow cell with 0.1 mL min^{-1} flow rate was 7.9 times higher (0.113 min^{-1}) than that achieved using batch type reactor (0.0143 min^{-1}), implying the superior photocatalytic performance using continuous flow system.
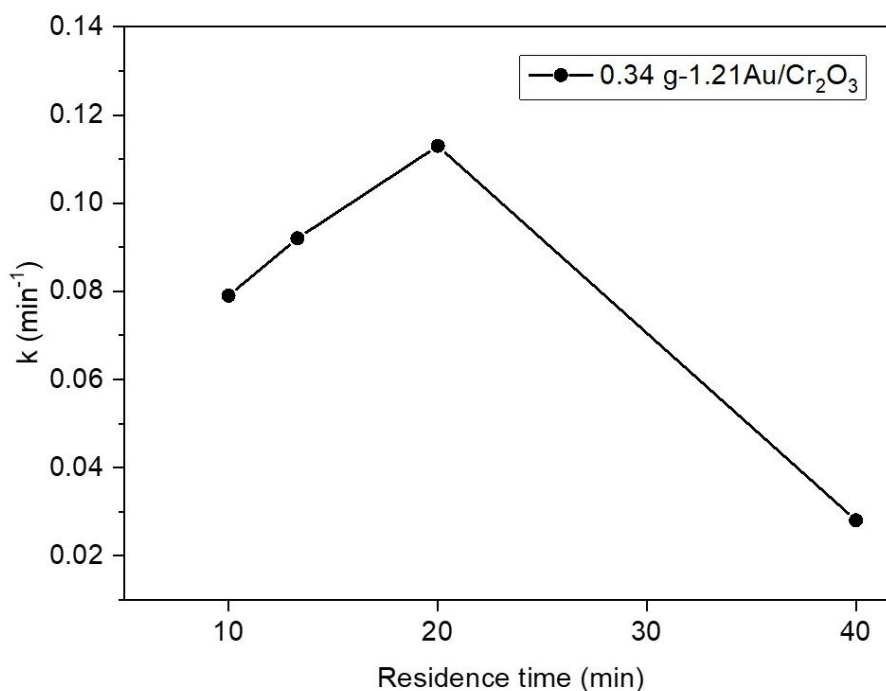
Figure 6.14. Reaction rate constant versus residence time. Photocatalyst concentration 1 mg mL^{-1} and laser intensity 63.3 W/cm^2.

6.2.3.4 Recyclability of photocatalysts

In terms of practical applications, stability and recyclability of a catalyst is of high importance. The re-usability study of 0.34Ag-1.21Au/Cr$_2$O$_3$ catalyst was carried out by the photocatalytic oxidation of benzyl alcohol under 532 nm laser irradiation and the results are presented in Fig. 6.15. After five consecutive cycles, the conversion efficiency of 0.34Ag-1.21Au/Cr$_2$O$_3$ photocatalyst presented a slight decrease from 93.7 to 89.1% with no loss of benzaldehyde selectivity, which could possibly arise from the mass loss during the recovery of the catalyst. These results revealed a negligible loss of activity after prolonged irradiation time, indicating the good stability of the photocatalyst.
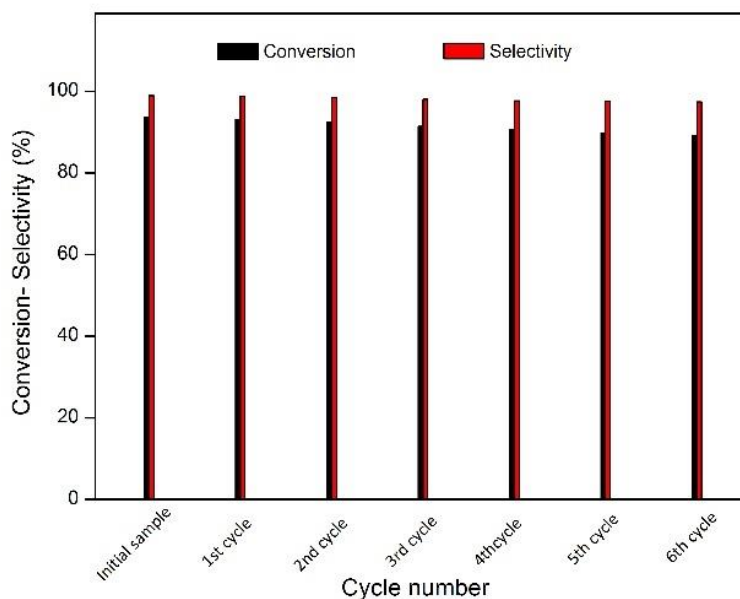
Figure 6.15. Recyclability test of 0.34Ag-1.21Au/Cr_2O_3 photocatalyst.

6.2.3.5 Role of photothermal effect on photocatalytic activity

As previously reported, operating temperature is critical to the photocatalytic oxidation of benzyl alcohol. For understanding the role of photothermal effect in the photocatalytic process, the photocatalytic oxidation of benzyl alcohol was conducted under the same conditions as described in section 3.5.2, Chapter 3, but in the absence of water to keep the temperature of the reaction constant at 21 $^{\circ}$C. Fig. 6.16 presents the temperature increase of the different suspensions irradiated by laser light. As it can be seen, 0.34Ag-1.21Au/Cr_2O_3 presented the higher temperature rise ($\sim$ 27.5 $^{\circ}$C) indicating a higher optical absorption of Ag-Au nanoparticles compared with that of pure Cr_2O_3 ($\sim$ 5 $^{\circ}$C), 0.82Ag/Cr_2O_3 ($\sim$ 6.5 $^{\circ}$C) and 1.18Au/Cr_2O_3 ($\sim$ 17.5°C). The significant temperature rise can be attributed to the strong photothermal effect of Ag-Au nanoparticles decorated on Cr_2O_3 microspheres.
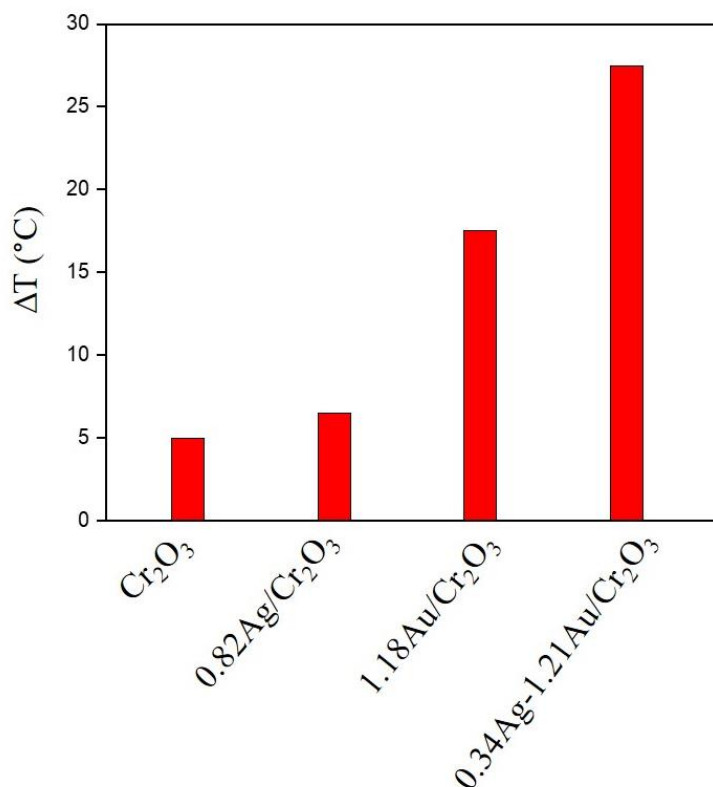
Figure 6.16. Temperature profile of pure Cr_2O_3 and Ag-Au/Cr_2O_3 under laser irradiation.

For understanding the photothermal effect on the photocatalytic process, the photocatalytic rate constant k was calculated (Fig. 6.17) based on pseudo-first-order kinetic model. For temperatures below 29 °C, the contribution of the photothermal effect on the total reaction was just 7.3% for Cr_2O_3 (k=0.0095 min^{-1}) and 8.7 % for 0.82Ag/Cr_2O_3 (k=0.0212 min^{-1}). With respect to the operating temperature, the photothermal effect on the photoreaction is significant for temperatures above 37 °C. The value of rate constant k obtained for 1.18Au/Cr_2O_3 was 0.065 min^{-1}, which is 1.27 times higher compared to that reported at controlled temperature (21 °C) by a water bath (0.051 min^{-1}). For bimetallic 0.34Ag-1.21Au/Cr_2O_3 (k=0.168 min^{-1}) the temperature raised to 48.6 °C, revealing a remarkable rate improvement. In this case, the photothermal-assisted reaction provides a rate enhancement of 48% compared to the controlled temperature system (k=0.113 min^{-1}). These findings reveal that the photothermal effect can accelerate significantly the photocatalytic reaction rates.
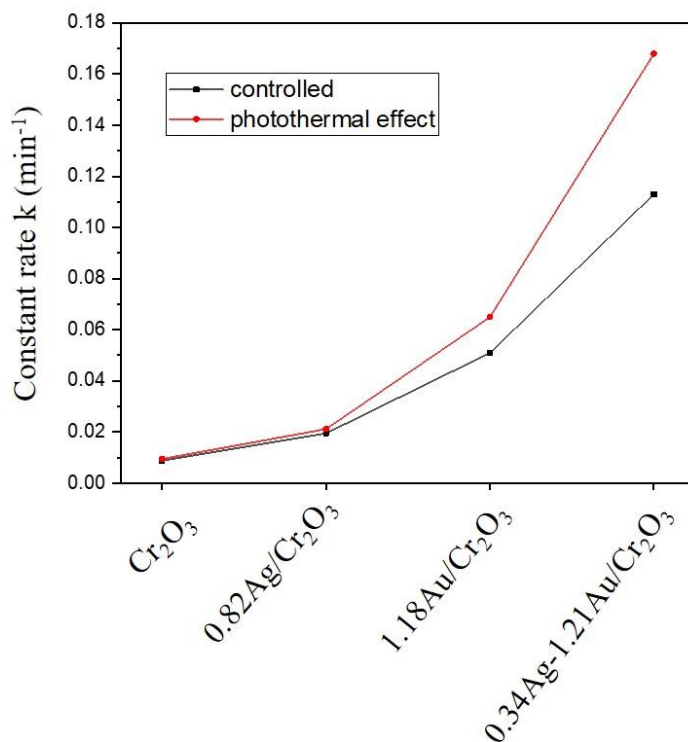
Figure 6.17. Constant rate k in the presence of pure Cr_2O_3 and Ag - Au loaded samples at flow rate 0.2 mLmin^{-1}, photocatalyst concentration 1 mg mL-1 and laser intensity 63.3 W/cm^2, by controlling temperature at 21°C (black line) and without controlling temperature revealing the photothermal effect (red line).

6.2.3.6 Investigation of the photo-oxidation mechanism

To understand the photocatalytic reaction mechanism of 0.34Ag-1.21Au/Cr$_2$O$_3$, a series of controlled experiments were carried out to reveal the contribution of oxidative species by adding radical scavengers (Fig. 6.18). The photocatalytic conversion of benzyl alcohol slightly decreased (81.2 %) using tert-butyl alcohol (TBA) for trapping hydroxyl radicals (OH˙), indicating that OH˙ were not involved in the oxidation of benzyl alcohol. Whereas, the addition of AO, AgNO$_3$ and BQ to capture hole (h$^+$), electron (e$^-$) and superoxide radicals ($^˙O_2^-$) scavengers, remarkably affected the photocatalytic performance resulting in significant decrease of benzyl alcohol conversion. Particularly, the conversion suppressed to 45.3 %, 29.8 % and 38.6 % in the presence of AO, AgNO$_3$ and BQ respectively. Additionally, the photocatalytic oxidation reaction performed under air atmosphere converted 70.1 benzyl alcohol, demonstrating that molecular oxygen was a significant oxidizing agent for the photo-oxidation process. From the above results, it can be concluded that $^˙O_2^-$ and h$^+$ were the dominant active species in the oxidation of benzyl alcohol into benzaldehyde.
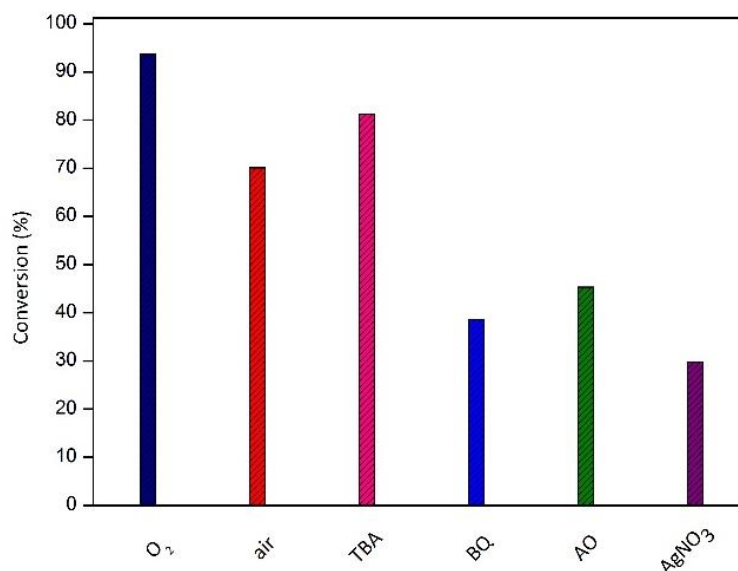
Figure 6.18. Photocatalytic oxidation process under O_2 and air atmosphere. Controlled experiments utilizing trapping agents: tert-butyl alcohol (TBA), 1,4-benzoquinone (BQ), ammonium oxalate (AO) and $AgNO_3$. Capture experiments were carried out using 0.34Ag-1.21Au/Cr_2O_3 photocatalyst.

The following mechanism for the photo-oxidation of benzyl alcohol into benzaldehyde using Ag-Au/Cr_2O_3 is proposed. Under visible light illumination, Cr_2O_3 microspheres could be excited producing electron-hole pairs. Subsequently, electrons migrate from the conduction band of Cr_2O_3 to Au and Ag across the Schottky barrier. Meanwhile, the local electric field enhancement around AgAu NPs and nearby the Cr_2O_3 microspheres, caused by excitation of AgAu NPs, promotes the electron-hole pair formation on Cr_2O_3 surface with higher rate compared to normal incident light. The electrons accumulated on AgAu NPs surface participate in the reduction of O_2 to produce superoxide radical species ($^{\cdot}O_2^{-}$) [Eq. 6.1], while the holes on the surface of Cr_2O_3 contribute to the activation of aromatic alcohol following the pathway in Eq. 6.2. Subsequently, $^{\cdot}O_2^{-}$ radicals could in turn trap two protons from the activated aromatic alcohol adsorbed at the neighbor sites to generate benzaldehyde as the product [Eq 6.3].

$$O_2 \xrightarrow{e^-} \cdot O_2^{-} \tag{6.1}$$

$$Ph - CH_2 - OH \xrightarrow{h^+} Ph - \overset{+\cdot}{C}H_2 - OH \tag{6.2}$$

$$Ph - \overset{+\cdot}{C}H_2 - OH \xrightarrow{\cdot O_2^{-}} Ph - CH = O + H_2O_2 \tag{6.3}$$

128
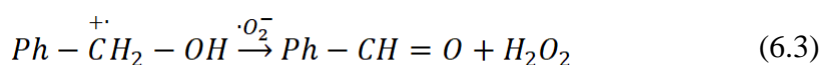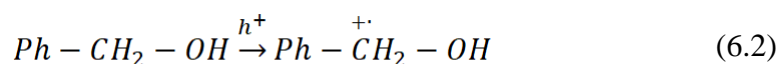
6.3 Conclusions

The work outlined in this Chapter met the objective set in the thesis to explore the capability of bimetallic Ag/Au NPs to catalyze selective oxidation of benzyl alcohol to benzaldehyde under laser light irradiation. Bimetallic Ag/Au NPs were successfully deposited on the surface of hydrothermally synthesized Cr_2O_3 microspheres and their performance for batch and continuous flow synthesis of benzaldehyde was evaluated. It can be concluded that all monometallic and bimetallic photocatalysts showed an improved conversion of benzyl alcohol, compared to pure Cr_2O_3. For batch reaction conditions, among the tested photocatalysts, $0.34Ag-1.21Au/Cr_2O_3$ exhibited the highest benzyl alcohol conversion (92.4 %) with high selectivity after 3 h of laser irradiation, which is 4.5 times that of pure Cr_2O_3, 1.3 times that of $1.18Au/Cr_2O_3$ and 2.5 times that of $0.84Ag/Cr_2O_3$ photocatalyst. Ag/Au ratio is of key importance in the development of effective photocatalysts for photocatalytic oxidation systems. The enhanced photocatalytic performance of bimetallic Ag-Au NPs can be ascribed to the intense photo-absorption and efficient separation of photogenerated charge carriers, which arise from the coupling of plasmonic metals with Cr_2O_3, in addition to the synergistic effect between bimetallic Ag-Au NPs and Cr_2O_3 microspheres. Under continuous flow conditions, the effect of flow rate, catalyst concentration and laser power intensity were investigated. It was confirmed that under optimized conditions (flow rate: 0.1 mL min^{-1}, photocatalyst concentration: 1 mg mL^{-1}, laser intensity: 500 mW), a highest benzyl alcohol conversion of 93.7 % with 98.9 % benzaldehyde selectivity was achieved using $0.34Ag-1.21Au/Cr_2O_3$ after approximately 20 min of laser irradiation. It should be noted that a maximum reaction rate constant of 0.138 min^{-1} was obtained using continuous flow reactor, which was almost an order of magnitude superior to the values achieved using batch reactor for photocatalytic oxidation of benzyl alcohol to benzaldehyde. The investigation of the photothermal effect on the photocatalytic performance revealed an enhancement of rate constant up to 48% for $0.34Ag-1.21Au/Cr_2O_3$, which is encouraging with regards to assisting the photocatalytic activity *via* the photothermal effect. Finally, the mechanistic studies of benzyl alcohol reaction demonstrated that $^{\cdot}O_2^{-}$ and h^{+} were the dominant active species in the oxidation of benzyl alcohol into benzaldehyde while O_2 was an important oxidizing agent for the photo-oxidation process.

This work is relevant to the overall aim of this thesis as it was demonstrated that high performing bimetallic Ag/Au NPs with optimized Ag/Au ratio behave as efficient photocatalysts for the selective benzyl alcohol oxidation to benzaldehyde. The use of

Ag/Au NPs decorated on the surface of Cr_2O_3 microspheres for continuous flow synthesis of benzaldehyde has not been previously reported, so extends the knowledge of this research area.

6.4 References

[1] X. Zhang, X. Ke, J. Yao, Recent development of plasmon-mediated photocatalysts and their potential in selectivity regulation, Journal of Materials Chemistry A, 6 (2018) 1941-1966.

[2] M. Sahoo, S. Mansingh, K.M. Parida, A bimetallic Au–Ag nanoalloy mounted LDH/RGO nanocomposite: a promising catalyst effective towards a coupled system for the photoredox reactions converting benzyl alcohol to benzaldehyde and nitrobenzene to aniline under visible light, Journal of Materials Chemistry A, 7 (2019) 7614-7627.

[3] Y.-J. Song, Y.M. López-De Jesús, P.T. Fanson, C.T. Williams, Preparation and Characterization of Dendrimer-Derived Bimetallic Ir–Au/Al_2O_3 Catalysts for CO Oxidation, The Journal of Physical Chemistry C, 117 (2013) 10999-11007.

[4] R. Nazir, P. Fageria, M. Basu, S. Pande, Decoration of Carbon Nitride Surface with Bimetallic Nanoparticles (Ag/Pt, Ag/Pd, and Ag/Au) *via* Galvanic Exchange for Hydrogen Evolution Reaction, The Journal of Physical Chemistry C, 121 (2017) 19548-19558.

[5] X. Tao, L. Shao, R. Wang, H. Xiang, B. Li, Synthesis of BiVO4 nanoflakes decorated with AuPd nanoparticles as selective oxidation photocatalysts, Journal of Colloid and Interface Science, 541 (2019) 300-311.

[6] R. Wang, B. Li, Y. Xiao, X. Tao, X. Su, X. Dong, Optimizing Pd and Au-Pd decorated Bi2WO6 ultrathin nanosheets for photocatalytic selective oxidation of aromatic alcohols, Journal of Catalysis, 364 (2018) 154-165.

[7] S.A. Makhlouf, Z.H. Bakr, H. Al-Attar, M.S. Moustafa, Structural, morphological and electrical properties of Cr_2O_3 nanoparticles, Materials Science and Engineering: B, 178 (2013) 337-343.

[8] T. Jiang, C. Jia, L. Zhang, S. He, Y. Sang, H. Li, Y. Li, X. Xu, H. Liu, Gold and gold–palladium alloy nanoparticles on heterostructured TiO_2 nanobelts as plasmonic photocatalysts for benzyl alcohol oxidation, Nanoscale, 7 (2015) 209-217.

[9] N. Gogoi, G. Borah, P.K. Gogoi, T.R. Chetia, TiO_2 supported gold nanoparticles: An efficient photocatalyst for oxidation of alcohol to aldehyde and ketone in presence of visible light irradiation, Chemical Physics Letters, 692 (2018) 224-231.

[10] Y. Bai, N. Cherkasov, S. Huband, D. Walker, R.I. Walton, E. Rebrov, Highly Selective Continuous Flow Hydrogenation of Cinnamaldehyde to Cinnamyl Alcohol in a Pt/SiO_2 Coated Tube Reactor, Catalysts, 8 (2018) 58-75.

[11] D. Motta, F.J.S. Trujillo, N. Dimitratos, A. Villa, L. Prati, An investigation on AuPt and AuPt-Bi on granular carbon as catalysts for the oxidation of glycerol under continuous flow conditions, Catalysis Today, 308 (2018) 50-57.

[12] I. Rossetti, Continuous flow (micro-)reactors for heterogeneously catalyzed reactions: Main design and modelling issues, Catalysis Today, 308 (2018) 20-31.

[13] Rossetti. I, (2016) Flow Chemistry: New Concepts from Batch to Continuous Organic Chemistry, Industrial Chemistry pp. 1-2.

[14] V. Hessel, D. Kralisch, N. Kockmann, T. Noël, Q. Wang, Novel Process Windows for Enabling, Accelerating, and Uplifting Flow Chemistry, ChemSusChem, 6 (2013) 746-789.

[15] J.Z.Y. Tan, F. xia, M.M. Maroto-Valer, Novel Raspberry–like Microspheres of Core–shell Cr_2O_3/TiO_2 Nanoparticles for CO_2 Photoreduction, ChemSusChem, (2019) 5246-5252.

[16] J. Ding, J. Ming, D. Lu, W. Wu, M. Liu, X. Zhao, C. Li, M. Yang, P. Fang, Study of the enhanced visible-light-sensitive photocatalytic activity of Cr2O3-loaded titanate nanosheets for Cr(vi) degradation and H_2 generation, Catalysis Science & Technology, 7 (2017) 2283-2297.

[17] H. Sun, L. Wang, D. Chu, Z. Ma, A. Wang, Synthesis of porous Cr_2O_3 hollow microspheres *via* a facile template-free approach, Materials Letters, 140 (2015) 35-38.

[18] J. Lu, H. Wang, D. Peng, T. Chen, S. Dong, Y. Chang, Synthesis and properties of Au/ZnO nanorods as a plasmonic photocatalyst, Physica E: Low-dimensional Systems and Nanostructures, 78 (2016) 41-48.

[19] W. Gao, X. Zhang, X. Su, F. Wang, Z. Liu, B. Liu, J. Zhan, H. Liu, Y. Sang, Construction of bimetallic Pd-Ag enhanced $AgBr/TiO_2$ hierarchical nanostructured photocatalytic hybrid capillary tubes and devices for continuous photocatalytic degradation of VOCs, Chemical Engineering Journal, 346 (2018) 77-84.

[20] C. Wang, H. Yin, R. Chan, S. Peng, S. Dai, S. Sun, One-Pot Synthesis of Oleylamine Coated AuAg Alloy NPs and Their Catalysis for CO Oxidation, Chemistry of Materials, 21 (2009) 433-435.

[21] Y. Guan, N. Zhao, B. Tang, Q. Jia, X. Xu, H. Liu, R.I. Boughton, A stable bimetallic Au–Ag/TiO_2 nanopaper for aerobic oxidation of benzyl alcohol, Chemical Communications, 49 (2013) 11524-11526.

[22] L. Collado, A. Reynal, J.M. Coronado, D.P. Serrano, J.R. Durrant, V.A. de la Peña O'Shea, Effect of Au surface plasmon nanoparticles on the selective CO_2 photoreduction to CH4, Applied Catalysis B: Environmental, 178 (2015) 177-185.

[23] S.K. Cushing, J. Li, F. Meng, T.R. Senty, S. Suri, M. Zhi, M. Li, A.D. Bristow, N. Wu, Photocatalytic Activity Enhanced by Plasmonic Resonant Energy Transfer from Metal to Semiconductor, Journal of the American Chemical Society, 134 (2012) 15033-15041.

[24] M.R. Khan, T.W. Chuan, A. Yousuf, M.N.K. Chowdhury, C.K. Cheng, Schottky barrier and surface plasmonic resonance phenomena towards the photocatalytic reaction: study of their mechanisms to enhance photocatalytic activity, Catalysis Science & Technology, 5 (2015) 2522-2531.

[25] W. Hou, Z. Liu, P. Pavaskar, W.H. Hung, S.B. Cronin, Plasmonic enhancement of photocatalytic decomposition of methyl orange under visible light, Journal of Catalysis, 277 (2011) 149-153.

[26] S. Bhardwaj, B. Pal, Photodeposition of Ag and Cu binary co-catalyst onto TiO_2 for improved optical and photocatalytic degradation properties, Advanced Powder Technology, 29 (2018) 2119-2128.

[27] J.-H. Liu, A.-Q. Wang, Y.-S. Chi, H.-P. Lin, C.-Y. Mou, Synergistic Effect in an Au−Ag Alloy Nanocatalyst: CO Oxidation, The Journal of Physical Chemistry B, 109 (2005) 40-43.

[28] S. Mubeen, G. Hernandez-Sosa, D. Moses, J. Lee, M. Moskovits, Plasmonic Photosensitization of a Wide Band Gap Semiconductor: Converting Plasmons to Charge Carriers, Nano Letters, 11 (2011) 5548-5552.

[29] M. Belekoukia, E. Kalamaras, J.Z.Y. Tan, F. Vilela, S. Garcia, M.M. Maroto-Valer, J. Xuan, Continuous flow-based laser-assisted plasmonic heating: A new approach for photothermal energy conversion and utilization, Applied Energy, 247 (2019) 517-524.

[30] L. Li, R. Chen, X. Zhu, H. Wang, Y. Wang, Q. Liao, D. Wang, Optofluidic Microreactors with TiO2-Coated Fiberglass, ACS Applied Materials & Interfaces, 5 (2013) 12548-12553.

[31] M. Rezaei, S.J. Royaee, M. Jafarikojour, Performance evaluation of a continuous flow photocatalytic reactor for wastewater treatment, Environmental Science and Pollution Research, 21 (2014) 12505-12517.

[32] X. Cheng, R. Chen, X. Zhu, Q. Liao, X. He, S. Li, L. Li, Optofluidic membrane microreactor for photocatalytic reduction of CO2, International Journal of Hydrogen Energy, 41 (2016) 2457-2465.

[33] M. Wu, J.-H. Pang, P.-P. Song, J.-J. Peng, F. Xu, Q. Li, X.-M. Zhang, Visible light-driven oxidation of vanillyl alcohol in air with Au–Pd bimetallic nanoparticles on phosphorylated hydrotalcite, New Journal of Chemistry, 43 (2019) 1964-1971.

Chapter 7 - Conclusions and Future work

7.1   Conclusions

This Thesis demonstrated the efficient use of plasmonic nano-photocatalysts for the selective oxidation of benzyl alcohol to benzaldehyde initiated by visible light, by conducting an extensive investigation of the parameters that are of key importance. Research investigations were carried out from the study of physicochemical and photothermal properties of plasmonic nano-photocatalysts to the exploration of plasmonic metals loading, ratio of bimetallic NPs (Ag/Au), photocatalyst concentration, light intensity as well as evaluate the effect of performing the reaction under continuous flow conditions.

So far, Au/Cr_2O_3 and $Ag-Au/Cr_2O_3$ have not been used as photocatalysts for batch and continuous flow synthesis of benzaldehyde and generally for the photocatalytic oxidation of benzyl alcohols. The different supports used so far (TiO_2, $BiVO_4$, CeO_2, SiO_2, GO and Bi_2WO_6) decorated with mono- and bi-metallic NPs (Au, Ag, Pt and Pd) achieved up to 82% benzyl alcohol conversion with 99% benzaldehyde selectivity under several hours of irradiation (8 hours). Detailed values of benzyl alcohol conversion obtained used the above supports are described in Literature review section 2.5. Benzyl alcohol conversion achieved in this Thesis (93.7% conversion with 99% benzaldehyde selectivity using $Ag-Au/Cr_2O_3$) is much higher at a shorter reaction time (3 hours laser irradiation) than the reported values in the literature using other semiconductors as supports for noble metals, implying the importance of supports that absorb light throughout the UV-Vis region. A more fair comparison between the data obtained from this thesis and literure would require reaction rate data but the results reported in the literature mainly stem from benzyl alcohol conversion or benzaldehyde production. In case of photothermal heating of plasmonic NPs, different studies performed photothermal experiments to investigate photothermal effect on assisting catalytically 4-nitrophenol reduction or degradation of RhB using Au NPs and degradation of nitropehnol using Ag NPs. The authors reported a temperature increase of 35 ˚C for Au NPs and 5 ˚C for Ag NPs. In this Thesis, the phothermal experiments revealed a temperature increase of 18 °C for Au NPs, 7 °C for Ag NPs and 27 °C for Ag-Au NPs, which contributed to a significant rate enhancement of 26%, 8.7% and 48% respectively. It should be mentioned here that the existing studies for photocatalytic oxidation of benzyl alcohol used water bath solutions to drive the reaction at room

temperature without exploring how the photothermal effect of plasmonic nanoparticles could assist catalytic process.

The following conclusions of each chapter can be made from the experimental investigations reported in this Thesis. The connectivity between the different chapters of this thesis highlight how the objectives contribute to the overall aim.

The objective of Chapter 4 was to investigate the surface plasmon resonance and particularly the photothermal effect of Au NPs by conducting a well-controlled experiment under continuous flow conditions using 532 nm laser irradiation. Initially, the optical properties of Au/TiO$_2$ nanoparticles were investigated, showing that plasmonic nanoparticles exhibited a remarkable absorption in the region 500-550 nm, attributed to the LSPR effect excited on Au NPs' surface. From photothermal experiments it can be concluded that the temperature of the nanofluids was remarkably increased in the presence of Au NPs. This phenomenon is related to the enhanced absorption of Au NPs in the visible region, which can be ascribed to the localized surface plasmon resonance effect on the surface of Au nanoparticles. Particularly, 0.84 wt.% Au nanofluid exhibited a significant higher temperature achieving up to 32˚C compared to that of TiO$_2$ nanofluid (22.5 ˚C) and water-based fluid (20.5 ˚C). It should be noted that Au loading influenced remarkably the temperature profile. By increasing Au loading from 0.56 to 1.18 wt.%, a temperature rise of 4˚C was observed which is related to higher absorption of Au NPs and the small particle size resulting in higher thermal conductivity. However, a further increase of Au loading to 1.86 wt.% led to a temperature decrease which can be caused by the excessive Au loading resulting in the increase of the mean size of Au NPs and to the formation of Au agglomerates, as was confirmed from TEM images. Then, the effect of flow rate on temperature profile was explored and the results revealed that the higher temperature increase was obtained using an optimized flow rate of 0.1 mL min^{-1}. By increasing the flow rate from 0.05 to 0.1 mL min^{-1} a higher temperature was achieved while a further increase of the flow rate up to 0.4 mL min^{-1} led to the lowering of the temperature. At large residence time (> 20 min) mass transfer limitations of nanofluids were observed leading to lower temperature. Despite the fact that mass transport (> 0.1 mL min^{-1}) was improved using higher flow rates, temperature was still lower because the nanofluid does not remain under illumination for sufficient time. After optimizing Au loading and flow rate, parameters such concentration of nanoparticles and laser intensity were studied. An initial increase of concentration from 0.2 to 1 mg mL^{-1} resulted in achieving the highest temperature up to 31.5 ˚C, which is related to the fact that the amount of suspended

nanoparticles in milli-Q water was higher, so more light was confined in the nanofluid. Conversely, the temperature decreased to 26.3 $^{\circ}$C upon further increasing the concentration to 1.4 mg mL^{-1}. This phenomenon can be ascribed to saturation of the absorption of light caused by a non-uniform distribution of NPs causing precipitation as confirmed from UV-Vis spectra.

The work in Chapter 4 enhanced our understanding on the parameters that affect the optical and photothermal properties of plasmonic Au nanoparticles under continuous flow conditions. The concept of continuous-flow plasmonic heating of Au/TiO$_2$ nanofluid, enabled the research work in Chapters 5 and 6 by extending the use of plasmonic metals such as Au, which benefit from considerable optical and photothermal properties, in photocatalytic applications.

Having established the surface plasmon resonance effect of Au NPs decorated on metal oxides, the objective of Chapter 5 was to investigate the photocatalytic oxidation of benzyl alcohol using Au loaded raspberry-like Cr$_2$O$_3$ microspheres under monochromatic 532 nm laser irradiation. The amount of loaded Au nanoparticles significantly affected the efficiency of photocatalytic oxidation of benzyl alcohol to benzaldehyde. It could be clearly observed that by increasing Au content from 0.64 to 1.18 wt.%, the highest reaction rate was obtained with a constant rate of 0.00701 min^{-1}, which is 2.3 fold of 0.64 wt.% Au. The improved reaction rate over 1.18 wt.% Au/Cr$_2$O$_3$ photocatalysts can be ascribed to the plasmon induced electromagnetic field enhancement near the surface of Au NPs in the semiconductor, which increased the generation rate of the photoexcited electron holes at Cr$_2$O$_3$. However, a further increase of Au loading to 1.82 wt.% led to a decrease in the reaction rate, suggesting that an optimised loading is very important to obtain high yield and selectivity towards benzaldehyde. In case of excessive Au content, photogenerated charge carrier recombination centers were formed that resulted in reduced photocatalytic activity. The effect of support on the photocatalytic activity was studied by using TiO$_2$ NPs as support. The results revealed that Au/TiO$_2$ photocatalysts showed only 39.1% conversion of benzyl alcohol compared with Cr$_2$O$_3$ supported Au NPs which converted 81.4%. The predominant reason for this trend is related to the fact that Cr$_2$O$_3$ microspheres not only play the role of support for Au NPs, but also participate actively in the photocatalytic oxidation of benzyl alcohol due to their significant visible light absorption compared to TiO$_2$ NPs which absorb light only in the UV region. Photothermal-assisted experiments showed an enhanced constant rate (k=0.00888 min^{-1}) which provides a 26% rate enhancement compared to that obtained at room

temperature. It can be concluded that the photothermal effect that stems from plasmonic Au NPs can boost the photocatalytic performance depending on the temperature change. Finally, a series of scavenging experiments were performed to explore the photocatalytic mechanism of Au-Cr_2O_3 microspheres. It can be concluded that oxygen acts as a trap to capture photogenerated electrons, providing $^{\cdot}O_2^{-}$, which could suspend the charge carrier recombination and promote the oxidation of benzyl alcohol.

High performing monometallic Au nanoparticles decorated on Cr_2O_3 microspheres for the photo-oxidation of benzyl alcohol to benzaldehyde inspired the work in Chapter 6 to study the activity of bimetallic nanoparticles over their monometallic counterparts by investigating the significance of Ag/Au ratio. Raspberry-like Cr_2O_3 microspheres were decorated with Au and Ag NPs and their performance was investigated *via* benzyl alcohol oxidation under 532 nm laser irradiation using batch and continuous flow system. It was concluded that the photocatalytic oxidation of benzyl alcohol to benzaldehyde is directly related to Ag/Au ratio, indicating the importance of optimized loading of Au and Ag NPs. Bimetallic 0.34Ag-1.21Au/Cr_2O_3 microspheres exhibited synergistically enhanced activity and stability for catalyzing aerobic oxidation of benzyl alcohol under visible laser irradiation achieving 93.7% conversion of benzyl alcohol with an impressive 98.9% benzaldehyde selectivity. The enhanced photocatalytic performance of bimetallic Ag-Au NPs can be ascribed to the intense photo-absorption and efficient separation of photogenerated charge carriers, which arise from the coupling of plasmonic metals with Cr_2O_3, in addition to the synergistic effect between bimetallic AuAg NPs and Cr_2O_3 microspheres. However, by gradually increasing Ag content from 0.34 to 2.24 wt.%, only 42% of benzyl alcohol was converted indicating the superior activity of Au NPs in Au-Ag for enhancing the photocatalytic activityUnder continuous flow conditions, different parameters, such as concentration of metal nanoparticles, flow rate and laser intensity that affected significantly the photocatalytic performance were studied thoroughly. The importance of optimized flow rate in terms of efficient mass transfer and the sufficient interaction time between the reaction mixture containing the photocatalyst and laser irradiation was underlined. Additionally, concentration of NPs was investigated showing that a higher number of NPs in the reaction mixture, offering more active sites, results in enhanced benzaldehyde production while a high concentration of NPs can lead to saturation of light absorption and mass transfer limitations. The reaction rate constant using continuous flow system was almost an order of magnitude higher compared to that of batch system for the photocatalytic oxidation of benzyl alcohol to benzaldehyde.

Finally, photothermal effect on the photocatalytic performance was explored indicating a 48% rate constant enhancement for 0.34Ag-1.21Au/Cr_2O_3, revealing that plasmonic heating effect can boost the photocatalytic performance.

The work in this Thesis meets all the objectives that have been set and contribute to the principal aim of investigating the batch and continuous flow synthesis of commercially valuable products such as benzaldehyde using plasmonic metal nanoparticles decorated on metal oxides as photocatalysts.

7.2 Future work

Based on the outcomes of this Thesis, further investigations are proposed to address the existing challenges in terms of reaction rate and optimize the photocatalytic performance enabling a viable system. The suggested routes that follow on from the work presented in this Thesis are discussed below:

7.2.1 Design of advanced optofluidic reactor

As described in Chapters 4 and 6, a continuous flow system is a promising route to deal with the required needs of designing a system with high photothermal and/or photocatalytic conversion efficiency. Inspired by the above findings, development of an optofluidic reactor is proposed in order to enhance the overall efficiency and reaction rate. Optofluidics is a technology that integrates optics and fluids on the micro or nanoscale and exploits their interaction to provide enhanced function and performance. This approach can offer low energy consumption, increased heat and mass transfer, large surface area to volume ratio, and precise control over fluids and light at small scales. Reactor development process is a significant engineering challenge where many factors should be taken under consideration including reactor geometry, material of construction and flow rate. This suggestion enables kinetic studies and optimization of key parameters to boost the photothermal and photocatalytic performance.

7.2.2 Development of efficient photocatalysts

As concluded in Chapter 6, the bimetallic Ag and Au NPs were found to show a remarkable photocatalytic response at an optimized Ag:Au ratio. It is suggested that the presence of other noble metals such as Pt, Pd and Cu could be favourable in the design of efficient photocatalysts for the selective oxidation of benzyl alcohol to benzaldehyde. Finally, as it has been shown in Chapter 5 the support plays a significant role in the photocatalytic performance. In this direction, further investigation on the effect of

different supports is proposed to promote higher reaction rates along with the suppression of by-products generation.

7.2.3 Effect of different solvents and activity of synthesized photocatalysts for the selective oxidation of several aromatic alcohols

As established in Chapters 5 and 6, toluene as solvent promotes the selective oxidation of benzyl alcohol to benzaldehyde in the presence of mono- and bi-metallic nanoparticles decorated on the surface of Cr_2O_3 microspheres. Further work requires verifying the versatility of $Ag/Au/Cr_2O_3$ microspheres in the production of benzaldehyde using different solvents (e.g. chloroform, acetonitrile) under the same experimental set-up. Particularly, green solvents such as water and dimethylcarbonate (DMC) should be examined demonstrating the potential to replace environmentally harmful solvents. Additionally, further investigation on the photocatalytic oxidation of various aromatic alcohols in the presence of $Ag/Au/Cr_2O_3$ microspheres is suggested. In this way, the synthesized $Ag/Au/Cr_2O_3$ microspheres will be validated as efficient photocatalysts for the selective oxidation of alcohols to corresponding aldehydes e.g by substitution of para-substituted benzylic alcohols with –Cl or electron releasing group such as –OCH_3 and –CH_3.

7.2.4 Investigation of benzyl alcohol oxidation mechanism

In Chapters 5 and 6, mechanistic studies were performed using different radical scavengers to detect the main oxidative species for the photocatalytic oxidation of benzyl alcohol into benzaldehyde in the presence of mono- and bi-metallic NPs. Validation of the proposed mechanism requires the development of advanced in situ/operando characterization techniques such as gas chromatography – mass spectroscopy and Raman spectroscopy to observe at real time the intermediate species as well as changes of the material crystal or morphological structure. Finally, theoretical calculations such as density functional theory (DFT) and Fine Difference Time Domain (FDTD) can elucidate molecular level mechanistic information in terms of reactant/surface dynamics and the nature of the transition-state.

APPENDIX A
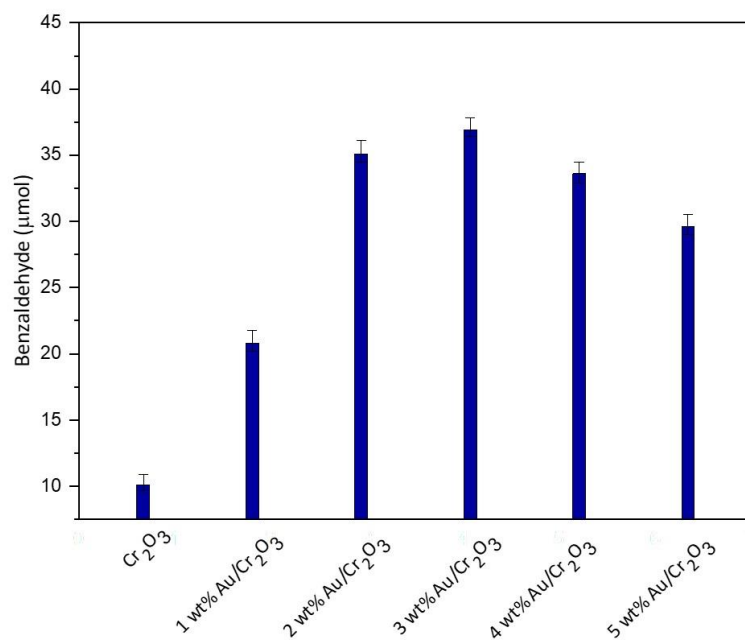
Figure A.1. Benzaldehyde production for pure Cr_2O_3 and Au-Cr_2O_3 photocatalysts.
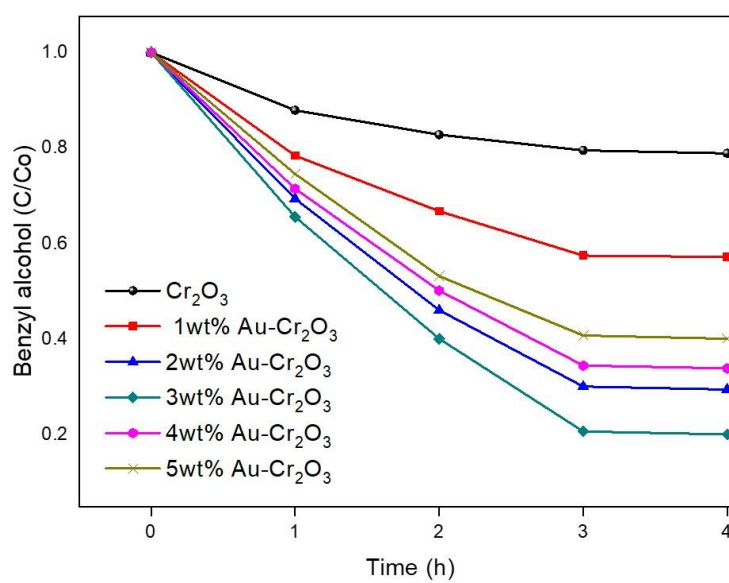
Figure A.2. Conversion rate of the as-synthesized photocatalysts

141
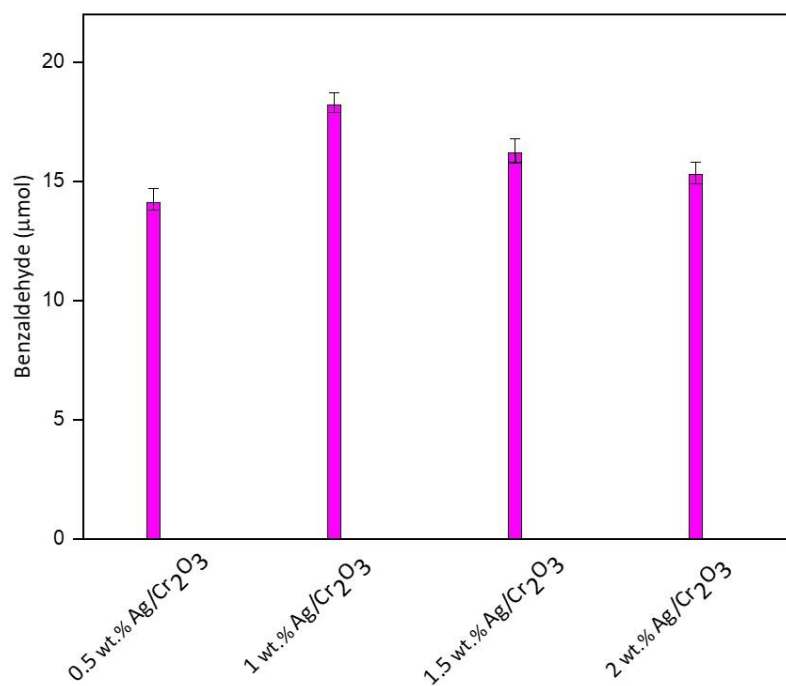
Figure A.3. Benzaldehyde production for Ag loaded on Cr_2O_3 microspheres.
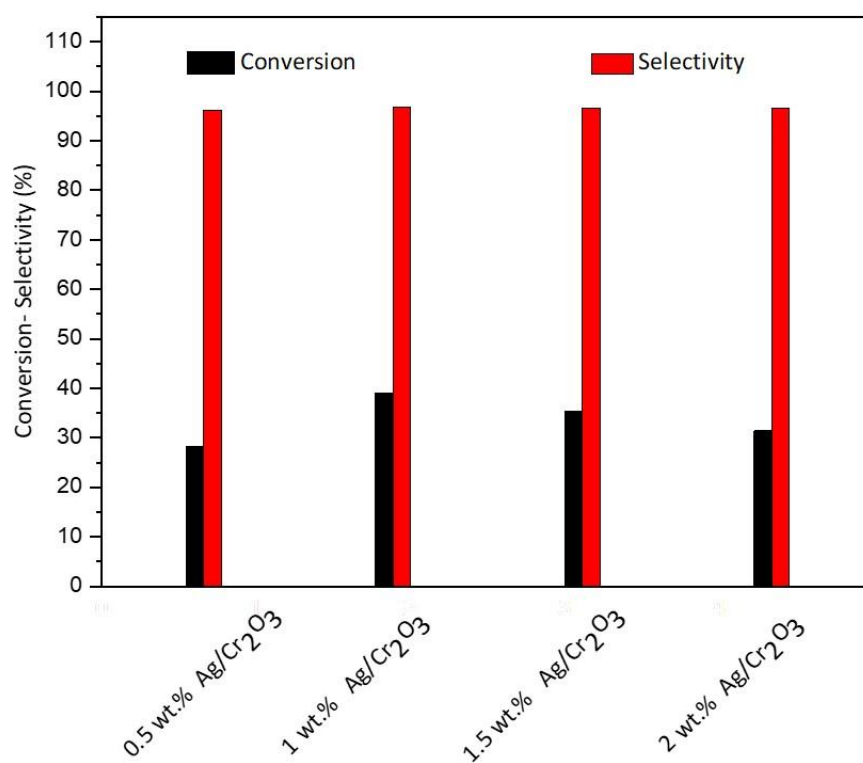
Figure A.4. Benzyl alcohol conversion and benzaldehyde selectivity for Ag loaded on Cr_2O_3 microspheres.

APPENDIX B

LIST OF FIGURES

Chapter 2

Chapter 3

Chapter 4

Chapter 5

Chapter 6

147

LIST OF TABLES